

FIRST-PRINCIPLES SIMULATIONS IN MULTIPLE DIMENSIONS: NANO-PARTICLES, SURFACE AND BULK

By

YUNING WU

A DISSERTATION PRESENTED TO THE GRADUATE SCHOOL
OF THE UNIVERSITY OF FLORIDA IN PARTIAL FULFILLMENT
OF THE REQUIREMENTS FOR THE DEGREE OF
DOCTOR OF PHILOSOPHY

UNIVERSITY OF FLORIDA

2012

© 2012 Yuning Wu

To my wife and my parents

ACKNOWLEDGMENTS

First I would like to thank my advisor, Professor Hai-Ping Cheng, who has taught me so much. I benefit enormously from her professional guidance and rigorous scientific attitude. She has always been watchful and helpful for me, not only as my advisor, but also as a friend. I will take her diligence, strictness and enthusiasm in science as my role model for the rest of my life.

I am very grateful to all my collaborators, including Dr. Xiao-Guang Zhang, Professor Amlan Biswas, Dr. Schmidt Martin, Dr. Nouari Kebaïli, and Dr. Catherine Bréchignac, for their valuable discussions and suggestions. It is great pleasure to collaborate with them.

I would also like to thank my committee members, including Professors Henk Monkhorst, Peter Hirschfeld, Amlan Biswas, and Youping Chen, as well as Professor Samuel Trickey. Their efforts to improve the quality of this thesis are highly appreciated.

I also want to thank previous and current group members, especially Dr. Chao Cao. Discussion with him has always been very beneficial, valuable and pleasant. I have learned a lot also from Dr. Yan Wang.

In addition, my gratitude also goes to my friends in Gainesville for their delightful companionship. They are Xue and family, Yue and family, Bo and family, Yan and family, Xingyuan and family, Yilin and family, Mengxing and family, and Jin.

Finally, I want to thank my parents and my wife, for their endless love and support.

I thank the US/DOE grant DE-FG02-02ER45995, NSF/PHY-0855292 and NSF/DMR-0804407, as well as the UF/HPC and DOE/NERSC for computing resources.

TABLE OF CONTENTS

	<u>page</u>
ACKNOWLEDGMENTS.....	4
LIST OF TABLES	8
LIST OF FIGURES.....	10
LIST OF ABBREVIATIONS.....	13
ABSTRACT	14
CHAPTER	
1 BACKGROUND	16
2 THEORETICAL AND COMPUTATIONAL METHODS.....	20
2.1 Density Functional Theory	20
2.1.1 Fundamental	20
2.1.2 Kohn-Sham Procedure	21
2.2 Exchange-Correlation Functionals	24
2.2.1 Local Density Approximation (LDA).....	24
2.2.2 Generalized Gradient Approximation (GGA).....	25
2.2.3 Hybrid Functionals.....	26
2.3 Plane Wave Basis Set	27
2.4 Pseudopotential	28
2.4.1 Norm-Conserving Pseudopotential.....	28
2.4.2 Ultrasoft Pseudopotential and Projector-Augmented Wave (PAW) Method	30
2.5 Modern Theory of Polarization.....	34
2.5.1 Conventional Definition.....	34
2.5.2 Fundamental of Polarization Theory.....	35
2.5.3 Berry Phase Description.....	36
2.5.4 The Quantum of Polarization.....	38
2.5.5 The Connection to Wannier Orbitals	39
3 CO-ADSORPTION OF N ₂ AND O ₂ ON SILVER CLUSTERS	40
3.1 Methods and Computational Details	42
3.2 Results and Discussion.....	43
3.2.1 Structure of Pristine Ag _n Clusters	43
3.2.2 Physisorption of N ₂ Molecules	46
3.2.3 Chemisorption of O ₂ Molecules	50
3.2.4 (N ₂) _n -O ₂ Co-adsorption on Ag ₄ ⁺	52

3.3 Summary and Conclusion	53
4 ENHANCE OF AG CLUSTER MOBILITY ON AG SURFACE BY CHLORIDIZATION	57
4.1 Methods and Computational Details	59
4.2 Results and Discussion.....	60
4.2.1 Ag_nCl_m Clusters on Ag(111) Surfaces	60
4.2.1.1 Ag Monomer and AgCl	61
4.2.1.2 Ag dimer and Ag_2Cl	62
4.2.1.3 Ag Trimer and Ag_3Cl_3	65
4.2.1.4 Ag Tetramer and Ag_4Cl_4	67
4.2.1.5 Formation Energies.....	69
4.2.2 $(\text{Ag}_{55})_2$ dumbbell structure	70
4.3 Summary and Concluion.....	72
5 MOLECULAR MAGNETOCAPACITANCE	74
5.1 Method and Computational Details	75
5.2 Results and Discussion.....	76
5.3 Summary and Conclusion	85
6 FIRST-PRINCIPLES STUDIES OF C_{60} MONOLAYERS ON METAL SURFACES	87
6.1 Fe-doped monolayer C_{60} on <i>h</i> -BN/Ni(111) Surface	87
6.1.1 Method and Computational Details	89
6.1.2 Results and Discussions	92
6.1.2.1 Structure	92
6.1.2.2 Electronic and Magnetic Properties	99
6.1.3 Summary and Conclusions.....	111
6.2 C_{60} on defected Au(111) surface	113
6.2.1 Method and Computational Details	114
6.2.2 Results and Discussions	114
7 SYMMETRY BREAKING INDUCED BY EPITAXIAL STRAIN IN BiMnO_3 THIN FILM.....	118
7.1 Method and Computational Details	119
7.2 Results and Discussions.....	119
7.3 Summary and Conclusions	125
8 FIRST-PRINCIPLES STUDIES OF Ta_2O_5 POLYMORPHS	126
8.1 Method and Computational Details	128
8.2 Results and Discussions.....	132
8.2.1 Structures	132
8.2.1.1 δ and β L- Ta_2O_5	132

8.2.1.3 77-atom L-Ta ₂ O ₅	137
8.2.1.4 Model amorphous Ta ₂ O ₅	138
8.2.2 Energetics and electronic structure	139
8.2.3 Elastic Moduli	141
8.2.4 Technical remarks: VCA and direct approach	142
8.3 Summary and Conclusion.....	147
9 CONCLUSIONS	148
LIST OF REFERENCES	152
BIOGRAPHICAL SKETCH.....	166

LIST OF TABLES

<u>Table</u>	<u>page</u>
3-1 Total energy (TE), binding energy per atom (BE/n), and ionization potential (IP) obtained by using HSE (2 nd and 3 rd columns) and PBE (4 th and 5 th columns), respectively.....	45
3-2 Total energy (TE) and adsorption energy per N ₂ molecule (AE/m) obtained by using HSE (2 nd and 3 rd columns) and PBE (4 th and 5 th columns), respectively.....	47
3-3 Adsorption energy and charge transfer to O ₂ molecules adsorbed on Ag _n ⁺ cations. The lowest energy states are written in italic.....	52
4-1 The energies E and formation energies E _f (in meV) of Ag _n and Ag _n Cl _m clusters on an Ag(111) surface. The ground state energy of each cluster is set to zero.....	69
4-2 Diffusion barriers E _d of Ag _n and Ag _n Cl _m clusters on an Ag(111) surface. All energies are in meV.	70
4-3 Distance to the center of cluster (in Å) of each layer (labeled by L-Cl/O, L-1, L-2, and L-3) and change in charge (in e ⁻) in each layer. + means gaining electrons and – losing electrons.	71
4-4 Binding energy (in eV) between two Ag ₅₅ -based clusters.....	71
5-1 Energies of neutral, cation, and anion of both HS and LS states. Adding/removing one spin up/down electron are all considered. The energy of neutral LS state (ground state) is set to be 0.....	78
5-2 Ionic potential (IP), electron affinity (EA), capacitance (C), and charging energy (E _c) of both HS and LS states.....	79
5-3 Energies of neutral, cation and anion of both AFM and FM states. Adding/removing one spin up/down electron are all considered. The energy of neutral AFM state (ground state) is set to be 0.....	84
5-4 The ionization potential, electron affinity, charging energy, and capacitance of the Fe-C ₆₀ -Fe system for both AFM and FM states.....	85
5-5 Energies, magnetizations and estimated switch fields (from AFM to FM) of Fe _n -C ₆₀ -Fe _n systems.....	85
6-1 Binding energy of Fe atoms at various sites in eV.....	94
6-2 Charge transfer and magnetic moments as computed by the Bader method... ..	103

6-3	Spin populations on the individual orbitals of Fe and C ₆₀ , ↑ spin up, ↓ spin down, <i>m</i> magnetic moment.....	111
6-4	Structure and energies: <i>dz</i> is the average inter-planar distance, Δ the average intra-layer buckling amplitude, and Δ_{xy} the average lateral displacement of atoms surrounding a vacancy (see Figure 6-11)	117
8-1	The optimized lattice constants, <i>a</i> , <i>b</i> , <i>c</i> . Numbers in parenthesis are calculated with symmetry constraints. All lengths are in unit of Å.....	135
8-2	Comparison of bond lengths and angles of symmetric and optimized δ-phase structure. All lengths are in unit of Å and angles in degree.....	136
8-3	Comparison of bond lengths and angles of symmetric and optimized β-phase structure. All lengths are in unit of Å and angles in degree.....	137
8-4	Numbers of oxygen and tantalum atoms, and cohesive energy. Values in parentheses are calculated with symmetry constraints. All lengths are in unit of Å.....	141
8-5	Elastic constants, Bulk moduli, Shear moduli, Young's moduli, and Poisson's ratio of different phases of Ta ₂ O ₅ . Y _x , Y _y and Y _z are Young's modulus along <i>a</i> , <i>b</i> and <i>c</i> axis.	144
8-6	Bulk moduli, Young's moduli, and Poisson's ratio of different phases of Ta ₂ O ₅ . Y are Young's modulus along <i>c</i> axis, calculated via direct method for validating VCA.....	146

LIST OF FIGURES

<u>Figure</u>	<u>page</u>
3-1 (a) Intensity histograms of $\text{Ag}_4^+(\text{N}_2)_m$ and (b) The mean number of N_2 adsorbed on Ag_4^+ and on Ag_4^+O_2 as a function of nitrogen pressure. (c) The mean number of oxygen molecules on all $\text{Ag}_4^+(\text{N}_2)_m$ clusters.....	41
3-2 Structure of Ag_n ($n=5-7$) neutral clusters and cations. The structures (a) in the left column are the most stable ions. (a-d) indicates decreasing stability of the ions.....	46
3-3 N_2 -adsorption on Ag_n^+ ($n=3, 4, 6, 7$). Both PBE and HSE06 XC were used. Results are listed in Table 3-2.	48
3-4 O_2 -adsorption on Ag_n^+ ($n=1-6$) cations. The adsorption energies and the Bader charge transfer are listed in Table 3-3.	51
3-5 The lowest energy states of $\text{Ag}_4\text{O}_2^+-(\text{N}_2)_m$ and of $\text{Ag}_4^+-(\text{N}_2)_m$ with $m=2-5$, respectively.....	54
4-1 Ag adatoms and AgCl clusters or separately adsorbed adatoms on an $\text{Ag}(111)$ surface.....	62
4-2 Ag dimer and Ag_2Cl clusters adsorbed on $\text{Ag}(111)$ surface.....	64
4-3 Ag trimers and Ag_3Cl_3 clusters adsorbed on an $\text{Ag}(111)$ surface.	66
4-4 Ag tetramers and Ag_4Cl_4 clusters adsorbed on an $\text{Ag}(111)$ surface.	68
4-5 (a) $\text{Ag}_{55}\text{-Ag}_{55}$ dumbbell structure. (b) Optimized $\text{Ag}_{55}\text{Cl}_{19}$ structure. (c) Optimized $(\text{Ag}_{55}\text{Cl}_{19})_2$ dumbbell structure. (d) Optimized $(\text{Ag}_{55}\text{O}_{19})_2$ dumbbell structure.	73
5-1 Optimized structure of $[\text{Mn}_3]$ molecule. Panel (a) is top view and panel (b) is side view.....	77
5-2 Isosurfaces of charge difference (a) between neutral molecule and cation of HS, (b) between anion and neutral molecule of HS, (c) between neutral molecule and cation of LS, (d) between anion and neutral molecule of LS.	81
5-3 Isosurfaces of charge density of (a) high-spin neutral state HOMO, (b) high-spin anion state HOMO, (c) low-spin neutral state HOMO and (d) low-spin anion state HOMO.....	82
5-4 C_{60} with 2 Fe atoms attached. C atoms are in yellow and Fe atoms are in red.	84

6-1	Fe ₁ -doped C ₆₀ monolayer configurations on an <i>h</i> -BN/Ni (111) surface. Panel (a)-(d): Structure of the configurations according to binding energy. (a) is the most stable and (d) the least. Left column is side view and right is top view.....	93
6-2	Same as Figure 6-1 for Fe ₂ -doped C ₆₀ monolayer on an <i>h</i> -BN/Ni (111) surface.....	95
6-3	Fe ₃ -doped C ₆₀ monolayer on an <i>h</i> -BN/Ni (111) surface. Similar to Figure 6-1 with (a) being the most stable on and (c) the least.	97
6-4	Same as Figure 6-3 for Fe ₄ -doped C ₆₀ monolayer on an <i>h</i> -BN/Ni (111) surface.....	98
6-5	Two isomers of a Fe ₁₅ -doped C ₆₀ monolayer on an <i>h</i> -BN/Ni (111) surface. Panel (a) is more stable than panel (b).....	100
6-6	Projected densities of states (PDOS) and projected densities of spin states (PDOSS) on monolayer C ₆₀ and a Fe atom for FeC ₆₀ / <i>h</i> -BN/Ni(111). Panel (c) and (d) are iso-surfaces of charge density difference and spin density.....	102
6-7	Projected densities of states (PDOS) and projected densities of spin states (PDOSS) on monolayer C ₆₀ and two Fe atoms for Fe ₂ C ₆₀ / <i>h</i> -BN/Ni(111). Panel (e)-(f) present the same information as panel (a)-(d) for the AFM state.	105
6-8	Projected densities of states (PDOS) and projected densities of spin states (PDOSS) on monolayer C ₆₀ and three Fe atoms for Fe ₃ C ₆₀ / <i>h</i> -BN/Ni(111).....	108
6-9	Projected densities of states (PDOS) and projected densities of spin states (PDOSS) on monolayer C ₆₀ and four Fe atoms for Fe ₄ C ₆₀ / <i>h</i> -BN/Ni(111).....	110
6-10	Projected densities of states (PDOS) and projected densities of spin states (PDOSS) on monolayer C ₆₀ and fifteen Fe atoms for Fe ₁₅ C ₆₀ / <i>h</i> -BN/Ni(111)....	112
6-11	C ₆₀ molecules on vacancy sites of Au(111) surface. Panel (a) is side view of C ₆₀ on a 7-atom pit. Panel (b), (c) and (d) are top view of C ₆₀ on 1-, 3- and 7-atom pits, respectively.....	116
7-1	(a) Monoclinic 40-atom unit cell of BMO. (b) 20-atom primitive cell of BMO. Bi atoms are in grey. Mn atoms are large blue (dark) spheres. O atoms are small red (dark) spheres.....	120
7-2	The energies per primitive cell for FM, AFM_2, and Ferri_2 magnetic configurations. (a) is the LDA+U result and (b) is from the HSE06 hybrid functional. Only the most stable AFM and Ferri orders are shown.	122
7-3	(a) The atomic displacements of a primitive cell under 2.2% strain. (b) Isosurface of spin-density of the states within 2 eV below Fermi surface. (c) The calculated polarization corresponding to the strain.....	124

8-1	Panel (a): Structure of δ -phase Ta_2O_5 . Panel (b): Structure of β -phase Ta_2O_5 . Panel (c): Structure of tetragonal phase Ta_2O_5 . Panel (d): Structure of low temperature phase 77-atom Ta_2O_5	134
8-2	Panel (a): Structure of amorphous Ta_2O_5 . Panel (b): pair correlation function of Ta-Ta in a $2 \times 2 \times 2$ super cell. Panel (c): Pair correlation function of Ta-O in a $2 \times 2 \times 2$ super cell.	139
8-3	Panel (a): DOS of δ - Ta_2O_5 . Panel (b): DOS of β - Ta_2O_5 . Panel (c): DOS of tetragonal H- Ta_2O_5 . Panel (d): DOS of tetragonal H- Ta_2O_5 with VCA. Panel (e): DOS of low temperature 77 atoms.	143

LIST OF ABBREVIATIONS

B3LYP	Hybrid functional of Becke three-parameter exchange, and Lee-Yang-Parr correlation
DFT	Density functional Theory
DOS	Density of states
GGA	Generalized gradient approximation
HOMO	Highest occupied molecular orbital
HSE	Hybrid functional of Heyd, Scuseria and Ernzerhof
LDA	Local density approximation
LUMO	Lowest unoccupied molecular orbital
NEB	Nudged elastic band
PBE	Generalized gradient approximation of Perdew, Burke and Ernzerhof
PDOS	Projected density of states
PW91	Generalized gradient approximation of Perdew and Wang
SD	Single-determinant
SMM	Single molecule magnets
VCA	Virtual crystal approximation

Abstract of Dissertation Presented to the Graduate School
of the University of Florida in Partial Fulfillment of the
Requirements for the Degree of Doctor of Philosophy

FIRST-PRINCIPLES SIMULATIONS IN MULTIPLE DIMENSIONS: NANO-PARTICLES,
SURFACE AND BULK

By

Yuning Wu

August 2012

Chair: Hai-Ping Cheng
Cochair: Amlan Biswas
Major: Physics

Systems in different dimensions can exhibit different and nearly unique properties, such as catalytic behavior in zero-dimensional (0D) metal clusters, adsorption patterns of molecules on two-dimensional (2D) noble metal surfaces, and mechanical and magnetic properties in three-dimensional (3D) crystals. Accurate description of quantum effects and electron correlations is imperative to correctly study these systems. Density functional theory (DFT) is a reliable and efficient method to determine the electronic structure across many methods and systems.

We have studied the silver cluster cations and the adsorption of N_2 and O_2 molecules onto them. We have interpreted the mutually cooperative co-adsorption of oxygen and nitrogen as a result of the N_2 -induced increase in charge transfer from Ag_n^+ cations to O_2 .

To understand the role of chlorine in the fragmentation of Ag nanostructures, we have studied the diffusion of Ag_n and Ag_nCl_m ($n = 1$ to 4) clusters on an Ag(111) surface, and the interaction strength of $(Ag_{55})_2$ dimers with and without chloridization. Bond

weakening and enhanced mobility are two important mechanisms underlying corrosion and fragmentation processes.

We have demonstrated the concept of molecular magnetocapacitance, in which the quantum part of the capacitance becomes spin-dependent. The nano-magnet $[\text{Mn}_3\text{O}(\text{sao})_3(\text{O}_2\text{CMe})(\text{H}_2\text{O})(\text{py})_3]$ shows a 6% difference in capacitance.

For 2D systems, we have investigated the structure, energetics, electronic and magnetic structures of Fe_n -doped C_{60} monolayers supported by *h*-BN monolayer covered Ni(111) surfaces. The binding energy, charge transfer (from Fe_n to C_{60}), and magnetic moment all increase monotonically as functions of n . The electron charge transfer is from the spin minority population.

We have also studied the adsorption of C_{60} molecules on Au(111) surface defects. The adsorption energy of the strong bonding configuration is much higher than the weak bonding configuration.

We have investigated the effect of epitaxial strain on a BiMnO_3 thin. Anti-ferromagnetism starts to emerge under about 2% epitaxial strain. The AFM order can break inversion symmetry and induce electric polarization, a result which is comparable to experiment.

Finally, we have studied the structure, energetics, elastic tensors and mechanical properties of four crystalline forms of Ta_2O_5 with exact stoichiometry as well as a model amorphous structure.

CHAPTER 1 BACKGROUND

Improvement of experimental technology, especially the nano-scale technology developed in the last three decades, has broadened the scope of physics and material science enormously from traditional 3D and 2D systems to so-called 0D and 1D systems. A typical example is the existence of carbon in 0D to 3D forms. 0D is C₆₀, 1D is carbon nano-tube, 2D is graphene and 3D is graphite. All are all highlights of scientific research in recent decades. A variety of interesting properties are observed, depending on the dimension and size of the system. For example, zero-dimensional nano-clusters can present catalytic behavior.¹⁻⁹ In recent years, huge amounts of research have been focused on the 2D graphene, due to its rare zero-gap band structure (Dirac cone).¹⁰⁻¹⁴ Furthermore, some specific types of 1D nano-wires, including carbon nanotubes¹⁵⁻²⁰ and nano-ribbons,²¹⁻²⁵ can present semi-conductor properties. Utilizing such properties for new functional materials and devices has become the cutting-edge and challenging task for condensed matter physicists and material scientists.

In principle, most physical properties of interest are determined by the positions of the atomic nuclei and the electron distribution. They appear together in the complete wave function $\Psi(\{R_I\}, \{r_i\})$, where $\{R_I\}$ are the coordinates of atomic nuclei and $\{r_i\}$ are the electron coordinates. The complete wave function is the solution of the Schrödinger equation with the Hamiltonian

$$H = -\frac{1}{2M_I} \sum_I \nabla_I^2 + \frac{1}{2} \sum_{I \neq J} \frac{Z_I Z_J}{|R_I - R_J|} - \frac{1}{2} \sum_i \nabla_i^2 - \sum_{I,i} \frac{Z_I}{|R_I - r_i|} + \frac{1}{2} \sum_{i \neq j} \frac{1}{|r_i - r_j|}. \quad (1-1)$$

Here Hartree atomic units ($\hbar = m_e = e = 1$) are adopted. M_I and Z_I are the mass and charge of the atomic nucleus I . Solving for the wave function can be simplified by

introducing the Born-Oppenheimer approximation, which exploits the much faster velocity of electronic motion than ionic motion (or equivalently, the mass of a nucleus being much larger than the electron mass). The Born-Oppenheimer approximation allows the separation of the complete wave function into nuclear and electron parts:

$$\Psi(\{R_I\}, \{r_i\}) = \psi_e(\{r_i\}) \times \phi_n(\{R_I\}). \quad (1-2)$$

$\psi_e(\{r_i\})$ can be obtained by solving the many-electron Schrödinger equation with the Hamiltonian

$$H_e = -\frac{1}{2} \sum_i \nabla_i^2 - \sum_{I,i} \frac{Z_I}{|R_I - r_i|} + \frac{1}{2} \sum_{i \neq j} \frac{1}{|r_i - r_j|}. \quad (1-3)$$

This separation leaves aside the nuclear kinetic energy (term in Equation 1-1) and nuclear Coulomb repulsions (second term in Equation 1-1). The nuclear motion then can be determined from the Hamiltonian with the nuclear terms (first two terms in Equation 1-1), plus the electronic energy as a function of $\{R_I\}$ derived from the electronic Hamiltonian.

Solving for the electronic wave function is still not an easy task. The third term in Equation 1-3, which introduces many-body electron-electron correlation, makes the problem so difficult that generally it is not solvable analytically. A many-body Schrödinger equation can be solved approximately by two categories of approaches. The first category, quantum chemistry methods,²⁶ is mostly based on the Hartree-Fock theory, which approximates the wave function as a Slater determinant. Hartree-Fock theory captures exact electron exchange, but omits electron correlation. It can be improved by including more determinants in the wave function, such as in configuration interaction (CI) and many-body perturbation theory (MBPT). The coupled cluster (CC)

method is not based conceptually on Slater-determinant, but in practice a single Slater-determinant often is the reference function. The accuracy of CI or CC can be improved arbitrarily in principle, however, the high time consumption limits computational application to systems of tens to hundreds of atoms.

Density functional theory²⁷ (DFT) is the second category. It is based on the Hohenberg-Kohn theorem, which states that the ground state energy is a unique functional of the electron density. The Kohn-Sham self-consistent procedure,²⁸ proposed in 1965, makes the Hohenberg-Kohn theorem a practical tool to solve for the ground state energy of a many-body system. In Kohn-Sham DFT, the interacting many-electron system is treated as a set of non-interacting electrons with an effective potential. Kohn-Sham DFT has achieved great success, because with reasonable approximate functionals, it can obtain good accuracy with relatively low computational effort. With the help of super-computers, pseudopotentials and efficient algorithms, DFT can treat systems as large as 1000 electrons. The major approximation is the exchange-correlation functional. The simplest level is the local density approximation²⁹,³⁰ (LDA). Other exchange-correlation functionals, such as GGA,³¹ LDA+U, GGA+U,^{23, 32-},³⁴ and hybrid functionals,³⁵⁻³⁷ have been devised proposed to improve upon LDA in treating large classes of systems.

To proceed, the remaining chapters are organized as following. Chapter 2 provides a general review of DFT, pseudo potentials, and the modern theory of polarization. In Chapter 3, DFT study of co-adsorption of N₂ and O₂ on silver cluster cations is presented. Chapter 4 discusses enhancement of Ag cluster mobility on Ag(111) surfaces by chloridization. The concept of molecular magnetocapacitance is

elaborated in Chapter 5. Studies of C₆₀ monolayer on defected Au(111) and h-BN-covered Ni(111) surface are presented in Chapter 6. The strain effect of the multiferroic BiMnO₃ thin film is discussed in Chapter 7. Finally the structural, energetic, mechanical properties of Ta₂O₅ polymorphs are shown on Chapter 8, and the work as a whole is summarized in Chapter 9.

CHAPTER 2

THEORETICAL AND COMPUTATIONAL METHODS

2.1 Density Functional Theory

2.1.1 Fundamental

As explained in Chapter 1, the Born-Oppenheimer approximation allows the separation of the electronic many-body Hamiltonian from the total Hamiltonian. The electronic Hamiltonian (Equation 1-3) can be rewritten as

$$H = T + V_{ext} + V_{int}, \quad (2-1)$$

where the kinetic energy T is

$$T = -\frac{1}{2} \sum_i \nabla_i^2, \quad (2-2)$$

the external potential V_{ext} from the nuclei-electron interaction is

$$V_{ext} = -\sum_{I,i} \frac{Z_I}{|R_I - r_i|}, \quad (2-3)$$

and the internal electron-electron Coulomb interaction is

$$V_{int} = \frac{1}{2} \sum_{i \neq j} \frac{1}{|r_i - r_j|}. \quad (2-4)$$

For all N-electron systems, T and V_{int} are the same if they are taken as operators.

Therefore, the ground state wave function $\psi_0(\{r_i\})$ is decided by V_{ext} . The corresponding ground state electron density is given by

$$n_0(r) = \langle \psi_0 | \psi_0 \rangle = \int \prod_{i=2}^N dr_i |\psi_0(r, r_2, r_3, \dots, r_N)|^2. \quad (2-5)$$

The Hohenberg-Kohn theorem²⁷ states that, for an N-electron system,

- (1) The external potential V_{ext} is completely and uniquely determined by the corresponding ground state electron density $n(r)$, up to an additive constant.

- (2) For all V-representable densities $n(r)$, the energy corresponding to $n(r)$ is no less than the ground state energy. The ground state energy can be obtained by the variational minimization of a functional of $n(r)$. Here a density is V-representable if it derives from an eigenstate of a Hamiltonian with a certain external potential V_{ext} .

Thus, the ground state expectation value of the Hamiltonian can be reformed as a functional of $n(r)$,

$$E[n] = T[n] + V_{ext}[n] + V_{int}[n]. \quad (2-6)$$

The required V-representability can be weakened to N-representability according to Levy and Lieb's constrained search formulation.^{38, 39} The N-representability, which is much weaker than V-representability, only requires that the total integral of the density is N, and the proper differentiability of \sqrt{n} . In their formulation, the variational minimization is done in two steps, first of which is searching among the wave functions yielding a specific density n , and the second step is varying the n . It can be presented as

$$E_0 = \min_n \left\{ \min_{\psi \rightarrow n} [\langle \psi | T + V_{int} | \psi \rangle] + \int V_{ext}(r) n(r) dr \right\} \quad (2-7)$$

2.1.2 Kohn-Sham Procedure

Although the ground state energy is well proven to be a functional of the charge density, the Hohenberg-Kohn theorem is not practical for real systems because the functional cannot be defined, or specifically, the kinetic energy and the non-classical part of the inter-electronic interactions cannot be written as a functional of the charge density. To take advantage of the theorem, a self-consistent procedure is proposed by Kohn and Sham.²⁸ It maps the many-body interacting electrons to fictitious non-

interacting electrons. The ground state charge density is assumed to be reproducible by the non-interacting electrons.

In Equation 2-6, V_{int} can be separated into two parts, a classical part and a non-classical part. The classical part is

$$V_h[n] = \frac{1}{2} \int \frac{n(r)n(r')}{|r-r'|}, \quad (2-8)$$

which is also called the Hartree energy. The non-classical part (denoted as V_{xc}), which is called the exchange-correlation energy, cannot in general be explicitly written as a density functional. Thus Equation 2-6 can be rearranged into

$$E[n] = T[n] + V_{ext}[n] + V_h[n] + V_{xc}[n]. \quad (2-9)$$

The essence of the Kohn-Sham procedure is the introduction of the kinetic energy of the assumed non-interacting electrons ($T_0[n]$), and the difference between $T_0[n]$ and $T[n]$ is combined with the unknown V_{xc} to form $V'_{xc}[n]$.

Then we can rewrite Equation 2-9 into

$$E[n] = T_0[n] + V_{ext}[n] + V_h[n] + V'_{xc}[n]. \quad (2-10)$$

We can thus perform the variational minimization of this functional, with a Lagrange multiplier μ to constrain the number of electrons to be N:

$$\delta(T_0[n] + V_{ext}[n] + V_h[n] + V'_{xc}[n] - \mu \left(\int n(r) dr - N \right)) = 0. \quad (2-11)$$

Then we have

$$\frac{\delta T_0[n]}{\delta n(r)} + \frac{\delta(V_{ext}[n] + V_h[n] + V'_{xc}[n])}{\delta n(r)} = \mu. \quad (2-12)$$

We define

$$v_h(r) = \frac{\delta V_h[n]}{\delta n(r)} = \int \frac{n(r')}{|r - r'|} dr', \quad (2-13)$$

and

$$v_{xc} = \frac{\delta V'_{xc}[n]}{\delta n(r)}. \quad (2-14)$$

We can thus define a total one-body potential

$$v_{eff}(r) = v_{ext}(r) + v_h(r) + v_{xc}(r). \quad (2-15)$$

Note that Equation 2-12 is exactly the same equation as for a system of non-interacting electrons in an external potential $v_{eff}(r)$. Therefore, the wave functions of the non-interacting electrons can be obtained by

$$\left[-\frac{1}{2} \nabla^2 + v_{eff}(r) \right] \psi_i(r) = \epsilon_i \psi_i(r). \quad (2-16)$$

The total kinetic energy of non-interacting electrons is calculated from

$$T_0[n] = -\frac{1}{2} \sum_{i=1}^N \int \psi_i(r)^* \nabla^2 \psi_i(r), \quad (2-17)$$

and the charge density is constructed as

$$n(r) = \sum_{i=1}^N |\psi_i(r)|^2. \quad (2-18)$$

Equations 2-13 to 2-18 form a self-consistent loop, which defines a practical way to minimize the functional (Equation 2-10). A guess of the charge density can form a set of non-interacting orbitals, constructing a new charge density for the next iteration. The

functional is minimized once the input and the output charge density are the same up to a desired level of accuracy.

2.2 Exchange-Correlation Functionals

Although the Kohn-Sham recipe of DFT is exact in principle, the XC functional is nearly impossible to derive explicitly. The difficulty comes from the fact that the XC potential at position r depends on the value of the XC energy ($v_{xc}[n]$ in our notation) not only at this point, but also its variation nearby. We can expand the XC energy in terms of the gradients of the charge density,

$$v_{xc}[n(r)] = v_{xc}[n(r), \nabla n(r), \nabla(\nabla n(r)), \dots]. \quad (2-19)$$

Normally, only the local density $n(r)$ and its gradient $\nabla n(r)$ (if necessary) are considered in the expansion, because higher order gradients in the expansion are known to misbehave. Commonly used XC functionals include local density approximation^{29, 30} (LDA), generalized gradient approximation (GGA) and hybrid functionals. We summarize these next.

2.2.1 Local Density Approximation (LDA)

The simplest way to construct the XC functional is to evaluate the XC energy density locally at every point, i.e., the XC energy density at point r is assumed to be the same as the XC potential at this point in a homogeneous electron gas with density $n(r)$. Thus the total XC energy ($V'_{xc}[n]$ in our previous notation) is

$$E_{xc}^{LDA}[n(r)] = \int n(r) \epsilon_{xc}^{\text{hom}}(n(r)) dr, \quad (2-20)$$

where $\epsilon_{xc}(n)$ is the XC energy per electron in a homogeneous electron gas of density n , which is already calculated to great accuracy. Due to the assumption that electrons at

a point feel the XC potential of a homogeneous electrons gas, one would expect LDA to be good for systems close to the homogeneous electron gas, and poor in very inhomogeneous systems.

Although unphysical in its strict locality, LDA works surprisingly successfully. Several parameterizations of LDA have been proposed and they all work quite well. The LDA helps to give useful predictions on electron densities, atomic positions, *etc*, but it can fail in predicting band gaps.

2.2.2 Generalized Gradient Approximation (GGA)

The LDA can be improved by introducing the dependence of spatial variation of the charge density into the XC energy. Many forms of GGA have been proposed to do this. They generally are of the form⁴⁰

$$E_{xc}^{GGA}[n(r)] = \int n(r) \epsilon_{xc}(n(r)) dr = \int n(r) \epsilon_x^{\text{hom}}(n(r)) F_{xc}(n(r), |\nabla n(r)|) dr, \quad (2-21)$$

where ϵ_x^{hom} is the exchange energy of homogeneous electron gas and F_{xc} is a dimensionless function. In more careful notation, F_{xc} is separated into two parts, the exchange part F_x and the correlation part F_c . Both of them can be expressed as a function of n and s , where n is the charge density and

$$s = \frac{|\nabla n|}{2(3\pi^2)^{\frac{1}{3}} n^{\frac{4}{3}}}. \quad (2-22)$$

The correlation part typically contributes much less than the exchange.

Different GGA recipes, using different forms for F_{xc} , have been proposed. The most commonly used GGA functionals include PW91,⁴¹ B88,⁴² PBE,³¹ etc. GGA

functions cover the non-local effect to some degree, and hence they show better performance in systems with high density gradient than LDA.

2.2.3 Hybrid Functionals

Hybrid functionals are a group of XC functionals which combine the exact exchange from orbital-dependent single-determinant (SD) exchange and conventional DFT functionals.⁴³ Hybrid functionals introduce a certain fraction of SD exchange (normally 20% to 25%), which has an error-canceling effect on the self-interaction error from conventional functionals. Hybrid functionals generally work better in energetic calculations, such as molecular properties and structural calculations,⁴⁴ than LDA or GGA. The general form of the hybrid functionals⁴⁵ is

$$E_{xc}^{hybrid} = \mu(E_x^{SD} - E_x^{GGA/LDA}) + E_{xc}^{GGA/LDA}, \quad (2-23)$$

where E_x^{SD} is the exact HF exchange, and the hybrid coefficient μ often is fitted according to atomic and molecular data.

Many hybrid functionals have been proposed, including B3LYP,⁴⁶ PBE0,⁴⁷ HSE,³⁶ etc. B3LYP has the form of

$$E_{xc}^{B3LYP} = E_{xc}^{LDA} + a_0(E_x^{HF} - E_x^{DFA}) + a_x E_x^{Becke} + a_c E_c, \quad (2-24)$$

in which a_0 , a_x and a_c vary according to the elements and molecules.

The PBE0 functional contains 25% of exact exchange, combined with 75% of PBE-GGA exchange. The correlation is totally represented by PBE-GGA. It has the following form:

$$E_{xc}^{PBE0} = \frac{1}{4} E_{xc}^{HF} + \frac{3}{4} E_x^{PBE} + E_c^{PBE}. \quad (2-25)$$

The PBE0 functional yields obvious improvements in certain problems over LDA/GGA, however, its self-consistent SD calculation is very time-consuming. The HSE03/HSE06 hybrid functionals were invented to reducing the computing cost without significant loss of accuracy. The idea is to separate the SD exchange into long-range (LR) and short-range (SR) terms. In HSE03/HSE06, the LR term is replaced by the PBE LR exchange. The resulting expression is thus,

$$E_{xc}^{HSE} = \frac{1}{4} E_x^{SR}(\xi) + \frac{3}{4} E_x^{PBE,SR}(\xi) + E_x^{PBE,LR}(\xi) + E_c^{PBE}. \quad (2-26)$$

In other words, the hybridization of exact exchange and explicit DFT exchange only happens in short range. HSE03/HSE06 give very similar results to PBE0, but greatly reduces the computational effort. The range-separation is determined by the parameter ξ . A value of 0.3 means HSE03, while 0.2 is used in HSE06. ξ is also related to a characteristic distance, $2/\xi$, where the SR term goes negligible.

2.3 Plane Wave Basis Set

There exist several ways of representing the one-body wave functions or orbitals in the Kohn-Sham equations, including plane waves, atomic orbitals, and real-space grids. The plane wave basis set is commonly used, especially for periodic systems, due to its computational efficiency in the fast Fourier transform (FFT) and easy convergence control. In a plane wave basis, a Bloch function can be expanded as

$$\psi_{n,k}(r) = \sum_G c_{n,k+G} \cdot e^{i(k+G)r}, \quad (2-27)$$

where G are reciprocal lattice vectors. The number of plane waves is controlled by the kinetic energy cutoff E_{cut} by

$$\frac{1}{2}|k + G|^2 \leq E_{cut}. \quad (2-28)$$

The kinetic energy is used as the criteria because it contributes the most to the total energy. As the cutoff energy and the number of plane waves increase, the convergence can be obtained systematically for all forms of wave functions. Compared to other basis sets, the number of necessary plane waves to reach convergence is normally large. The FFT somewhat reduces the efficiency of parallelization because it is non-local and hard to be parallelized.

2.4 Pseudopotential

The large number of the plane waves needed for the convergence is mostly due to the high kinetic energy of the core electrons and the associated nuclear-electron cusp in density. The idea of pseudopotentials is to replace the real potential from nuclei and core electrons by a smooth effective core potential or pseudopotential and focus on valence electrons. The rapid oscillations of the valence electron wave function near the nuclei are replaced by the node-free pseudo wave functions, which are forced to coincide with the real wave functions outside the core region.

2.4.1 Norm-Conserving Pseudopotential

The pseudopotential and pseudo wave function are obtained by solution of the all-electron scalar-relativistic radial atomic Schrödinger equation with the KS-DFT potential $V(r)$

$$\left[\frac{1}{2M(r)} \left(-\frac{d^2}{dr^2} - \frac{\alpha}{2M(r)} \frac{dV(r)}{r} r \frac{d}{dr} \frac{1}{r} + \frac{l(l+1)}{r^2} \right) + V(r) - \varepsilon_l \right] u_l(r) = 0, \quad (2-29)$$

in which

$$M(r) = 1 + \frac{\alpha^2}{2}(\varepsilon_l - V(r)), \quad (2-30)$$

and α is the fine structure constant. The pseudo wave function $\tilde{u}_l(r)$ is constructed according to the following conditions:

- (1) The eigenvalue of $\tilde{u}_l(r)$ must match the eigenvalue of the true wave function $u_l(r)$.
- (2) $\tilde{u}_l(r)$ must coincide with $u_l(r)$ beyond a chosen core radius r_{cl} .
- (3) $\tilde{u}_l(r)$ and $u_l(r)$ include the same amount of charge inside the core radius.
- (4) The first and second derivatives at r_{cl} are identical for $\tilde{u}_l(r)$ and $u_l(r)$.

After $\tilde{u}_l(r)$ is chosen, the pseudopotential \tilde{V}_l then can be obtained by inversion of the non-relativistic radial Schrödinger equation,

$$\left[-\frac{1}{2} \frac{d^2}{dr^2} + \frac{l(l+1)}{r^2} + \tilde{V}_l(r) - \tilde{\varepsilon}_l \right] \tilde{u}(r) = 0, \quad (2-31)$$

and thus

$$\tilde{V}_l(r) = \tilde{\varepsilon}_l - \frac{l(l+1)}{r^2} + \frac{1}{2\tilde{u}(r)} \frac{d^2}{dr^2} \tilde{u}(r). \quad (2-32)$$

An accurate and practical pseudopotential requires a non-local form because different angular momentum states (partial waves) have different scattering properties. $\tilde{V}_l(r)$ can be used to build the non-local part of the pseudopotential in the way proposed by Kleinmen and Bylander,⁴⁸

$$\tilde{V}_{KB} = \tilde{V}_{local} + \sum_{l,m} \frac{|\langle \delta\tilde{V}_l | \varphi_{lm} \rangle \langle \varphi_{lm} | \delta\tilde{V}_l |]}{\langle \varphi_{lm} | \delta\tilde{V}_l | \varphi_{lm} \rangle}, \quad (2-33)$$

in which

$$\delta\tilde{V}_l = \tilde{V}_l - \tilde{V}_{local} , \quad (2-34)$$

$$\tilde{\phi}_{lm} = \tilde{u}(r)Y_{lm} , \quad (2-35)$$

and \tilde{V}_{local} is an arbitrary local potential.

Many recipes for generating the norm-conserving pseudopotential have been proposed, depending on different ways of defining pseudo wave functions in the core region. The Troullier and Martin recipe^{49, 50} uses a polynomial up to 12th order of r . A linear combination of spherical Bessel functions was also proposed by Rappe and Rabe.⁵¹

2.4.2 Ultrasoft Pseudopotential and Projector-Augmented Wave (PAW) Method

Despite the success of norm-conserving pseudopotentials for various elements, such as Si and Al, they still need expensive kinetic energy cutoff for the elements with localized valence states. Norm conservation requires that the core radius cannot be chosen too much beyond the maximum of the true wave function, so the pseudo wave function under the norm-conserving condition is not significantly smoother than the true wave function. Vanderbilt⁵² and Blöchl⁵³ proposed the ultrasoft and projector-augmented wave (PAW) pseudopotential respectively, to resolve this problem.

The ultrasoft pseudopotential avoids the norm-conserving condition by introducing a non-local overlap operator,

$$S = 1 + \sum_{i,j} Q_{ij} |\beta_i\rangle\langle\beta_j| , \quad (2-36)$$

where Q_{ij} is the matrix based on true wave functions ϕ and pseudo wave functions $\tilde{\phi}$ inside the core radius r_{cl} ,

$$Q_{ij} = \langle \varphi_i | \varphi_j \rangle_{r_{cl}} - \langle \tilde{\varphi}_i | \tilde{\varphi}_j \rangle_{r_{cl}}, \quad (2-37)$$

and $|\beta_i\rangle$ are projector functions defined as the dual of $|\tilde{\varphi}_i\rangle$. The norm-conserving condition is $Q_{ij} = 0$, which is generalized to

$$\langle \varphi_i | \varphi_j \rangle_{r_{cl}} = \langle \tilde{\varphi}_i | S | \tilde{\varphi}_j \rangle_{r_{cl}}. \quad (2-38)$$

This indicates that φ and $\tilde{\varphi}$ have the same amplitude beyond the core radius. Define the matrix B_{ij} as

$$B_{ij} = \langle \tilde{\varphi}_i | \chi_j \rangle, \quad (2-39)$$

in which

$$|\chi_i\rangle = (\varepsilon_i - T - V_{loc}) |\tilde{\varphi}_i\rangle, \quad (2-40)$$

and V_{loc} is the chosen local part of the pseudopotential, then the non-local part can be determined as,

$$V_{NL} = \sum_{i,j} (B_{ij} + \varepsilon_i Q_{ij}) |\beta_i\rangle \langle \beta_j|. \quad (2-41)$$

In such a way, the pseudo wave function $|\tilde{\varphi}_i\rangle$ is the solution of the modified Schrödinger equation,

$$(H - \varepsilon_i S) |\tilde{\varphi}_i\rangle = (T + V_{loc} + V_{NL} - \varepsilon_i S) |\tilde{\varphi}_i\rangle = 0. \quad (2-42)$$

The elimination of the norm-conserving condition allows smoother pseudo wave functions and thus a lower energy cutoff.

Similar to the ultrasoft pseudopotential, the projector augmented wave method makes use of projectors and auxiliary localized functions. The calculations of physical quantities, such as energy, involve not only smooth functions over all space, but also

localized contributions inside the core regions of ions. The PAW method keeps and uses true wave functions from all-electron KS calculation, which is different from the ultrasoft pseudopotential. The basic idea of the PAW method is shown as following. More details can be found in Blöchl's original literature.⁵³

The all-electron wave function ψ and the smooth auxiliary wave function (or pseudo wave function) $\tilde{\psi}$ are related by a linear transformation

$$|\psi_n\rangle = T |\tilde{\psi}_n\rangle . \quad (2-43)$$

The transformation should modify $\tilde{\psi}$ only inside augmentation spheres for each atom, so the operator T can be written as,

$$T = 1 + \sum_R T_R , \quad (2-44)$$

where R means the atomic sites, and T_R only acts in the augmentation sphere of site R . For each site, the auxiliary atomic wave function $\tilde{\varphi}_i$ can be defined from the all-electron partial waves φ_i by

$$|\varphi_i\rangle = T |\tilde{\varphi}_i\rangle = (1 + T_R) |\tilde{\varphi}_i\rangle \quad \text{for } i \in R . \quad (2-45)$$

Then a set of projector functions $|\tilde{p}_i\rangle$ is constructed inside the augmentation sphere, following

$$\langle \tilde{p}_i | \tilde{\varphi}_j \rangle = \delta_{ij} \quad (2-46)$$

and

$$\sum_i |\tilde{\varphi}_i\rangle \langle \tilde{p}_i| = 1 . \quad (2-47)$$

Inside the augmentation sphere of site R , the auxiliary wave function can be expanded by auxiliary atomic wave functions as

$$|\tilde{\psi}_n\rangle = \sum_{i \in R} \langle \tilde{p}_i | \tilde{\psi}_n \rangle |\tilde{\varphi}_i\rangle. \quad (2-48)$$

Plug in Equation 2-45 and we can get

$$T_R |\tilde{\psi}_n\rangle = \sum_{i \in R} (\langle \varphi_i \rangle - \langle \tilde{\varphi}_i \rangle) \langle \tilde{p}_i | \tilde{\psi}_n \rangle, \quad (2-49)$$

so the transformation T is

$$T = 1 + \sum_R \sum_{i \in R} (\langle \varphi_i \rangle - \langle \tilde{\varphi}_i \rangle) \langle \tilde{p}_i |. \quad (2-50)$$

In other words, the transformation operator is completely defined as a combination of smooth auxiliary partial waves, non-smooth all-electron partial waves, and the projector functions. By applying the operator onto auxiliary wave function, we get

$$|\psi_n\rangle = |\tilde{\psi}_n\rangle + \sum_R \left(\sum_{i \in R} \langle \varphi_i \rangle \langle \tilde{p}_i | \tilde{\psi}_n \rangle - \sum_{i \in R} \langle \tilde{\varphi}_i \rangle \langle \tilde{p}_i | \tilde{\psi}_n \rangle \right). \quad (2-51)$$

The expectation value of any one-body operator \hat{O} is

$$\langle \hat{O} \rangle = \sum_n f_n \langle \tilde{\psi}_n | \hat{O} | \tilde{\psi}_n \rangle + \sum_R \sum_{i,j \in R} (\langle \varphi_i | \hat{O} | \varphi_j \rangle - \langle \tilde{\varphi}_i | \hat{O} | \tilde{\varphi}_j \rangle) D_{ij}^R + \sum_{i=1}^{N^{core}} \langle \varphi^c_i | \hat{O} | \varphi^c_i \rangle, \quad (2-52)$$

where

$$D_{ij}^R = \sum_n f_n \langle \tilde{\psi}_n | \tilde{p}_i \rangle \langle \tilde{p}_j | \tilde{\psi}_n \rangle, \quad (2-53)$$

and φ_i^c is the core wave function.

The PAW method is closely related to, however somewhat better than the ultrasoft pseudopotential. The ultrasoft pseudopotential is the same as the linearization of the on-site compensation energy calculation (inside the augmentation sphere) in PAW scheme. The PAW method is more trustable than the ultrasoft pseudopotential especially in magnetic systems.

2.5 Modern Theory of Polarization

The macroscopic electric polarization, defined as electric dipole per unit volume, is an old but a very important concept regarding dielectric media. Ferroelectric materials, which exhibit spontaneous macroscopic polarization, are of great interest and application, especially if magnetic properties coexist (multiferroics). Despite the importance and significance of this polarization, a mature physical understanding at the first-principles level was not achieved until the 1990s. In this section, the modern theory of polarization is reviewed briefly.

2.5.1 Conventional Definitions

The conventional definition of electric polarization is based on the Clausius-Mossotti model,⁵⁴ in which polarizable units are assumed. The macroscopic electric polarization is thus the accumulation of the dipole moments contributed from the polarizable units, divided by the volume of the whole system. In crystalline systems, the unit cell can be identified as the polarizable unit and the calculation of polarization is within the unit cell,

$$P_{cell} = \frac{1}{V_{cell}} \int_{cell} r \rho(r) dr. \quad (2-54)$$

The key point of the validity of the CM model is that the induced charge can be clearly divided and attributed to the polarizable units. The CM model may work in ionic crystals, in which charge is quite localized due to the ionic bonds. However, in systems with covalent character, the CM model is not valid, because the delocalized charge distribution makes the identification of polarizable units ambiguous.

Other attempts to define polarization through the charge distribution have proven to be failures. Examples include the polarization in a macroscopic volume and the cell

average of the microscopic polarization. Macroscopic polarization can be illustrated by the following equation,

$$P_{sample} = \frac{1}{V_{sample}} \int_{sample} r\rho(r)dr . \quad (2-55)$$

The sample volume is a macroscopic but finite volume, which contains the bulk and surface. This model proves unhelpful because it is very hard to distinguish the surface from the bulk region and because this model has little connection to the bulk property based on periodic boundary conditions. Thus, it is not a useful definition.

The second attempt to model polarization is through a cell average of the microscopic polarization

$$\nabla \cdot P_{micro}(r) = -\rho(r) \quad (2-56)$$

is also not meaningful, because any divergence-free contribution can be added to $P_{micro}(r)$, without violating equation (2-56).

Overall, a more sophisticated definition of polarization is needed, especially for crystalline systems with periodic boundary condition.

2.5.2 Fundamental of Polarization Theory

In practice, it has been realized that the change of polarization ΔP is more physically meaningful than the absolute value of P .⁵⁵ The experimental measurements, either of induced polarization or spontaneous polarization, are based on the change of polarization.⁵⁶ Because of the fundamental equation

$$\frac{dP(t)}{dt} = j(t), \quad (2-57)$$

in which $j(t)$ is the current density, the change of polarization can be written as

$$\Delta P = P(\Delta t) - P(0) = \int_0^{\Delta t} j(t) dt . \quad (2-58)$$

This implies the change of the polarization can be achieved by accumulation through an adiabatic process. Note that $j(t)$ is a bulk property. By introducing an adiabatic time λ ⁵⁵, the last equation can be rewritten to

$$\Delta P = \int_0^1 \frac{dP(\lambda)}{d\lambda} d\lambda , \quad (2-59)$$

where $\lambda = 0$ or 1 refers to the initial or final state, respectively. The initial and final states can be the states before and after the application of electric field, strains, etc. It is convenient, especially when studying the spontaneous polarization, to set the centrosymmetric geometry as the reference point, i.e. $\lambda = 0$, and thus the polarized geometry can be set to $\lambda = 1$.

Both nuclei and electrons contribute to polarization. The ionic contribution is rather straightforward. In terms of the electronic contribution, it is quite interesting to realize that the change of polarization is essentially the accumulation of the adiabatic electronic current, which is closely related to the phase of the wave function in the quantum mechanical picture. The phase of the wave function vanishes during the calculation of the charge density, explaining why the description of polarization by charge density is insufficient for bulk system.

2.5.3 Berry Phase Description^{57, 58}

In a crystalline system with periodic boundary condition, the Bloch theorem tells us that the eigenfunctions have the Bloch wave form $\varphi_{nk}(r) = e^{ik \cdot r} u_{nk}(r)$, where $u_{nk}(r)$ has periodicity of the lattice vectors and follows from $H_k |u_{nk}\rangle = E_{nk} |u_{nk}\rangle$. The Hamiltonian in k space is

$$H_k = \frac{(p + \hbar k)^2}{2m} + V , \quad (2-60)$$

with V , the Fourier transform of the effective one-electron potential.

Considering the adiabatic process depending on the parameter λ , the variation of the wave function can be obtained through a first-order perturbation,

$$|\delta\varphi_{nk}\rangle = -i\hbar \frac{d\lambda}{dt} \sum_{m \neq n} \frac{\langle \varphi_{mk} | \partial_\lambda \varphi_{nk} \rangle}{E_{nk} - E_{mk}} |\varphi_{mk}\rangle , \quad (2-61)$$

where ∂_λ is the derivative with respect to λ . This variation can be utilized to construct the current contributed from the n th band,

$$j_n = \frac{dP_n}{dt} = \frac{i\hbar e}{(2\pi)^3 m_e} \frac{d\lambda}{dt} \sum_{m \neq n} \int dk \frac{\langle \varphi_{nk} | p | \varphi_{mk} \rangle \langle \varphi_{mk} | \partial_\lambda \varphi_{nk} \rangle}{E_{nk} - E_{mk}} + c.c. , \quad (2-62)$$

in which $c.c.$ indicates the complex conjugate. dP/dt . can be converted to $dP/d\lambda$. by multiplying by $dt/d\lambda$. Combined with applying a perturbation to the Hamiltonian in k space, the following form of $dP/d\lambda$. can be obtained,

$$\frac{dP_n}{dt} = \frac{ie}{(2\pi)^3} \int dk \langle \nabla_k u_{nk} | \partial_\lambda u_{nk} \rangle + c.c.. \quad (2-63)$$

Therefore, after an integration with respect to λ and summation over all occupied bands, the electronic polarization is

$$P_{el} = \frac{e}{(2\pi)^3} \text{Im} \sum_n \int dk \langle u_{nk} | \nabla_k | u_{nk} \rangle . \quad (2-64)$$

Here n is the index for all occupied states, including up and down states. With the ionic contribution combined, the total polarization, including ionic and electronic contributions, is formulated as

$$P = P_{ion} + P_{el} = \frac{e}{\Omega} \sum_i Z_i R_i + \frac{e}{(2\pi)^3} \text{Im} \sum_n \int dk \langle u_{nk} | \nabla_k | u_{nk} \rangle , \quad (2-65)$$

where Z_i and R_i are the atomic numbers and coordinates of the ion with index i.

Equation 2-65 is the core statement of the modern theory of polarization. The term $i\langle u_{nk} | \nabla_k | u_{nk} \rangle$ is the gauge potential in Berry-phase theory,^{59, 60} and its integral over a closed manifold (the Brillouin zone in the polarization case) is the Berry phase. The change of polarization is independent of the path the system undergoes during the adiabatic process. To study the ferroelectric material, the starting point is commonly set as the centrosymmetric geometry which gives zero polarization.

2.5.4 The Quantum of Polarization

For simplicity, an 1D case is initially considered. Due to the periodic boundary conditions, the periodic Bloch function $|u_{nk}\rangle$ can be shifted by a phase factor $e^{-i\beta(k)}$, in which $\beta(2\pi/a) - \beta(0) = 2\pi m$ and m is an integer. Thus the polarization contributed from the n th band will have an additional term $m \cdot e$. This implies that the polarization is only well-defined by a series of branches with modulus e . Extended to the 3D case, the polarization is only well-defined by a series of many branches with modulus eR/Ω , where $R = \sum_i m_i R_i$ and R_i are the lattice vectors of the primitive cell. The formula to compute the change of the polarization is generalized to

$$\Delta P := (P_{\lambda=1} - P_{\lambda=0}) \bmod \frac{eR}{\Omega}. \quad (2-66)$$

The “:=” means that the ΔP should be one of the group of values on the right-hand side, i.e. only a branch. All values corresponding to the points along the evolving path should be in the same branch. In practice, several intermediate points normally need to be included in order to stay along the same branch.

2.5.5 The Connection to Wannier Orbitals

The Wannier orbitals provide another view of the Berry-phase polarization. The Wannier orbitals are defined as

$$|w_{nR}\rangle = \frac{\Omega}{(2\pi)^3} \int e^{ik \cdot R} |\varphi_{nk}\rangle dk, \quad (2-67)$$

which is similar to the Fourier transform of Bloch wave. Interestingly, the center of a Wannier orbital $\langle w_{nR} | r | w_{nR} \rangle$ turns out to be

$$r_{nR} = \frac{\Omega}{e} P_n + R. \quad (2-68)$$

The Berry-phase polarization thus can be reconsidered in a Wannier orbital picture. The contribution to the Berry-phase polarization from band n is equivalent to placing an electron sitting at the center of the corresponding Wannier orbital.

CHAPTER 3

CO-ADSORPTION OF N₂ AND O₂ ON SILVER CLUSTERS¹

Metal clusters were a subject of intense research interest in the 1980s because of the fascinating size-dependence of their physical properties.⁶²⁻⁶⁴ In the late 1990s, the unexpected catalytic behavior of charged small noble metal particles^{1-3, 6, 65-67} brought such clusters into the spotlight and continues to stimulate current research interest. Charging of metal clusters is typically achieved by surface charge transfer if the clusters are supported or by ionization and electron attachment in free clusters. To understand the chemical reactivity of small particles, adsorption and reaction of small molecules on clusters are therefore crucial. Several experimental groups have been working on the subject using free clusters in ion beams.⁶⁸⁻⁷⁴ It was noticed that oxygen is molecularly chemisorbed to silver clusters at low temperature but forms silver oxide under heating.⁷²⁻⁷⁴ Furthermore a cooperative effect in the co-adsorption of O₂, and N₂ was found (as shown in Figure 3-1).⁷⁴ In contrast to silver, adsorption of small molecules on gold clusters has been extensively studied theoretically.⁷⁵⁻⁷⁹ However, there is no theoretical work addressing this enhancement in co-adsorption, although the same phenomenon but less pronounced was reported on gold in an experimental paper by Lang *et al.*⁷¹ The stronger chemical activity of Ag over Au makes the silver clusters interesting but also adds complexity to, in particular, consideration of the metal-oxygen interaction.

Structures of pristine metal clusters are critical for theoretical investigations of molecular adsorption. It has been noticed that small gold and silver clusters assume a flat geometry; a 2D-to-3D structure transition occurs within the size range from 5 to

¹ This work has been published in Journal of Chemical Physics.⁶¹

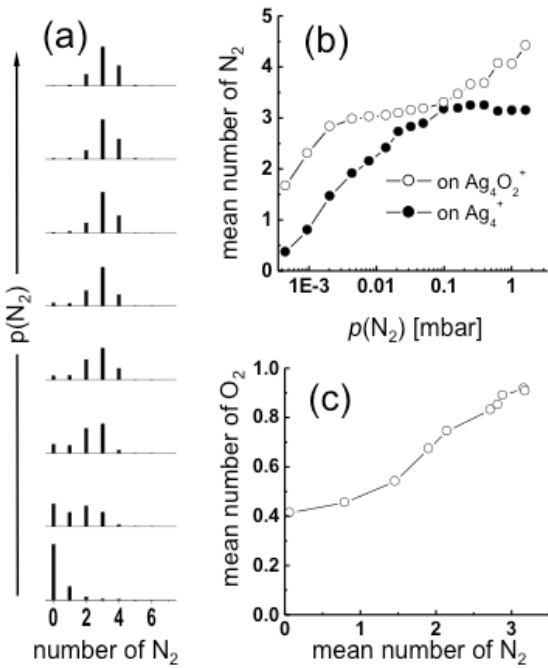


Figure 3-1. (a) Intensity histograms of $\text{Ag}_4^+(\text{N}_2)_m$ over m at different nitrogen pressures. (b) The mean number of N_2 adsorbed on Ag_4^+ and on Ag_4^+O_2 is plotted in comparison as a function of nitrogen pressure p . The presence of chemisorbed O_2 enforces the physisorption of N_2 . (c) The mean number of oxygen molecules on all $\text{Ag}_4^+(\text{N}_2)_m$ clusters depending on the mean number of nitrogen on $\text{Ag}_4^+.12$ atoms, depending on material and charge state.

Anions tend to stay in a 2D geometry at a size slightly larger than the neutral state and the cation, and the gold cluster remains in 2D at a size slightly larger than the silver cluster. For example, a 2D model for Ag_7 is presented by Xiang *et al.* to study the anion state when silver clusters are surrounded by organic ligands.⁸⁰ Nevertheless, in 2002, Kappes' group reported ion mobility measurements of Ag_n^+ cation clusters.⁸¹ It was shown that cation silver clusters transform from the planar structure to 3D at 4-5 atoms. Quantum chemistry calculations performed by the same group at the MP2 level of approximation support this conclusion.⁸¹ Density functional theory (DFT)²⁸ with generalized gradient approximations (GGA), specifically the Perdew-Burke-Ernzerhof (PBE) functional³¹, were used to study oxidization of silver clusters, but a planar

geometry was found to be the ground state of the pristine Ag_6^+ and Ag_7^+ . Fernández and co-workers used the same functional, however they predicted that the 2D to 3D transition occurs from Ag_5^+ to Ag_6^+ .⁸² This discrepancy raises a question regarding the validity of DFT in determining the structure of small noble metal clusters. In a more recent paper by Trublar's group, a number of new functionals have been constructed and applied to study gold anion clusters.⁶⁵ It is evident that the PBE functional fails to handle such subtle structural transformations. Trublar's group also pointed out the significance of electronic structure of single atoms (specifically, the transition energy from $d^{10}s^1$ to d^9s^2).⁶⁵ A revisit of structure of silver clusters is thus desirable. Structures of pristine clusters are important for understanding adsorption and reaction.

This chapter presents calculations of structures of small silver cluster cations using hybrid functionals. This approach predicts to a 2D to 3D transition at 4 to 5 silver atoms. With such a calculation, we go further and study the molecular adsorption of oxygen and nitrogen on different sites of the silver clusters, and coadsorption in order to compare with experimental data. The rest of this chapter is organized as follows: Section 3.1 discusses the theoretical approach, and section 3.2 shows the results on pristine silver clusters, on the N_2 physisorption, on the O_2 -chemisorption and on the O_2 - $(\text{N}_2)_m$ co-adsorption. The chapter ends with summary in section 3.3.

3.1 Methods and Computational Details

All systems have been investigated by density functional theory (DFT)²⁸ with the spin-unrestricted GGA³¹ in the PBE form. We used plane-wave basis in conjunction with the PAW^{53, 83} pseudopotential as implemented in the VASP package.^{84, 85} For issues concerning 2D vs 3D structures and possible corrections to the adsorption energy, the Heyd-Scuseria-Ernzerhof (HSE06) hybrid exchange-correlation functional³⁶ also was

used to confirm and verify our results. The unit cell typically was $25 \times 25 \times 25$ ($\text{\AA} \times \text{\AA} \times \text{\AA}$) with only the gamma point in the first Brillouin zone. Tests have been performed to guarantee that clusters are isolated from neighboring images for both neutral and charged systems. For charged clusters, a jellium background with dipole corrections⁸⁶ was used to screen out long-range Coulomb interactions properly. To reach the energy convergence of charged clusters when using HSE06, unit cells of some systems were enlarged to $30 \times 30 \times 30$ ($\text{\AA} \times \text{\AA} \times \text{\AA}$). A 500 eV cut-off energy was used to truncate the plane-wave basis and ensure precision better than 1 meV/atom in the total energy. Structural optimizations were performed using PBE energy functional with an energy convergence of 10^{-5} eV/cell and atomic force convergence of 0.02 eV/ \AA , respectively. Finally, the Bader method⁸⁷ was used for charge analysis.

The calculated nitrogen adsorption energy is defined as

$$E_{ad} = -E_{total} + E_{Ag_n^+} + E_{(N_2)_m} \quad (3-1)$$

and the co-adsorption energy as,

$$E_{ad} = -E_{total} + E_{Ag_nO_2^+} + E_{(N_2)_{mN}} \quad (3-2)$$

where E_{total} is the total energy of cation with adsorbents, m represents the number of N_2 molecules, and $E_{Ag_n^+}$ and $E_{Ag_nO_2^+}$ are total energies of Ag_n^+ and $Ag_nO_2^+$ cations without adsorbents, respectively.

3.2 Results and Discussion

3.2.1 Structure of Pristine Ag_n Clusters

To understand N_2 adsorption, it is necessary to understand structures of pure silver cations. We therefore have revisited structures of Ag_n^+ ($n=5-7$) using the

computationally expensive HSE06 hybrid functional as implemented in the VASP package.

Table 3-1 lists binding energies of both neutral clusters and cations. For neutral clusters, PBE and HSE06 are in agreement qualitatively. For $n=5$, the planar bowtie is most stable (Figure 3-2 c5), followed by the bi-pyramid (Figure 3-2 b5) and the twisted bowtie (Figure 3-2 a5, 3D). When ionized, the most stable and the least stable isomers swap shapes and the bi-pyramid remains as the second stable isomer. It is interesting to note that for both ionized and neutral clusters the energy difference between the first and second configuration is much smaller than between the second and the third. The two functionals, PBE and HSE06, predict the same geometry for cations.

For $n=6$, PBE and HSE06 also are in agreement with HSE06 for neutral clusters. The neutral cluster still prefers the 2D triangle structure (Figure 3-2 c6). There are also two 3D isomers including a rhombic wedge (Figure 3-2 a6) and a pyramid (Figure 3-2 d6). Upon ionization, PBE and HSE06 predict different ground state geometries. The planar structure (Figure 3-2 b6) is more stable than the others in the PBE calculations. When computed by HSE06, the rhombic wedge becomes the most stable shape. The planar (Figure 3-2 b6 and c6) geometries shift to second and third position in terms of stability. Differing from the pentamers, the energy differences among neutral hexamers are much larger than among the cations.

The heptamer, $n=7$ was analyzed using the same method. For the neutral cluster, HSE06 and PBE predictions again agree. The most stable geometry is the bi-pyramid (Figure 3-2 a7) followed by the cap (Figure 3-2 c7) and the hexagonal planar (Figure 3-2 b7). The 2D-3D transition of neutral Ag_n is in agreement with previous theoretical

Table 3-1. Total energy (TE), binding energy per atom (BE/n), and ionization potential (IP) obtained by using HSE (2nd and 3rd columns) and PBE (4th and 5th columns), respectively.

Ag_n^q (n, q)	Figure 3-2	TE-HSE	BE/n	TE-PBE	BE/n
(5,0)	a5	0.62	0.99	0.24	1.11
(5,0)	b5	0.08	1.02	0.08	1.14
(5,0)	c5	0	1.03	0	1.15
(6,0)	a6	0.96	1.12	0.90	1.259
(6,0)	b6	0.30	1.23	0.22	1.37
(6,0)	c6	0	1.28	0	1.409
(6,0)	d6	0.44	1.21	0.37	1.348
(7,0)	a7	0	1.123	0	1.434
(7,0)	b7	0.35	1.258	0.40	1.377
(7,0)	c7	0.22	1.275	0.27	1.395
			IP		IP
(5,1)	a5	0	5.11	0	5.36
(5,1)	b5	0.16	5.54	0.03	5.62
(5,1)	c5	0.24	5.73	0.48	5.98
(6,1)	a6	0	5.72	0.02	6.22
(6,1)	b6	0.09	5.59	0	5.88
(6,1)	c6	0.20	6.44	0.15	6.76
(6,1)	d6	0.37	6.82	0.18	7.01
(7,1)	a7	0	5.60	0.10	5.78
(7,1)	b7	0.002	5.26	0	5.38
(7,1)	c7	0.114	5.50	0.23	5.78

Note: All energies are in units of eV and shifted to zero for the lowest energy state. The letter *a5-c7* denotes clusters size $n=5-7$ and various isomer structures shown in Figure 3-2; the superscript *q* indicate the charge state. Numbers in *italic* refer to the lowest isomer.

studies. Like all above-mentioned cases, HSE06 and PBE predict similar trends and order of magnitude energy differences among all heptamers. However, the situation is very different for the cations. According to HSE06, the bi-pyramid(Figure a7) and the planar configurations tie to be most stable, and the cap-shaped (Figure 3-2 c7) isomer

is only slightly less stable (by 0.12 eV). Meanwhile, PBE predicts the planar (Figure 3-2 b7) form to be most stable, followed by the pyramid and the cap.

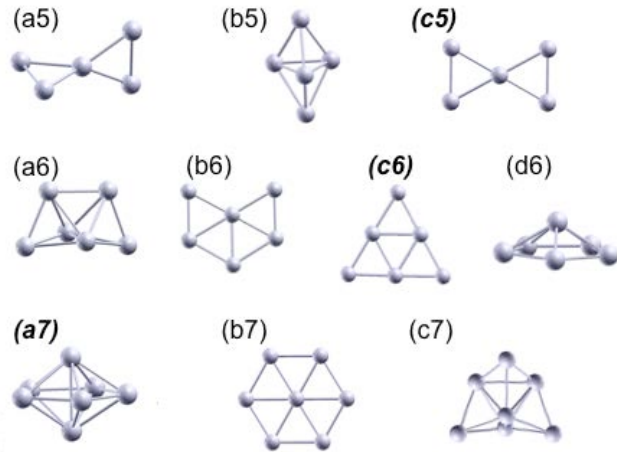


Figure 3-2. Structure of Ag_n ($n=5-7$) neutral clusters and cations. The structures (a) in the left column are the most stable ions. (a-d) indicates decreasing stability of the ions. Italic indicates the most stable neutral structures. The energetics and IP potential are listed in Table 3-1 for two different DFT approximations.

So, the hybrid functional seems to correct a slight PBE bias for the 2D structure when treating noble metal clusters. It also predicts systematically smaller binding energies and smaller ionization potentials (IP). Therefore, PBE is still a very good approximation for studying the trends in clusters. As a reference point, PBE and HSE06 predict the ionization energy of a single Ag atom as 7.93 and 7.59 eV, respectively, compared to the experimental value of 7.57 eV.⁸⁸

3.2.2 Physisorption of N_2 Molecules

After clarification of the structures of pristine clusters, we can discuss results of N_2 adsorption. Figure 3-3 depicts adsorption geometries for a few selected clusters to illustrate the physical picture. We first focus on trimer and tetramer cations since they are directly related to the experimental results.⁶¹

Table 3-2. Total energy (TE) and adsorption energy per N_2 molecule (AE/m) obtained by using HSE (2nd and 3rd columns) and PBE (4th and 5th columns), respectively.

$Ag_n(N_2)_m^+$ <i>(n,m)</i>	<i>Figure 3-4</i>	TE-HSE	AE/m	TE-PBE	AE/m
(3,1)	a	0	0.36	0	0.43
(4,1)	b	0	0.30	0	0.40
(4,1)	c	0.12	0.18	0.12	0.28
(6,1)	d	0	0.31	0	0.45
(6,1)	e	0.21	0.10	0.25	0.20
(6,1)	f	0.23	0.09	0.25	0.20
(7,1)	g	0	0.35	0	0.43
(7,1)	h	0.21	0.14	0.27	0.16
(7,6)	i	0	0.19	0	0.22
(7,6)	j	0.26	0.14	0.35	0.17
(7,6)	k	0.44	0.12	0.31	0.16

Note: All energies are in units of eV and shifted to zero for the lowest energy state. The letters a-h refers to various isomer structures and the superscript q to charge states. Numbers in italics refer to the lowest isomer.

The first part of Table 3-2 (rows with $m=1$) shows our calculated total energies and adsorption energies of Ag cations relative to states of lowest energies. For $n=3$, the problem is straightforward. There is only one geometric arrangement (Figure 3-3 a). The adsorption energy is 0.43 eV from PBE and 0.36 eV from HSE06 and the same degree of reduction applies to all clusters. The energy gain by adding the second N_2 to a trimer cation is 0.39 eV. For $n=4$, there are two inequivalent sites as shown in Figure 3-3 b-c. Our calculations (via PBE) show that N_2 prefers an obtuse corner over an acute one by 0.12 eV, or 0.40 vs. 0.28 eV. This is different from O_2 physisorption on Ag_4^+ , in which an acute corner is preferred, although it is not the ground state (Table 3-2, Figure 6g-h). When three or four corners are all occupied by three or four N_2 molecules, the total

energy gain is 1.02 and 1.24 eV, respectively. Note that when the corners are all occupied, the total adsorption energy is 110 meV less than merely counting the number of sites and adding up single bond energies. In contrast with the coadsorption of oxygen and nitrogen, nitrogen molecules on different sites of the same cluster do *not* enhance but reduce the binding of each other. Whereas oxygen and nitrogen act cooperatively, nitrogen molecules act mutually competitively.

For the hexamer, we have studied three inequivalent N₂ adsorption sites in the 3D cluster as shown in Figure 3-3 d-f, in which the three sites are ordered from high to low adsorption energy. The adsorption energies are 0.45 eV, 0.20 eV, 0.20 eV for PBE, and 0.31 eV, 0.10 eV, 0.09 eV for HSE06, respectively. Adsorption for the geometry in Figure 3-3 d is about 0.2 eV stronger than the other two geometries by both functionals.

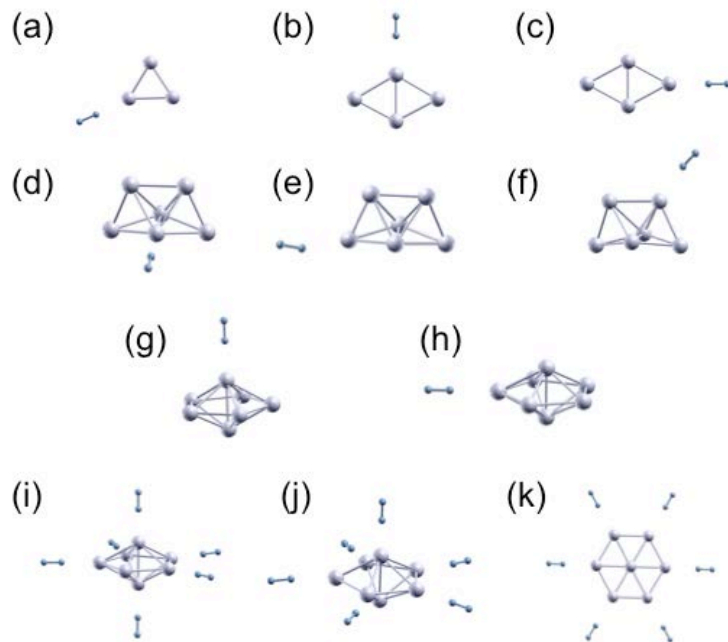


Figure 3-3. N₂-adsorption on Ag_n⁺ ($n=3, 4, 6, 7$). Both PBE and HSE06 XC were used. Results are listed in Table 3-2. The physisorption to sites at obtuse corners with high coordination number is found to be stronger than to those at acute ones.

Next we present our calculations on the silver heptamer cation, with its interesting and controversial 2D vs. 3D feature. For single N₂ adsorption on the ground state heptamer of bipyramidal geometry, there are two inequivalent sites, the top site and the side site (Figure 3-3 g-h). We notice that N₂ favors the top site of a cation. This preference is consistent with what is observed in the Ag tetramer and hexamer cation, in which an obtuse corner is preferred. Similar to Ag₄⁺, we also observe the competitive effect when multiple N₂ molecules are adsorbed on Ag₇⁺. The total binding of N₂ molecules on top and bottom sites is 20 meV less than twice the binding of one molecule on one of the two sites. The total binding of four N₂ molecules in the middle plane in Figure 3-3 i is 130 meV less than four times the binding of one N₂ in the plane (with top and bottom sites occupied).

Magic numbers have been observed at two physisorbed nitrogen molecules for Ag₇⁺ as well as for Ag₆⁺ in experiments.⁶¹ This is consistent with the calculated most stable 3D-isomers and with the nitrogen preference for obtuse corners, since only those isomers have two sites on obtuse corners with high-coordinated Ag-atoms.

The second part of Table 3-2 (rows with $m=6$) lists energies of Ag₇ with six nitrogen molecules. The number $m=6$ is chosen to compare the 3D bipyramidal (Figure 3-3 i-j) with the planar geometry (Figure 3-3 k). For 6-N₂ on a bipyramidal, there is a vacant site. Adsorption on the cation gives rise to 0.1-0.2 eV/molecule of adsorption energy. Adsorbed with six nitrogen molecules, the total energy of an Ag₇⁺ bipyramidal is clearly more stable than for the 2D structure, lower by 0.44 eV for HSE06 and 0.31 eV for PBE than planar cations. This difference indicates that N₂ molecules can stabilize the 3D structure and hence exert a non-negligible effect.

3.2.3 Chemisorption of O₂ Molecules

Figure 3-4 depicts O₂ adsorption on Ag_{*n*}⁺ for *n*=1-6. For *n*=1-3, there is one stable configuration which is physisorbed in nature. The oxygen molecule lies in the same plane as the silver ions. The adsorption energies are 0.45, 0.26, and 0.23 eV, respectively, and charge transfers are essentially zero (Table 3-3). The adsorption energy is computed according to Equation 3-1 but replacing N₂ by O₂ and setting *m*=1. For comparison, we have performed a calculation on a trimer using the HSE06 functional. The calculated adsorption energy is 0.16 eV, 0.07 eV lower than the PBE treatment. For *n*>3, we have obtained multiple isomers. The most interesting case is Ag₄⁺, since the lowest energy state upon O₂ adsorption corresponds to a 3D structure (Figure 3-4 d), which is different from a pristine Ag₄⁺ planar rhombus. The next three isomers with 2D geometry are shown in Figure 3-4 f-h. The isomer in Figure 3-4 f has charge transfer and adsorption energy both lower than the ground state cluster, and the clusters in Figure 3-4 g-h follow exactly the same pattern. We therefore can conclude that among isomers of a given size cluster, adsorption state energy and charge transfer are correlated and that measurements of one signal the other. The substantial difference between trimers and tetramers can be explained simply by the number of electrons in the two cations. In Ag₃⁺ the two s-electrons are spin-paired but in Ag₄⁺ there is a spin-unpaired electron. The calculated O₂ bond lengths are 1.23 Å in free space, 1.24 Å in Ag₃⁺O₂, and 1.31 Å in Ag₄⁺O₂, respectively.

Calculations on O₂-adsorbed Ag₅⁺ (Figure 3-4 i-m) and Ag₆⁺ (Figure 3-4 n-q) cations also indicate interesting physical processes in these small clusters. Similar to trimers and tetramers, respectively, pentamers and hexamers have even and odd number of electrons. It is expected that an O₂ binds to a pentamer more weakly than to

a haxamer as shown in Table 3-3. Nevertheless, there is a sizable charge transfer in pentamers, which is not the case in trimers. This difference reflects the fact that the size does matter when dealing with clusters. The adsorption energy of a pentamer increases by 40 meV from the value of a trimer, and the O₂ bond length is 1.26 Å, or 2% longer than that of a trimer. Interestingly, and contrary to Ag₄⁺O₂, the O₂-adsorbed Ag₅⁺ is a planer.

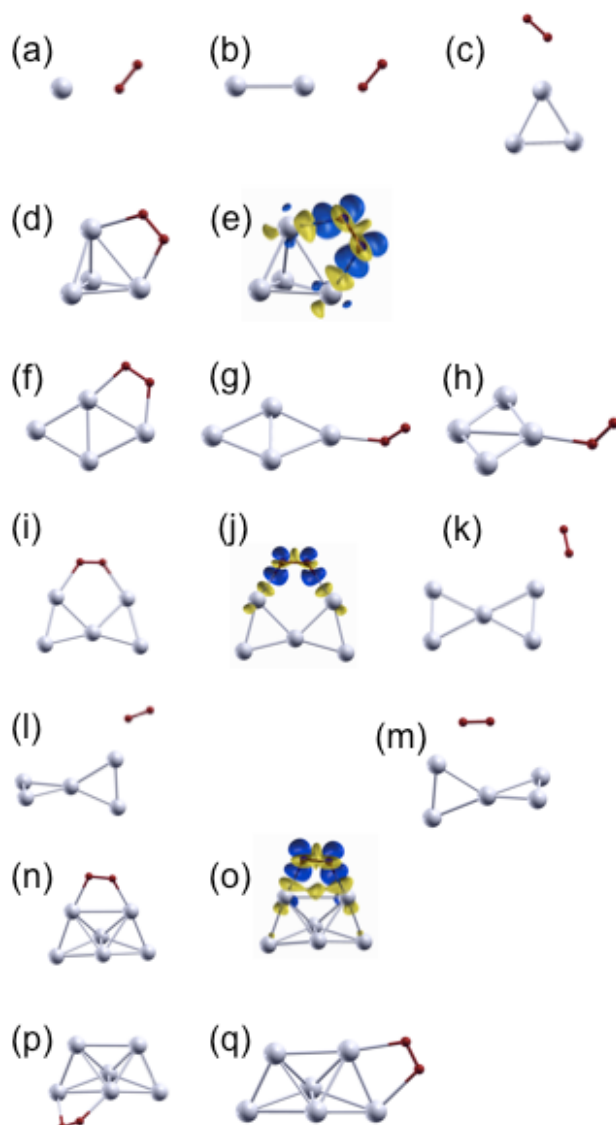


Figure 3-4. O₂-adsorption on Ag_n⁺ ($n=1-6$) cations. Small spheres represent O atoms and large ones Ag. For $n=4-6$, isosurfaces of charge difference (at the value of 0.02 e⁻/Å³), are plotted for the ground state cluster. The blue (darker) color

represents electron accumulation and yellow (lighter) deficiency. The adsorption energies and the Bader charge transfer are listed in Table 3-3.

The hexamer shows the strongest adsorption energy and the hexamer ground state also has the largest charge transfer among all the small clusters. This trend agrees with experimental observation.⁶¹ The bond length of the oxygen molecule is 1.33 Å, 8% larger than that of a free oxygen molecule, clearly indicating a chemisorption state. Without repeating the tedious effort we made to understand Ag_4^+O_2 , we have determined that enhanced co-adsorption should occur in the hexamer and other large clusters based on the same mechanisms as in the tetramer.

Table 3-3. Adsorption energy and charge transfer to O_2 molecules adsorbed on Ag_n^+ cations. The lowest energy states are written in italic.

n	adsorption energies and charge transfers of isomers (a)-(h) (Figure 3-4)			
1	(a) 0.45, none			
2	(b) 0.26, none			
3	(c) 0.23, none			
4	(d) 0.62, 0.41	(f) 0.35, 0.33	(g) 0.29, 0.18	(h) 0.15, 0.08
5	(i) 0.27, 0.20	(k) 0.18, none	(l) 0.18, none	(m) 0.12, none
6	(n) 0.81, 0.52	(p) 0.51, 0.39	(q) 0.33, 0.24	

Note: To put the charge state into perspective, our test calculation shows that the Bader analysis gives a 0.8 e- charge transfer for a NaCl unit. All energies are in eV and charge transfer in e-.

3.2.4 (N_2)_n- O_2 Co-adsorption on Ag_4^+

With clues obtained from experimental data, we have carried out an extensive search for the cluster structure and adsorption configurations. Figures 1b-c show the cooperative effect in coadsorption of N_2 and O_2 for the example of Ag_4^+ .

Figure 3-5 a-d depict the lowest energy adsorption states of Ag_4O_2^+ with 2-5 N_2 molecules and Figure 3-5 e-h show Ag_4^+ with 2-5 N_2 . Compared to E_{ad} (Equation 3-1), the calculated E_{ad-co} (Equation 3-4) for $m=2-5$ are 48, 35, 5, and 14 meV higher, indicating a small but clear enhancement. Compared to cation Ag_4O_2^+ without N_2

adsorption, the charge transfer from Ag_4^+ to O_2 increases by 0.01, 0.06, 0.12, and 0.12 electron, respectively. The enhancement in both energy and charge transfer is accompanied by an O_2 bond length increase of 0.00, 0.01, 0.02 and 0.02 Å, respectively. In addition, our calculated binding energies of N_2 molecules on Ag_4^+ are in good agreement with previous theoretical and experimental studies.^{88, 89}

One very subtle point needs to be mentioned: the first two N_2 , on the opposite side from the O_2 (Figure 3-5 a), contribute adsorption energy merely through electrostatic energy, but the two N_2 on the side of O_2 (near the oxygen molecule, Figure 3-5 c) affect charge transfer to the molecule and thus the O_2 bond length. Therefore, the fifth N_2 adsorption gains more energy compared to the fifth N_2 in the cluster without an O_2 . The observed enhancement in nitrogen-oxygen co-adsorption involves complex mechanisms.

We have also performed calculations of $\text{O}_2\text{-}(\text{N}_2)_2$ co-adsorption on Ag_3^+ clusters. An 18 meV enhancement in adsorption energy has been found due to the existence of an O_2 molecule, but there is no charge transfer even with the two N_2 molecules.

Our calculated results agree qualitatively with the experimental trend that oxygen molecules can increase the average number of adsorbed N_2 molecules and vice versa; the N_2 induces further charge transfer from Ag_4^+ core to the O_2 molecule.

3.3 Summary and Conclusion

Our comparative studies on two exchange-correlation functionals, PBE and HSE06, show that PBE is able to capture most of the trends in adsorption processes. The only failed predictions are the planar structures for Ag_6^+ and Ag_7^+ . Calculated with a hybrid functional they are found to be 3D in agreement with the experimentally deduced

nitrogen adsorption abundances and with earlier ion mobility experiments.⁶¹ The HSE06 functional provides, additionally, a better ionization potential.

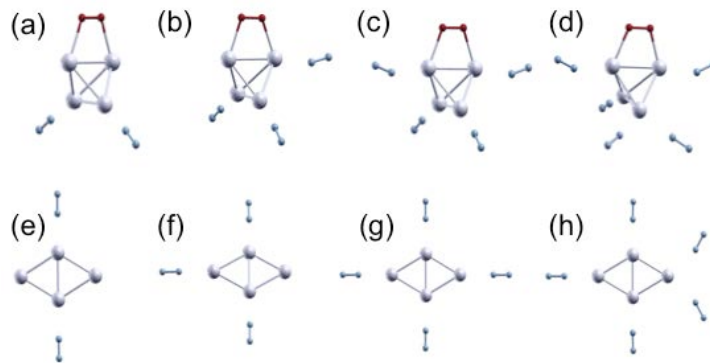


Figure 3-5. The lowest energy states of $\text{Ag}_4\text{O}_2^+-(\text{N}_2)_m$ and of $\text{Ag}_4^+-(\text{N}_2)_m$ with $m=2-5$, respectively.

For adsorption of nitrogen molecules, polarization dominates the process resulting in exclusively physisorption states. We found that the physisorption to sites at obtuse corners is stronger than for those at acute ones. This is opposite to findings of earlier experiments on neutral clusters. In charged clusters different sites differ in the distance to the charge center. Typically, sites on obtuse corners are closer to the charge center than acute ones. This effect enhances the adsorption on obtuse corners and is therefore opposite to the one described in the literature. For the same reason the nitrogen physisorption tends to decrease with increasing cluster size, as seen in experiment as in our calculations. Since the relative distances of sites to the charge center in the small silver-cation clusters vary strongly, their impact on the binding of nitrogen is more important than the effect of field enhancement on acute corners that was noticed in earlier studies on neutral and bigger clusters. Based on this, experimentally observed abundances in the number of adsorbed nitrogen molecules

were used to confirm the 2D-3D transition, as predicted based on hybrid functional results.

As we have seen in the Ag_4^+ and Ag_7^+ cases, physisorption of nitrogen is a competitive effect. The binding of nitrogen to any site is reduced by the presence of other nitrogen molecules on other sites.

For oxygen molecules, a transition from physisorption to molecular chemisorption occurs with $n > 3$, which is accompanied by charge transfer from cations to the O_2 and O_2 bond elongation. For a given size of cluster, the binding energy increases as charge transfer increases among various isomers. The amount of charge transfer displayed a pattern which coincides with even-odd number of s-electrons in the cation clusters.

We have used Ag_4^+O_2 as an example to show that nitrogen and oxygen coadsorption is a cooperative effect. The enhancement mechanism is, however, neither simple nor straightforward. First, the N_2 adsorption energy of some sites far from O_2 increases when there is an O_2 adsorbed on a Ag_n^+ without inducing extra charge transfer to O_2 . Second, when sites near O_2 are also occupied, the charge transfer to O_2 and the O_2 bond length both increase but the adsorption energy stays comparable to pure N_2 adsorption. Third, an N_2 -induced extra charge transfer results in enhanced binding for the second adsorption shell.

It is important to keep in mind that the energetic information does not include effects caused by kinetics and dynamics during evaporation processes, as occur in experiments where vibrational frequencies are also important. Nevertheless, energetics and charge transfer capture the essential physics underlying the adsorption state and adsorption process.

Our investigations on silver should also shed light on co-adsorption in gold clusters and nano-particles. The physisorption (N_2) induced strengthening of chemisorption (O_2) is of great general interest in nano-catalytic processes.

CHAPTER 4

ENHANCE OF AG CLUSTER MOBILITY ON AG SURFACE BY CHLORIDIZATION

The interactions between nanostructures and chemical additives in ambient environment can lead to many interesting phenomena. These interactions are of fundamental importance to nanostructure resistance to aging and consequently to system stability. Extensive experimental and theoretical work has been done on relevant phenomena such as metal surface coarsening, chemisorption-induced surface reconstruction, nano-cluster fragmentation, etc.⁹⁰⁻⁹⁷

Chalcogens (mainly, sulfur and oxygen), commonly used as additives, have been found to enhance the coarsening of Ag and Cu surfaces. Shen *et al.*⁹⁶ have observed accelerated coarsening of an Ag(111) surface if the sulfur coverage exceeds the critical value of 0.01 monolayer in experiment. They have proposed several surface units (in the form of Ag_nS_m) to explain the phenomenon, supported by DFT calculations.²⁸ Similar investigations also have been done on Cu(111) surfaces by Feibelman,⁹³ who showed that the presence of sulfur significantly reduces the formation energy of Ag_n or Cu_n clusters ($n > 2$) when sulfur is added, and thus enhances the material mass transport significantly.

The use of preformed clusters as primary building blocks is a major tool in the building of new architectures such as dendritic structures at nanoscale.⁹⁸ It has been observed that the deposition of silver clusters with a diameter of a few nanometers leads to silver fractal islands. The fractal relaxation can be activated by using a surfactant, such as molybdenum oxide molecules, carried by silver clusters in a subsequent deposition.⁹⁹ The surfactant increases the surface diffusion processes that lead to fractal pearlizing fragmentation.⁹⁹ More recently, an experimental study¹⁰⁰ on

silver fractal aging shows sulfur and chlorine are the main impurities to play a role in fractal fragmentation. One possible explanation is that these additive molecules act as surfactants, which increase the surface diffusion of fractal arms, thereby leading to their fragmentation.

This chapter attempts to address the role of chlorine in the observed phenomena related to Ag nanostructures using first-principles DFT calculations. We have studied the effectiveness of mass transport and bond weakening, two fundamental aspects critical to corrosion and fragmentation, which are intertwined in the observed fractal degradation process. The enhancement of the mobility or the mass transport rate of Ag clusters has been demonstrated by Ag cluster diffusion on Ag(111) surfaces before and after chloridization. The decrease of interaction strength has been examined using a model that consists of two Ag_{55} clusters (details are discussed below).

The problem of Ag_n and Ag_nCl_m diffusion on silver surfaces is an interesting topic in the field of metal surfaces.¹⁰¹⁻¹⁰⁶ It is thus relevant to mention related theoretical work on transition and noble metal surfaces. A systematic study of surface structure, diffusion path and barriers of Al_n ($n = 1$ to 5) clusters on Al(111) surfaces was carried by Chang et al. using DFT.¹⁰² In the same paper, by use of the empirical embedded atom method (EAM), they calculated the diffusion barriers of a series of transition metals and noble metal clusters on (111) surfaces. Diffusion of Cu_n clusters on Cu(111) and Ag(111) surfaces also was studied using DFT.^{104, 105} To our knowledge, the diffusion behavior of Ag_n clusters and Ag_nCl_m clusters on Ag(111) surfaces has not been investigated at the first-principles level. Following the practice of previous work,^{93, 96} our calculations and

analysis have been focused on the comparison between the mobility of Ag_n and Ag_nCl_m clusters on Ag(111) surfaces.

The rest of this chapter is organized as follows: Section 4.1 describes our models and the first-principle calculation methods; Section 4.2 presents our results on Ag_n and Ag_nCl_m ($n = 1$ to 4) clusters on Ag(111) surface and the $(\text{Ag}_{55})_2$ dumbbell structures. Section 4.3 concludes the chapter.

4.1 Methods and Computational Details

All systems were investigated by DFT calculations with the spin-unrestricted PBE³¹ form of the GGA functional. We used the plane-wave basis set in conjunction with the PAW^{53, 83} potential as implemented in the VASP package.^{84, 85} A 500 eV cut-off energy was used to truncate the plane-wave expansion.

For the first part of the investigation, a seven-layer slab with the two bottom layers fixed was employed to simulate the Ag(111) surface, on top of which Ag_n and Ag_nCl_m cluster adsorption and diffusion was investigated. The choice of (111) surface orientation enables the study of both fcc and hcp adsorption sites. The thickness of the vacuum between the surface clusters and the neighboring metal surface was estimated to be larger than 15 Å. A $(2\sqrt{3} \times 2\sqrt{3})\text{R}30^\circ$ surface unit cell and a $(3 \times 3 \times 1)$ Monkhorst-Pack k-point mesh¹⁰⁷ was used. We define the formation energy E_f as

$$\begin{aligned} E_f(\text{Ag}_n\text{Cl}_m) = & n \times [E(\text{Ag}) + E_{ad}(\text{Ag})] \\ & + m \times [E(\text{Cl}) + E_{ad}(\text{Cl})] \\ & - [(E(\text{Ag}_n\text{Cl}_m) + E_{ad}(\text{Ag}_n\text{Cl}_m)], \end{aligned} \quad (4-1)$$

where E_{ad} is the surface adsorption energy, given by

$$E_{ad}(X) = E(X + \text{surface}) - E(X) - E(\text{surface}), \quad (4-2)$$

where X can be a single Ag or Cl atom, or an Ag_nCl_m cluster. The formation energy describes the energy gain for assembling an Ag_nCl_m cluster on an Ag(111) surface from separately adsorbed atoms. It affects the relative population of a given size of Ag_nCl_m cluster on a surface. Low formation energy correlates to a high population. Note that our definition of formation energy differs from that in studies of surface coarsening,^{93, 96} which used the difference between the adsorption energy of an Ag adatom on a pure surface and on the edge of an Ag island. Since the difference is a constant per Ag atom, our definition of formation energy provides a good criterion for evaluating the relative population of different sizes of clusters.

For the second part of our investigation, we used an Ag_{55} dimer model, in which each Ag_{55} is a Mackay icosahedron. We used a $30 \text{ \AA} \times 20 \text{ \AA} \times 20 \text{ \AA}$ box and consider only the Γ -point. The binding energy of the dimer E_b is defined as

$$E_b = |E(\text{Ag}_{55}\text{Cl}_m)_2 - 2 \times E(\text{Ag}_{55}\text{Cl}_m)| \quad (4-3)$$

Structural optimizations were performed using an energy convergence of 10^{-5} eV/cell and atomic force convergence of 0.02 eV/\AA , respectively. For energy barrier evaluations, we performed nudged elastic band¹⁰⁸ (NEB) calculations. Five or seven images, including the starting and final images, were considered in the calculation, depending on the distance between starting and final images. The normal force was converged within 0.03 eV/\AA . Finally, the Bader method⁸⁷ was used for charge analysis.

4.2 Results and Discussion

4.2.1 Ag_nCl_m Clusters on Ag(111) Surfaces

The first part of our investigation addresses issues related to mass transport on Ag surfaces. We therefore studied adsorption of a number of Ag_n and Ag_nCl_m ($n = 1$ to 4)

clusters on Ag(111) surfaces. The important quantities are diffusion barriers of chloridized clusters on surfaces compared to pure Ag_n clusters. To avoid unnecessary complication, only clusters with stoichiometry $m=n$ were studied for $m \geq 3$. According to our calculations, an Ag_2Cl_2 cluster is not stable on an Ag(111) surface, but Ag_2Cl is. Figures 4-1 to 4-4 show the different surface states of Ag_n and Ag_nCl_m that are discussed in detail below, and Tables 4-1 and 4-2 summarize the calculated energies of surface states, formation energies, and diffusion energy barriers.

4.2.1.1 Ag Monomer and AgCl

There exist two locally stable sites for a single Ag adatom adsorption, fcc and hcp sites (Figures 4-1a and b, respectively). The fcc site is more stable than the hcp site by only 4 meV. The best diffusion path between fcc and hcp sites is the bridge crossing, with a 59 meV energy barrier. This barrier is about 20 meV higher than the value calculated using EAM. For AgCl, we have found that AgCl dissociated adsorption (Fig 4-1f), in which the AgCl bond is completely broken, is energetically more favorable than the configuration in which the Ag and Cl atoms are bonded, or AgCl cluster adsorption (Figure 4-1c). In the bonded configuration, AgCl with Ag at an fcc site (Figure 4-1c) is 60 meV higher than the dissociated state (Figure 4-1f), while AgCl with Ag at an hcp site (Figure 4-1d) is 72 meV higher. The intermediate stage (Figure 4-1e), in which the Ag and Cl are halfway dissociated (with an Al-Cl distance somewhere between 1c and 1f), is 66meV higher than the ground state. The diffusion barrier of AgCl as a cluster from Figure 4-1c to Figure 4-1d is 46meV, which is 13meV lower than the barrier for diffusion of a single Ag. This 22% difference is significant, since the mobility is an exponential function of the energy barrier. Furthermore, although the AgCl cluster is not the most stable structure on an Ag(111) surface, the dissociation barrier from Figure 4-1c to

Figure 4-1e is 72meV, which is 26 meV higher than the diffusion barrier. This means that once the Ag and Cl atoms form a cluster, the probability of diffusion as a cluster is higher than the probability of separation. The dissociation barrier from the configuration of Figure 4-1e to that of Figure 4-1f is 30 meV.

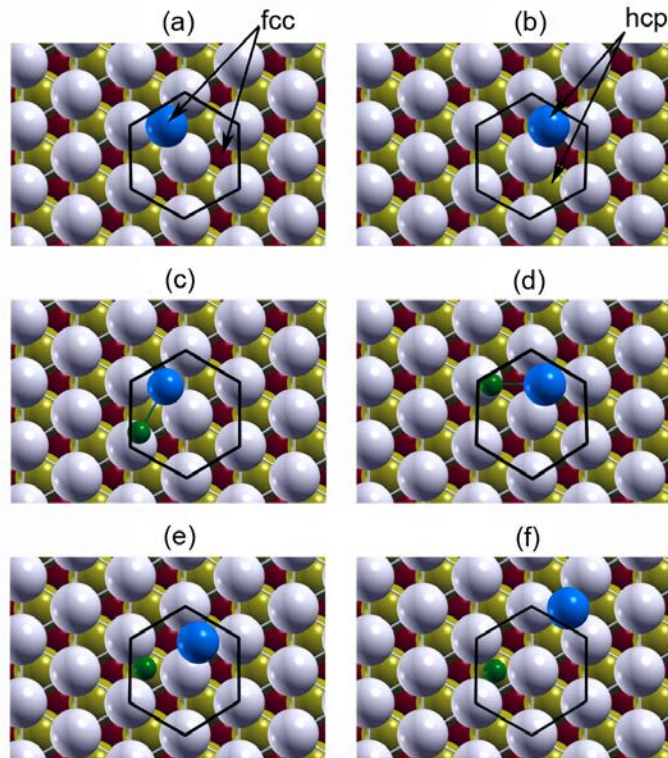


Figure 4-1. Ag adatoms and AgCl clusters or separately adsorbed adatoms on an Ag(111) surface: (a): an adatom on an fcc site. (b): an adatom on an hcp site. (c): an AgCl cluster with Ag at an fcc site. (d): an AgCl cluster with Ag at an hcp site. (e): an intermediate stage of AgCl separation. (f): Ag and Cl separated and adsorbed. Ag adatoms are in blue (dark) and Cl adatoms are in green (small, dark). The top layer of the Ag(111) surface is in light grey, while the second and third layer are in yellow (grey) and red (dark), respectively. Hexagons are used to illustrate the same positions in (a) to (f).

4.2.1.2 Ag dimer and Ag_2Cl

For Ag_2 clusters on an Ag(111) surface, three different configurations were studied. Figures 4-2a to 2c show fcc-fcc (FF), fcc-hcp (FH) and hcp-hcp (HH) adsorption geometries, respectively. Here, fcc-fcc refers to the arrangement with both Ag atoms

located at fcc sites and fcc-hcp refers to one Ag at fcc and one at hcp, etc. The ground state FF, is more stable than FH by 31 meV. The HH structure is 10 meV higher than the ground state. We investigated both local rotation and long-range intercell translation, as was done in reference15. The local rotation can be illustrated by Figure 4-2a → Figure 4-2b → Figure 4-2c. The energy barrier between configurations of Figure 4-2a and Figure 4-2b is 62meV, while that between configurations of Figure 4-2b and in Figure 4-2c is 55meV. However, this rotational motion does not allow the Ag dimer to diffuse into the next 7-Ag hexagon. Long-range intercell translation requires the center of mass of the two Ag atoms to move in a given direction continuously from one cell to the next Figure 4-2a → Figure 4-2d. Figure 4-2i shows that the cluster moves along a zigzag path. The calculated diffusion energy barrier of long-range motion is 123 meV. As mentioned previously, an Ag_2Cl_2 cluster is not a stable structure when placed on the Ag(111) surface, although this cluster is stable in vacuum. No energy barrier is found for one Cl atom to drift away from the cluster and find a stable adsorption site on the surface. The one Cl atom that stays in the cluster is located above the center of mass of the Ag dimer and forms an Ag_2Cl cluster. The surface structures of Ag_2Cl are shown in Figures 4-2 e-h. As was found for the Ag dimer, the most favorable state is FF. The energies of FH and HH structures are 6 and 13 meV higher than the ground state, respectively. Our calculations have found a 61 meV energy barrier during the local rotation shown in Figure 4-2d → Figure 4-2e, while a 62meV barrier has been obtained for the rotation shown in Figure 4-2e → Figure 4-2f. Compared to results for the Ag_2 dimer, the former is practically the same, but the latter is 7 meV higher. Thus, the local rotation dynamics is suppressed slightly by chloridization. In contrast, the intercell

translation is enhanced. We found an 8 meV decrease in the translational barrier height for Ag_2Cl compared to a pure silver dimer.

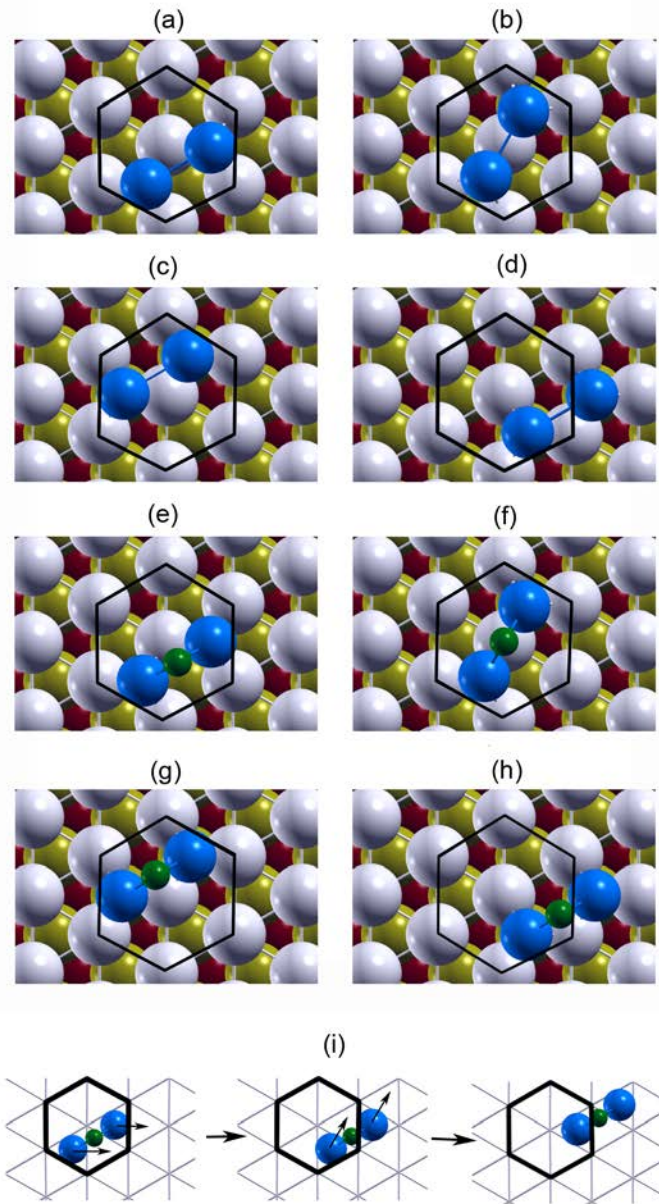


Figure 4-2. Ag dimer and Ag_2Cl clusters adsorbed on $\text{Ag}(111)$ surface: (a): Both Ag atoms are at fcc sites (FF); (b): One Ag atom is at an fcc site and the other is at a hcp site (FH); (c): Both Ag atoms are at hcp sites (HH); (d): Both Ag atoms in (a) diffuse together to hcp sites (HH'); (e)–(h): Different adsorption configurations of Ag_2Cl , with the same Ag patterns as (a)–(d), respectively. The Cl atom stays above the middle of the two Ag atoms. Panel (i) shows the translational motion of an Ag_2Cl cluster. The skeleton grid represents the top

Ag layer and the arrows point to the direction of the movement of Ag (and chlorine) atoms in each step.

4.2.1.3 Ag Trimer and Ag_3Cl_3

Four different surface configurations of Ag trimers exist on the Ag(111) surface, fcc_t (Figure 4-3a), fcc_h (Figure 4-3b), hcp_t (Figure 4-3c) and hcp_h (Figure 4-3d). Here, fcc or hcp refer to the adsorption site of Ag atoms, and t or h mean top or hollow, labeling the location of the center of mass of the cluster. Our calculations reveal that fcc_t and fcc_h configurations are nearly degenerate in energy, and so are the hcp_t and hcp_h configurations. The fcc_h structure is the ground state, 14meV lower than the hcp_t or hcp_h configurations. The energy barrier for the long-range diffusion from fcc_h to hcp_t is 178 meV, and the energy barrier between fcc_t and hcp_h is equally high.

In an Ag_3Cl_3 cluster in vacuum, Cl atoms prefer to bind at the edge sites of a triangle formed by the three Ag atoms. On an Ag(111) surface, Cl atoms remain at side sites, but somewhat buckled above the Ag_3 plane. Compared to an Ag trimer, an Ag_3Cl_3 cluster is more stable at the fcc_t (Figure 4-3e) and the hcp_t (Figure 4-3h) sites. These two sites are energetically equivalent, and they are 102 meV lower than the hcp_h (Figure 4-3f) site and 99meV lower than the fcc_h (Figure 4-3g) site. Unlike an Ag trimer, in which the positions of Ag atoms determine the ground state, the position of the center of mass is the critical factor to the cluster ground state. The calculated diffusion barrier is 159 meV for moving from fcc_t to hcp_h and 158 meV for moving from fcc_h to hcp_t , which is about a 20meV reduction from the diffusion barriers of a pure Ag trimer on the surface. The minimal energy diffusion path is again a zigzag path (Figure 4-3i).

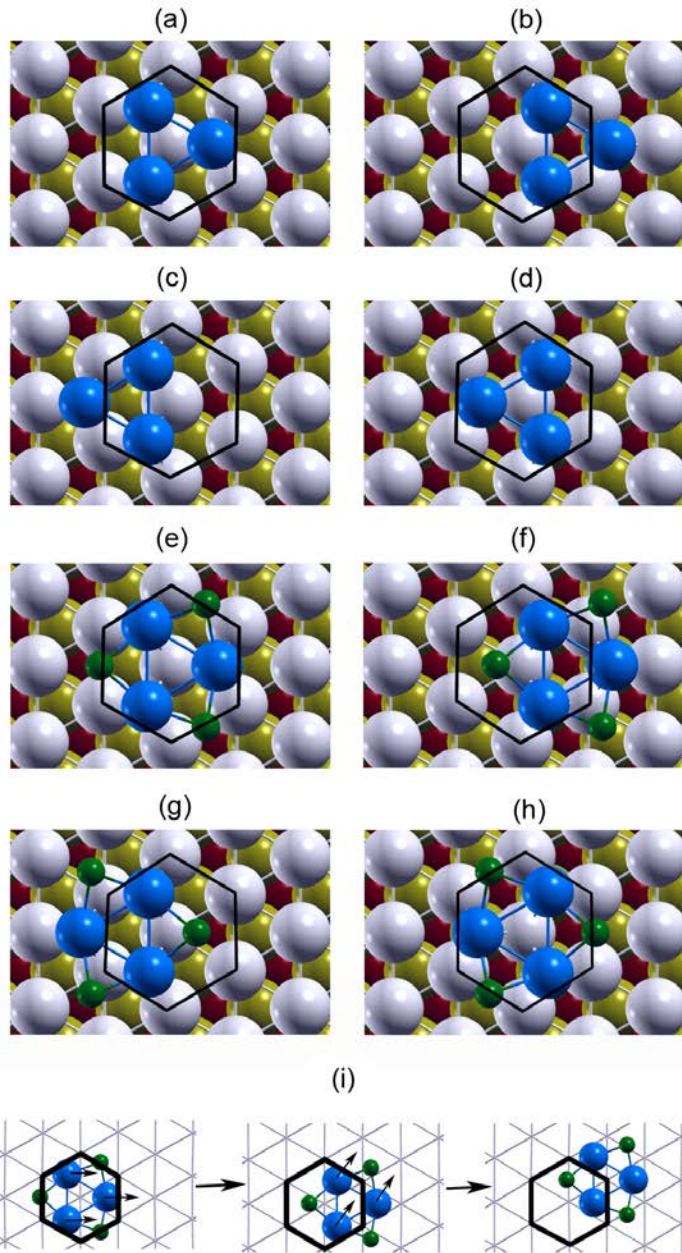


Figure 4-3. Ag trimers and Ag₃Cl₃ clusters adsorbed on an Ag(111) surface: (a): All three Ag atoms are at fcc sites and the center of mass is at the on-top site (fcct); (b): Ag atoms are at hcp sites and the center of mass is at the hollow site (fcch); (c): Ag atoms are at fcc sites and the center of mass is at the hollow site (fcch); (d): Ag atoms are at hcp sites and the center of mass is at the on-top site (hcpt). (e)–(h): Adsorption configurations of Ag₃Cl₃ with same Ag patterns as (a)–(d), respectively. Similar to Figure 4-2i, panel (i) shows the translational motion of Ag₃Cl₃ cluster.

4.2.1.4 Ag Tetramer and Ag_4Cl_4

The most stable Ag tetramer on the surface is a compact fcc structure with all Ag atoms sitting at fcc sites, shown in Figure 4-4a. We have denoted this configuration as 4F. This structure has an energy about 100 meV lower than the 4H geometry, in which all Ag atoms are located at hcp sites (shown in Figure 4-4c). The diffusion between 4F and 4H can be realized by moving four Ag atoms together, or by a two-at-a-time motion, which we label ‘maneuvering’, through an intermediate 2F2H state, shown in Figure 4-4b. Along the first path, the calculated energy barrier is 225meV. The second path was studied by Chang¹⁰² to explain the surface diffusion barrier drop from trimer to tetramer for $\text{Ir}_n/\text{Ir}(111)$ and $\text{Ni}_n/\text{Ni}(111)$ systems, in which this motion has lower barriers than the corresponding trimmers. The same mechanism treated by DFT also explained the $\text{Al}_n/\text{Al}(111)$ system. However, in the case of $\text{Ag}_n/\text{Ag}(111)$, the 2F2H structure is 207meV higher than the 4F state and the barrier through the second path is 218meV, just slightly lower than the first path and significantly higher than the EAM result.

Chloridized Ag tetramers behave quite differently from the pure metal ones. The ground state of Ag_4Cl_4 is the 2F2H structure Figure 4-4d, which is 127 meV lower than the 4F structure Figure 4-4e. Figure 4-4f also shows a different 2F2H state, which can be obtained by shifting the Ag atoms on the left side upward in Figure 4-4e. Figure 4-4g illustrates the diffusion path of the Ag_4Cl_4 . The first three steps correspond to Figure 4-4d, 4e and 4f. As shown in the path, only two of the four Ag atoms move at each step, finally achieving a step in the direction of diffusion. This complicated maneuvering path has a 153 meV barrier, which is much lower than the barrier of translational motion for the Ag tetramer.

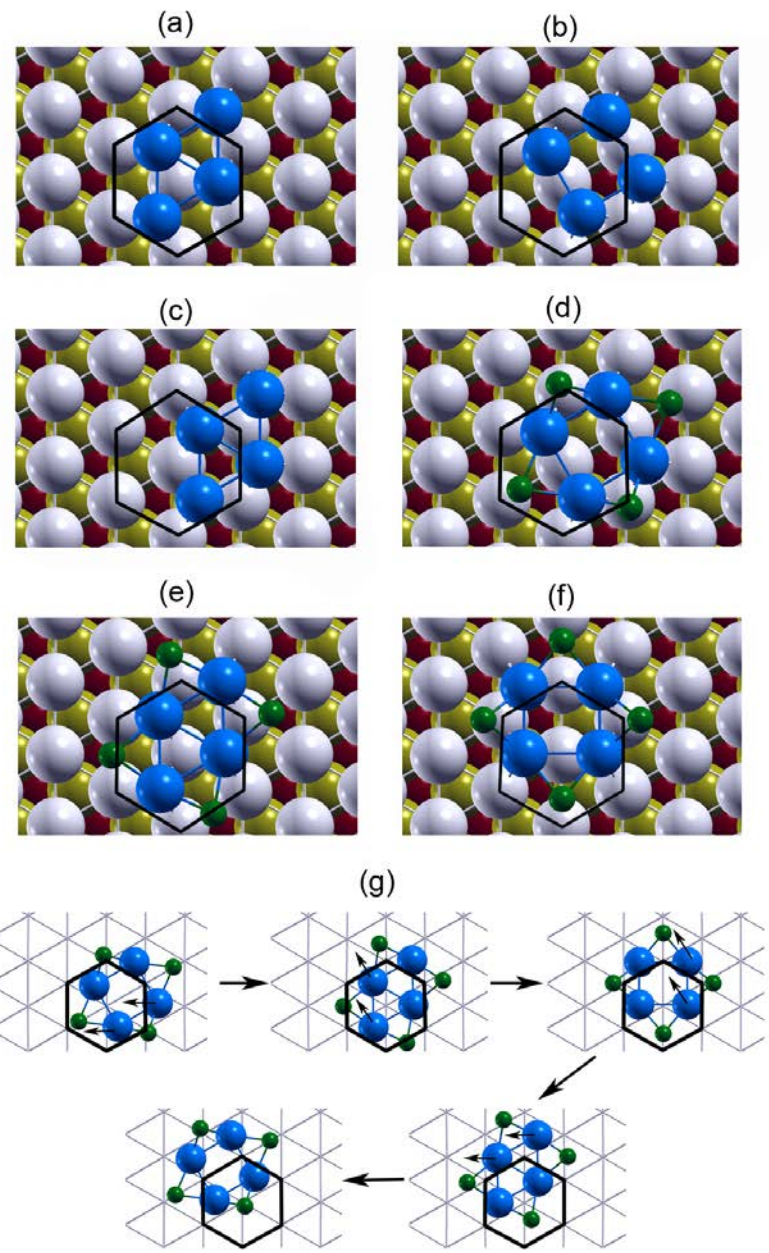


Figure 4-4. Ag tetramers and Ag₄Cl₄ clusters adsorbed on an Ag(111) surface: (a): Ag atoms are at fcc sites (4F); (b): Two Ag atoms are at fcc sites and the other two are at hcp sites (2F2H); (c): Ag atoms are at hcp sites (4H); (d): 2F2H structure of Ag₄Cl₄; (e): 4F structure of Ag₄Cl₄; and (f): 2F2H structure of Ag₄Cl₄, with the cluster shifted from (d). Panel (g) shows the diffusion path of Ag₄Cl₄. Again, the skeleton grid represents the top Ag layer. The arrows depict the movement of Ag atoms in each step. Chlorine atoms just follow.

Table 4-1. The energies E and formation energies E_f (in meV) of Ag_n and Ag_nCl_m clusters on an Ag(111) surface. The ground state energy of each cluster is set to zero.

cluster	Adsorption site	E (meV)	E_f (meV)
Ag	fcc (4-1a)	0	0
	hcp (4-1b)	4	4
Ag_2	FF (4-2a)	0	-114
	FH (4-2b)	32	-83
	HH (4-2c)	10	-104
	HH' (4-2d)	10	-104
	fcc _t (4-3a)	3	-491
	hcp _h (4-3b)	14	-480
Ag_3	fcc _h (4-3c)	0	-494
	hcp _t (4-3d)	14	-480
	4F (4-4a)	0	-919
Ag_4	2H2F (4-4b)	207	-712
	4H (4-4c)	100	-819
AgCl	fcc (4-1c)	60	-3
	hcp (4-1d)	72	8
	mid_stage (4-1e)	66	3
	separate (4-1f)	0	-63
Ag_2Cl	FF (4-2e)	0	551
	FH (4-2f)	6	557
	HH (4-2g)	13	564
	HH' (4-2h)	13	564
	fcc _t (4-3e)	0	-843
	hcp _h (4-3f)	102	-741
Ag_3Cl_3	fcc _h (4-3g)	99	-744
	hcp _t (4-3h)	0	-843
	2H2F (4-4d)	0	-1392
Ag_4Cl_4	4F (4-4e)	127	-1265
	2H2F' (4-4f)	2	-1390

4.2.1.5 Formation Energies

Formation energies of Ag_nCl_m are listed in Table 4-1. Only the ground states are discussed except for $n=1$, since the ground state is dissociated adsorption, which is not the focus of this chapter. For $n=m=1$, the formation energy of an AgCl cluster is -3 meV, which means that adsorption of an AgCl cluster is almost comparable to that of a single Ag adatom. For $n=2$, $m=1$, the formation energy is 551 meV, which is much higher than

that of an Ag dimer (-114meV). The positive sign in the formation energy means that the cluster is energetically higher than the fragmented state while adsorbed on the surface. The ground states of both Ag_3Cl_3 and Ag_4Cl_4 have negative formation energies, -843 meV and -1392 meV , respectively, or -281 meV and -348 meV per AgCl unit. Both values are significantly lower than the corresponding Ag clusters without chlorine. Based on the formation energies, one can predict that silver surface coarsening can be accelerated by chlorine. One can also expect that Ag_3Cl_3 and Ag_4Cl_4 have higher population than AgCl and Ag_2Cl clusters on the surface, and thus are good candidates as basic surface diffusion units.

Table 4-2. Diffusion barriers E_d of Ag_n and Ag_nCl_m clusters on an Ag(111) surface. All energies are in meV.

cluster	transition	E_d	clusters	transition	E_d
Ag	$1\text{a} \leftrightarrow 1\text{b}$	59	AgCl	$1\text{c} \leftrightarrow 1\text{d}$	46
Ag_2	$2\text{a} \leftrightarrow 2\text{b}$	62	Ag_2Cl	$1\text{c} \leftrightarrow 1\text{e}$	72
	$2\text{b} \leftrightarrow 2\text{c}$	55		$2\text{e} \leftrightarrow 2\text{f}$	61
	$2\text{a} \leftrightarrow 2\text{d}$	123		$2\text{f} \leftrightarrow 2\text{g}$	62
Ag_3	$3\text{a} \leftrightarrow 3\text{b}$	178	Ag_3Cl_3	$2\text{e} \leftrightarrow 2\text{h}$	115
	$3\text{c} \leftrightarrow 3\text{d}$	178		$3\text{e} \leftrightarrow 3\text{f}$	159
Ag_4	$4\text{a} \leftrightarrow 4\text{b}$	216	Ag_4Cl_4	$3\text{g} \leftrightarrow 3\text{h}$	158
	$4\text{b} \leftrightarrow 4\text{c}$	218		$4\text{d} \leftrightarrow 4\text{e}$	153
	$4\text{a} \leftrightarrow 4\text{c}$	225		$4\text{e} \leftrightarrow 4\text{f}$	149

4.2.2 $(\text{Ag}_{55})_2$ dumbbell structure

In the second part of our investigation we studied the Ag_{55} Mackay icosahedron and $\text{Ag}_{55}\text{-Ag}_{55}$ dumbbell dimer structure (Figure 4-5a), and we calculated the binding energies of $(\text{Ag}_{55})_2$ itself and with Cl or O adsorption (see Table 4-3). In the dumbbell structure, two Ag_{55} clusters are connected through two parallel facets, one of which is rotated 60 degrees with respect to the other one, mimicking fcc stacking. Our model

structure with Cl adsorption is $(\text{Ag}_{55}\text{Cl}_{19})_2$, with one Cl atom on each facet except for those in contact with the other cluster.

Table 4-3. Distance to the center of cluster (in Å) of each layer (labeled by L-Cl/O, L-1, L-2, and L-3) and change in charge (in e^-) in each layer. + means gaining electrons and - losing electrons.

	Layer_Cl/O	L_1	L_2	L_3
distance	Ag_{55}	5.54	4.84	2.80
	$\text{Ag}_{55}\text{Cl}_{19}$	6.65	5.65	4.95
charge	$\text{Ag}_{55}\text{O}_{19}$	5.78	5.53	5.17
	$\text{Ag}_{55}\text{Cl}_{19}$	+9.99	-2.59	-8.24
	$\text{Ag}_{55}\text{O}_{19}$	+17.40	-2.28	-15.46
				+0.37

Table 4-4. Binding energy (in eV) between two Ag_{55} -based clusters.

dimer	Binding energy
$\text{Ag}_{55}-\text{Ag}_{55}$	4.61
$\text{Ag}_{55}\text{Cl}_{19}-\text{Ag}_{55}\text{Cl}_{19}$	3.82
$\text{Ag}_{55}\text{O}_{19}-\text{Ag}_{55}\text{O}_{19}$	5.29

To construct an $(\text{Ag}_{55})_2$ dumbbell structure with Cl adsorption, we started with Cl adsorption on an Ag_{55} icosahedron. For single Cl atom adsorption on Ag_{55} , we found that the center hollow site of a facet has is the most stable site. The calculated adsorption energy is -3.33 eV, 25 meV more stable than the corner hollow site, which is the second most stable. Then, 19 Cl atoms were placed at the center hollow sites of 19 facets, with one facet left for binding with a second chloridized cluster to later form $\text{Ag}_{55}\text{Cl}_{19}-\text{Ag}_{55}\text{Cl}_{19}$. After optimization, some Cl atoms have diffused on facets and have deviated from the center hollow sites (Figure 4-5b). Meanwhile, the structure of Ag_{55} is significantly influenced by Cl atoms. The first part of Table III shows the average distance from each layer to the center of the Ag_{55} cluster. On average, with Cl atoms the surface and the second Ag layers are both 0.11 Å further away from the center than values without (2.0% and 2.3% expansion, respectively): the Ag_{55} cluster expands under chloridization. For comparison, an oxidized Ag_{55} with 19 O atoms, one on each

facet, also was studied. Our calculations show that oxygen atoms prefer to stay firmly at the center hollow sites, and they are closer to the center by 0.87 Å than Cl atoms.

Though the second layer expands by 0.33 Å (6.8%), the distance between the surface layer and the center of the cluster remains nearly unchanged. Charge (electron) analysis (see the second part of Table 4-3) shows that the second Ag layer contributes a much higher percentage of the total charge transferred to O than Cl atoms, which indicates the strong interaction between oxygen atoms and Ag atoms in the layer.

Based on the optimized $\text{Ag}_{55}\text{Cl}_{19}$, we then constructed the chloridized dumbbell structure, in the same way as the $(\text{Ag}_{55})_2$ construction described above. The optimization of the $(\text{Ag}_{55})_2$ geometry leads to a binding energy of 4.61 eV, but the binding energy of $(\text{Ag}_{55}\text{Cl}_{19})_2$ is 3.82 eV (reduced by 17%). Chloridization clearly weakens the bonding strength between the two Ag_{55} clusters in the dimer. For comparison, we calculated the binding energy of the oxidized dimer. Interestingly, the binding energy is 5.29 eV, higher than for both the pure silver cluster dimer and the chloridized cluster dimer, indicating a bond strengthening due to oxidation. Therefore, oxygen chemisorption on silver dendritic nanostructures does not enhance the fragmentation, but chlorine does.

4.3 Summary and Conclusion

To understand the enhancement of Ag nanofractal fragmentation by chlorine pollution, this chapter has presented a detailed density functional study of $(\text{Ag}_{55})_2$ dumbbell structures with and without chloridization, as well as surface diffusion of Ag_n and Ag_nCl_m ($n = 1$ to 4) clusters on Ag(111) surfaces. For a single Ag_{55} cluster, surface adsorption of Cl atoms tends to loosen the first two layers on the surface. We have shown that the binding energy between two Ag_{55} icosahedrons in the dumbbell structure

is reduced by 17% with surface coverage of chlorine (19 Cl atoms on each Ag₅₅). We have also demonstrated that Ag_nCl_m clusters are generally more mobile than Ag_n clusters on Ag(111) surfaces for n=1–4. The formation energies of Ag_nCl_m imply that Ag₃Cl₃ and Ag₄Cl₄ are good candidates as basic units for Ag surface diffusion in addition to the monomer AgCl; the energy barrier calculations indicate that AgCl and Ag₄Cl₄ have barriers substantially lower than their corresponding pure silver clusters, and Ag₃Cl₃ has a barrier slightly lower than Ag₃. Finally, our investigations also have uncovered diffusion paths of the clusters.

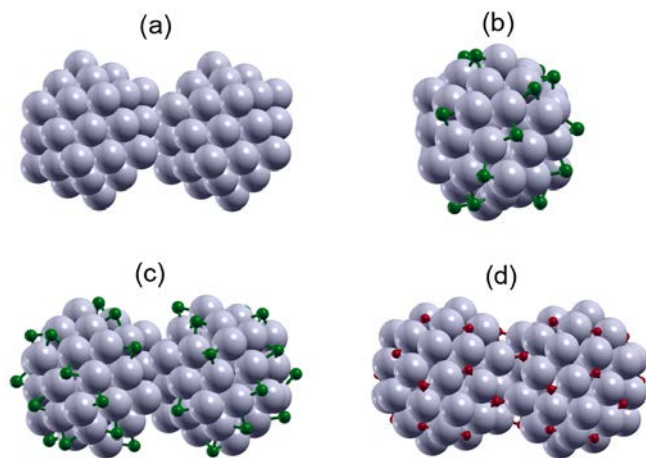


Figure 4-5. (a) Ag₅₅-Ag₅₅ dumbbell structure. (b) Optimized Ag₅₅Cl₁₉ structure. Green (small, dark) balls are Cl atoms. (c) Optimized (Ag₅₅Cl₁₉)₂ dumbbell structure. (d) Optimized (Ag₅₅O₁₉)₂ dumbbell structure. Red (small, dark) balls are O atoms.

Our theoretical investigation suggests that the enhancement of Ag_n surface mobility by chloridization explains the acceleration of fragmentation of silver nanofractals and the effects of those impurities in the aging process under ambient air.

CHAPTER 5

MOLECULAR MAGNETOCAPACITANCE

Quantum mechanical effects can change the capacitance of a mesoscopic capacitor by a contribution due to the density of states.¹⁰⁹ One quantum consequence is magnetocapacitance due to the asymmetry in the capacitance tensor elements under field reversal.¹¹⁰ On the nanoscale, quantum capacitance of a molecule may depend on the charge density distributions of the highest occupied molecular orbital (HOMO) and the lowest unoccupied molecular orbital (LUMO). For single molecule nano-magnets (SMM) and other magnetic nanosystems whose HOMO and LUMO are determined by their magnetic states, it is natural to expect that their self-capacitances are in turn dependent on their magnetic states. Such an effect, if proven to exist, will provide a much simpler path to achieve magnetocapacitance in nanoscale materials. By merely switching the magnetic state of a molecular nano-magnet, one can change its capacitance.

In this chapter, we demonstrate the concept of molecular magnetocapacitance based on first-principles calculations of single molecular nano-magnets. Molecular nano-magnets are stable at room temperature and can be crystallized or used in single-molecule tunneling junctions.¹¹¹⁻¹¹⁵ A rich array of magnetic states or spin states has been probed and tunneling transport through a Mn₁₂ single-electron transistor has been studied using DFT.¹¹⁶ Our model system is a single molecular nano-magnet [Mn₃O(sao)₃(O₂CMe)(H₂O)(py)₃] that contains three Mn^{III} ions, the key for its magnetic properties, three pyridine ligands, one carboxylate group and a water molecule. For simplicity, we abbreviate the molecular formula as [Mn₃]. The SMM can be in an S=6 high-spin (HS) state or in an S=2 low-spin (LS) state depending on the relative spin

orientations of the three Mn^{III} ions. The LS state is observed as the ground state in experiment. The system also can be viewed as a zero-dimensional quantum dot.

5.1 Method and Computational Details

Following the classical definition, we relate potential energy change upon charging and discharging to the capacitance of the system, but with a full quantum description of electrons coupled with molecular configurations. For nano-dots, the capacitance can be obtained by the ratio of the charge variation to the chemical potential variation. The important quantity is the charging energy E_c (sometimes also called capacitive energy), which is the difference between the ionization potential (IP) and the electron affinity (EA),^{117, 118}

$$E_c = \frac{e^2}{c(N)} = IP(N) - EA(N), \quad (5-1)$$

where N is the number of electrons in the system, IP and EA are *the least energy* needed to subtract an electron from, and *the most energy* released to attach an electron to a system of N electrons, respectively. With this important *least-most energy principle* in mind, we carefully examine the physical properties of [Mn₃]. The basic procedure consists of four steps as, 1) optimize the molecular configuration and obtain the electronic structure and magnetic pattern, 2) add and/or subtract an electron of spin-up and/or spin-down followed by optimization again, 3) extract E_c according to *the least-most energy principle*, and 4) calculate magnetic quantum conductance.

As detailed in Chapter 2, we performed DFT²⁸ calculations to investigate the ionization potential and electron affinity of the [Mn₃] SMM system. We used the spin-polarized PBE³¹ exchange-correlation functional in the PAW^{53, 83} as implemented in the VASP package.^{84, 85} The [Mn₃] molecule was placed in a 35 Å by 35 Å by 35 Å unit cell

for isolation from neighboring molecules for both neutral and charged systems. Thus only the Γ -point was used for the first Brillouin zone.¹⁰⁷ The plane-wave energy cutoff was 500 eV. Thresholds for self-consistent calculation and structure optimization were set as 10^{-5} eV and 0.02 eV/ \AA , respectively. The polarizability was calculated by linear interpolation of the induced dipole moment and applied electric field. The dipole moment was calculated with the same criteria as self-consistent calculation with dipole correction.

5.2 Results and Discussion

Configuration optimization is essential to nano-systems that contain $10^2\text{-}10^3$ atoms because of the strong interplay between structure and properties. All calculations should be performed using same theoretical treatment for maximal error cancellations. Figure 5-1 shows the optimized structure of a $[\text{Mn}_3]$ molecule. It can be seen that three pyridine ligands are attached to Mn^{III} ions above the $[\text{Mn}^{III}]_3$ -plane. Below the $[\text{Mn}^{III}]_3$ plane, one carboxylate group is shared by Mn2 and Mn3, while a water molecule is attached to Mn1. The rest of the atoms of the molecule lie almost in the $[\text{Mn}^{III}]_3$ -plane. The largest deviation from the plane is the position of the middle oxygen (O1) atom^{119, 120} (0.39 \AA above the plane, in good agreement with the experimental value of 0.33 \AA), followed by the position of one side oxygen (O2) atom (0.33 \AA below the plane). The deviations of all other atoms range from 0 to 0.20 \AA . Both the HS and LS states show very similar structures after optimization.

There are three distinct low-spin configurations, 1=(down, up, up), 2=(up, down, up) and 3=(up, up, down), but the second and the third ones are equivalent due to the system symmetry. The second LS configuration, or LS2, is predicted to be more stable

than the first LS type by 21 meV. Our calculations also show that LS2 is energetically more stable than HS state by 37 meV, in good agreement with previous calculations.⁶¹

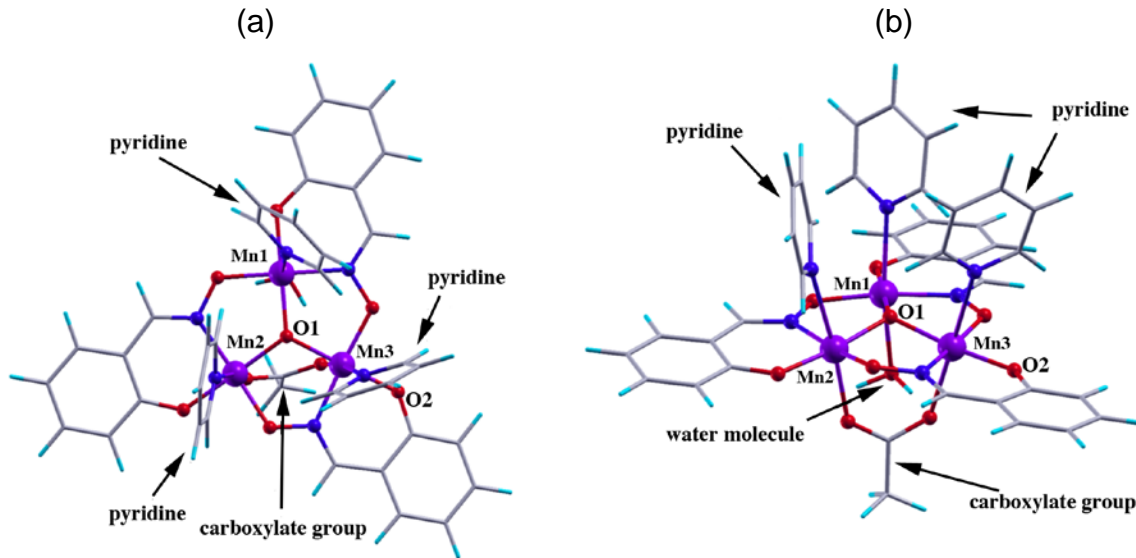


Figure 5-1. Optimized structure of $[Mn_3]$ molecule. Panel (a) is top view and panel (b) is side view. Mn atoms are in purple. O atoms are in red. Blue spheres are N atoms. Grey and blue-green sticks stand for C and H atoms.

Next, in step 2, we proceed to examine energy changes in various initial and final states of $[Mn_3]$ upon adding or removing an electron. We consider only the most stable LS state. Anions (cations) were prepared by adding (removing) a spin-up or a spin-down electron such that we created ions of all possible different spin states. Table 5-1 shows the energies of the neutral molecule, cation, and anion of both HS and LS states. We denote anion_up and anion_down as gaining a spin-up and a spin-down electron, respectively. Similarly, cation_up and cation_down refer to losing a spin-up and spin-down electron, respectively. Structural optimizations were performed for all states. The relaxation energies, defined as the energy difference before and after structural relaxation for a charged system from the neutral structure are 33, 57, 78 and 54 meV for anion_up, anion_down, cation_up and cation_down in the HS state, while those of LS

states are 88, 86, 79 and 73 meV. As shown, the HS state prefers to adsorb a spin-up electron over a spin-down electron by 75 meV, and favors losing a spin-up electron rather than a spin-down one by 592 meV. In contrast to the HS state, the LS state, which is the ground state, prefers to gain a spin-down electron over a spin-up electron by 45 meV. However, it prefers to give away a spin-up electron than a spin-down one by 80 meV.

Table 5-1. Energies of neutral, cation, and anion of both HS and LS states.

Adding/removing one spin up/down electron are all considered. The energy of neutral LS state (ground state) is set to be 0.

	High-spin state		Low-spin state	
	Energy (eV)	Magnetization (μ_B)	Energy (eV)	Magnetization (μ_B)
neutral	0.037	12	0	4
anion_up	-1.627	13	-1.544	5
anion_down	-1.552	11	-1.589	3
cation_up	5.677	11	5.825	3
cation_down	6.269	13	5.905	5

In step 3, we followed *the least-most energy* principle and select the most stable anion and cation states for calculations of ionization potential and electron affinity. Table 5-2 lists the ionization potential (IP), electron affinity (EA), capacitance (C) and charging energy (E_c) of both HS and LS states (Step 4 followed immediately once the right IP and EA were identified). Charging energy and capacitance were calculated according to Equation 5-1. It can been seen that the HS state is 175 meV lower in IP and 75 meV higher in EA than the LS state, resulting in a capacitance of the HS state that is 6% (or 0.247×10^{-20} F) higher than in the LS state and a charging energy that is 260 meV lower than those of the LS state.

Table 5-2. Ionic potential (IP), electron affinity (EA), capacitance (C), and charging energy (E_c) of both HS and LS states.

	High-spin state	Low-spin state	$2(HS - LS)/(HS + LS)$
IP(eV)	5.640	5.825	-3%
EA (eV)	1.664	1.589	4%
C (10^{-20} F)	4.029	3.782	6%
E_c (eV)	3.976	4.236	-6%

The difference in E_c between high-spin and low-spin state constitutes the physical foundation for the concept of quantum magnetocapacitance. Without a magnetic field, the molecule stays in the LS ground state, which has a high charging energy. The system can be switched into the HS state, which has a lower charging energy, by applying a sufficiently high magnetic field, resulting in a change in the quantum capacitance of the molecule or a quantum magnetocapacitance. We estimate the magnitude of the switching magnetic field via $B = \Delta E / g\mu_B \Delta M$, where ΔE is the energy difference between LS and HS states (37 meV), ΔM is the magnetic moment difference between HS and LS states, $\mu_B = 0.058$ meV/T, and the g -factor is equal to 2. With these values, the switching magnetic field is approximately 40 T at 0 K.

It is important to understand the microscopic origin of the charging energy difference between HS and LS states. We thus calculated the spatial distribution of total charge difference between the neutral and the charged $[\text{Mn}_3]$ for both anions and cations in the HS and LS states. Figure 5-2, panels (a) and (b) depict the difference between the neutral molecule and the anion in the HS state, and panel (c) and (d) show those in the LS state. By comparing Figure 5-2 with electron orbitals Figure 5-3, we found that the charge density difference is mainly from the highest occupied electron orbitals (HOMOs). Note that the electron in the HOMO of the neutral molecule is the electron lost in the ionization process and the electron in the HOMO of the anion is the

electron gained when attaching an electron. Panels (a) and (c) (corresponding to HOMOs of the HS and LS neutral atoms, respectively) show significant difference between the HS and the LS cations, especially at the Mn2 site. Drastically different distributions of the lost electron between the HS and the LS states lead to a relatively large difference in *IP* (175 meV). Meanwhile, panels (b) and (d) (correspond to the HOMOs of the HS and the LS anions, respectively) display some similarities, especially on all three Mn atoms, which explains the relatively small difference in *EA* (75 meV). The main difference is that in panel (b), the center oxygen atom has more charge than the one in panel (d).

The mechanism of quantum magnetocapacitance is therefore clear. The charging process in a magnetic system depends on the magnetic state of the system and also on the spin of the incoming and out-going electrons. The capacitance can be controlled by the external magnetic field, by changing the spin configuration of a quantum dot. We stress here that the proposed controllable magnetic quantum capacitance is fundamentally different from tuning the quantum capacitance by utilizing Landau levels¹²¹. There, the system itself is non-magnetic and thus the capacitance is not spin dependent. As the size of a system is reduced, it becomes harder and harder to utilize Landau levels. To generate one magnetic flux quantum through a quantum dot of 2×2 nm² (the size of our molecule) in cross-sectional area, such as the one in our study (in the x-y plane), the required magnetic field is 500 Tesla. The switching field for our model molecule of about 40 T does not allow even one electron in each Landau level, and the capacitance cannot be modulated through Landau levels under such a field.

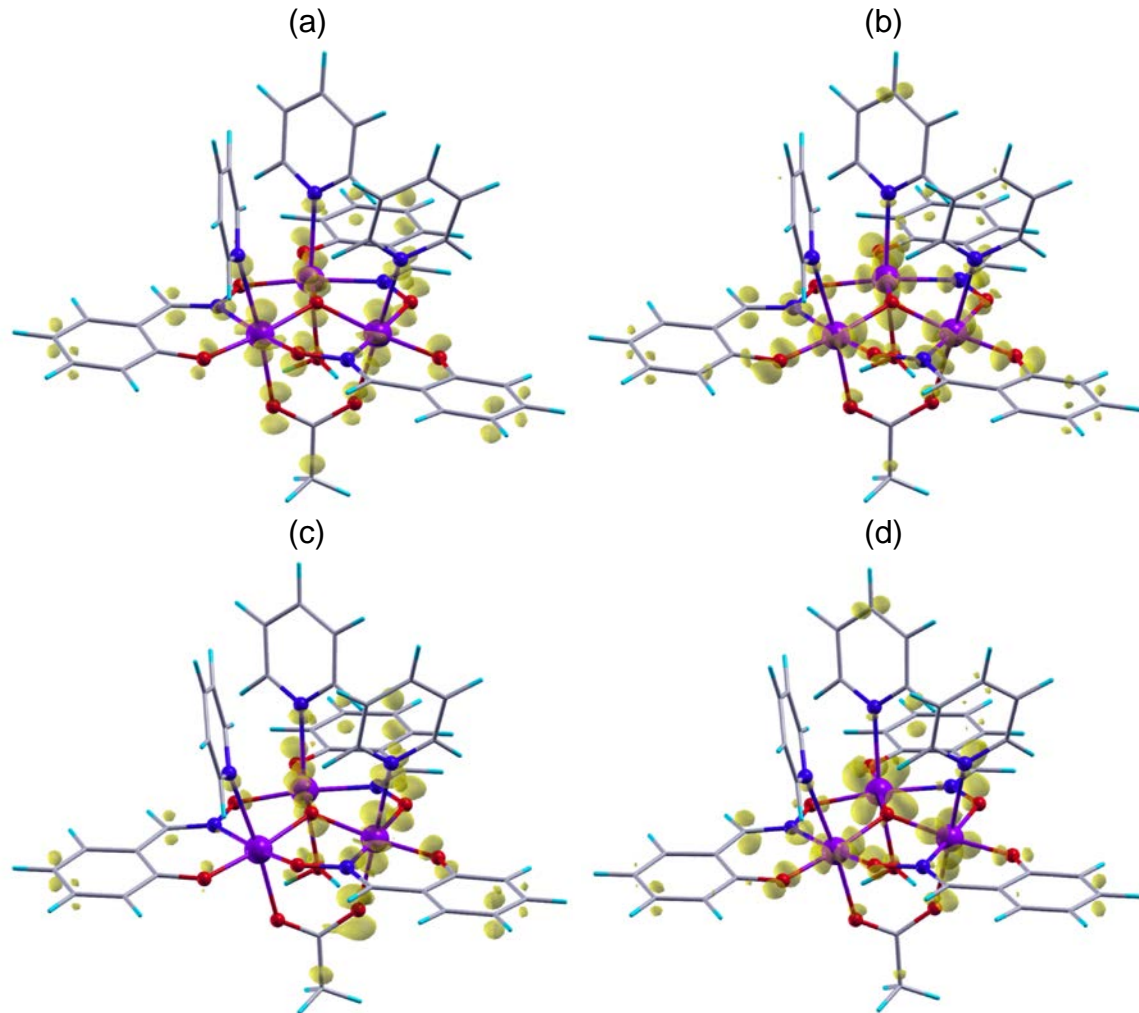


Figure 5-2. Isosurfaces of charge difference of (a) between neutral molecule and cation of high-spin state, (b) between anion and neutral molecule of high-spin state, (c) between neutral molecule and cation of low-spin state and (d) between anion and neutral molecule of low-spin state. Isovalue is $0.015 \text{ e}/\text{\AA}^3$.

The type of molecular magnetocapacitance presented here is best exploited through the Coulomb blockade effect. Recently it has been proposed^{122, 123} that a small spin-dependence of the charging energy of a quantum dot can lead to a giant Coulomb blockade magnetoresistance effect. Molecular magnets and magnetic nanostructures that demonstrate magnetocapacitance are the perfect candidates for realizing this effect.

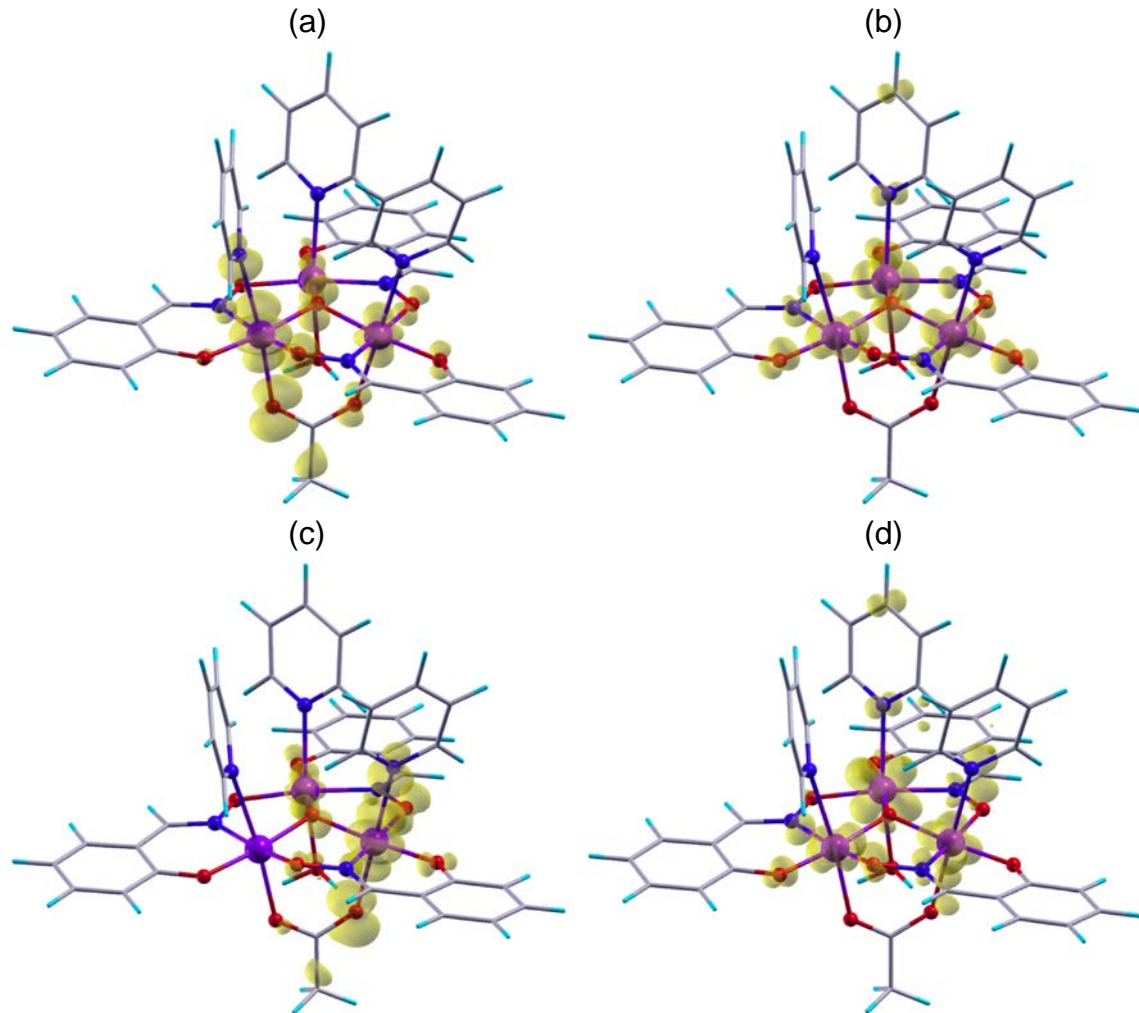


Figure 5-3. Isosurfaces of charge density of (a) high-spin neutral state HOMO, (b) high-spin anion state HOMO, (c) low-spin neutral state HOMO and (d) low-spin anion state HOMO. Isovalue is $0.015 \text{ e}/\text{\AA}^3$.

The concept of the quantum self-capacitance should be distinguished from the polarizability of a molecule, even though both are related to the concept of a capacitance at some level. The polarizability is only a factor affecting the mutual capacitance between the source and the drain if such molecules are used as a dielectric medium. The charging energy, on the other hand, is the essential quantity in the Coulomb blockade effect whereby an electron is injected onto the molecule. The pertinent capacitance in the latter case is the self-capacitance of the molecule (or more precisely the mutual capacitance between the molecule and an electrode). We have

shown that the quantum self-capacitance has a strong spin-dependence. It is natural to further ask whether the molecular polarizability also has a similar spin-dependence. We have performed dielectric constant and polarizability calculations of the molecule in the HS and the LS states within the linear response regime. That is, we assume a linear dependence between the dipole moment and applied electric field. By comparing the calculated response tensor elements, we have found that the maximum difference between the LS and HS states is less than 0.5%. The sharp contrast between the energy calculations and the polarizability (or dielectric constant) calculations highlights the different physics represented by these two quantities. The polarizability reflects how all electrons collectively respond to an external field, whereas the quantum capacitance is mainly determined by only the HOMO and LUMO orbitals. Therefore, a molecule may have different self-capacitances in two spin states but a spin-independent polarizability. It is clear then that when the molecule is used as a dielectric medium its magnetic moment does not affect the polarizability. When it is used as a quantum dot for Coulomb blockade a strong spin-dependence in the current should appear. The capacitances for these two applications are entirely different.

Finally, the proposed magnetic quantum capacitor can be realized by a nano-structure other than SMM. For example, a system that consists of two Fe particles separated by a C₆₀ molecule (Figure 5-4) can have an AFM ground state. Our calculations show that the energy difference between the AFM state and the FM state is a function of Fe_n particle size. Table 5-3 and 5-4 present the energetic and capacitance information of Fe-C₆₀-Fe, corresponding to Table 5-1 and 5-2 for [Mn₃] molecule. The

AFM state is 321 meV lower than the FM state in charging energy, indicating a 6 percent higher capacitance for the AFM state.

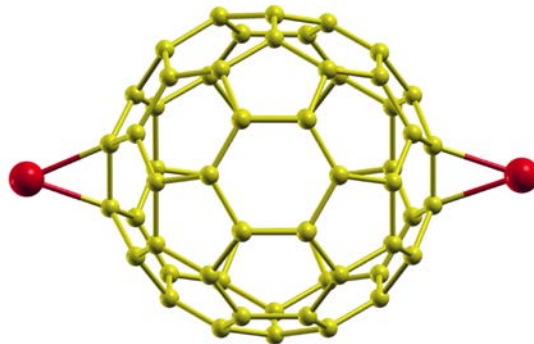


Figure 5-4. C_{60} with 2 Fe atoms attached. C atoms are in yellow and Fe atoms are in red.

Table 5-3. Energies of neutral, cation and anion of both AFM and FM states.

Adding/removing one spin up/down electron are all considered. The energy of neutral AFM state (ground state) is set to be 0.

	AFM	FM		
	Energy (eV)	Magnetization (μ_B)	Energy (eV)	Magnetization (μ_B)
neutral	0.0	-0.269	0.083	6.022
anion	-2.558	1.033	-2.641	6.573
cation	5.402	0.023	5.498	5.300

Table 5-5 lists the energy differences between AFM and FM states, as well as the switching fields, for different values of n. The estimated switching field is 124.4 T for the Fe-C₆₀-Fe system. By enlarging the attached Fe clusters, the magnetic moment difference between AFM and FM states increases and the energy difference decreases. This leads to a drop of the switching field. The switching field of Fe₁₅-C₆₀-Fe₁₅ is estimated as 1.2 T. Beyond a certain size, the ground state of the system transits from the AFM state to the FM state. Our findings on SMMs and Fe_n-C₆₀-Fe_n suggest that a relentless search for candidate systems can be very fruitful. Future synthesis of SMM

guided by the energy principle may hold the key for realizing quantum dots with capacitance that is tunable using a magnetic field under 1 T.

Table 5-4. The ionization potential, electron affinity, charging energy, and capacitance of the Fe-C₆₀-Fe system for both AFM and FM states.

	AFM	FM	$2(FM - AFM)/(FM + AFM)$
IP (eV)	5.402	5.415	1%
EA (eV)	2.558	2.724	13%
C (10^{-20} F)	5.633	5.954	6%
E _c (eV)	2.844	2.691	-6%

Table 5-5. Energies, magnetizations and estimated switch fields (from AFM to FM) of Fe_n-C₆₀-Fe_n systems. The switching field decreases as the number of Fe atoms (or the magnetic moment) increases. Fe₅₀-C₆₀-Fe₅₀ turns out to have a FM ground state.

	AFM		FM		Switching Field (T)
	Energy (eV)	Magnetization (μ_B)	Energy (eV)	Magnetization (μ_B)	
Fe-C ₆₀ -Fe	0.0	-0.27	0.083	6.02	124.4
Fe ₁₀ -C ₆₀ -Fe ₁₀	0.0	0.00	0.022	53.23	3.6
Fe ₁₅ -C ₆₀ -Fe ₁₅	0.0	0.00	0.012	86.73	1.2
Fe ₅₀ -C ₆₀ -Fe ₅₀	0.014	0.91	0.0	281.34	N/A

5.3 Summary and Conclusion

In this chapter, we have demonstrated the concept of molecular magnetocapacitance. The quantum part of the capacitance becomes spin-dependent, and is tunable by an external magnetic field. Such molecular magnetocapacitance can be realized using single molecule nano-magnets and/or other nano-structures that have antiferromagnetic ground states. As a proof of principle, first-principles calculation of the nano-magnet [Mn₃O(sao)₃(O₂CMe)(H₂O)(py)₃] shows that the charging energy of the high-spin state is 260 meV lower than that of the low-spin state, yielding a 6% difference in capacitance. A magnetic field of ~40T can switch the spin state, thus changing the molecular capacitance. A smaller switching field may be achieved using nanostructures

with a larger moment. Molecular magnetocapacitance could lead to revolutionary device designs, e.g., by exploiting the Coulomb blockade magnetoresistance whereby a small change in capacitance can lead to a huge change in resistance.

CHAPTER 6

FIRST-PRINCIPLES STUDIES OF C₆₀ MONOLAYERS ON METAL SURFACES

6.1 Fe-doped monolayer C₆₀ on *h*-BN/Ni(111) Surface²

Following intensive research activities in the 1990s,¹²⁵⁻¹³⁵ investigations of physical properties of C₆₀ assemblies on surfaces continue as an active research area.¹³⁶⁻¹⁴⁴ Scientists aim to understand fundamental physical processes in these complex systems that may have applications in nano-molecular electronic materials, for example, electrical or optical sensors¹⁴⁵ and photovoltaic devices.¹⁴² Like carbon nanotubes, the electronic structure of C₆₀ and C₆₀ assemblies can be tuned via contact with metals or organic molecules. The best-known examples are perhaps the superconductivity of alkali-metal-doped C₆₀ solids^{146, 147} and soft ferromagnetism in C₆₀-nonpolymeric organic molecule complexes.¹⁴⁸ With high electron affinity, C₆₀ is often an electron receptor, which alters the electronic properties of the adherent molecule and molecular assemblies. Employing this characteristic, recent study of quantum transport¹³⁶ shows that one can alter the I-V characteristics of metal-doped fullerene thin film deposited on gold substrate by controlling the thickness of potassium doped C₆₀ thin films, eight years after the first report of a single C₆₀ molecule transistor.

In the above-cited experimental investigations, various surfaces have been used as support. Our previous theoretical effort focused on surface-supported monolayer C₆₀ without doping.¹⁴⁹⁻¹⁵¹ We investigated and characterized thoroughly the interface electronic structure of these systems before and after adsorption of the C₆₀ monolayer assemblies, and provided insights to experimental observations of C₆₀ on Au(111), Ag(111), Cu(111),^{149, 150} and *h*-BN/Ni(111).¹⁵¹ More recently, Hebard's group¹⁵²

² This work has been published in Journal of Chemical Physics.¹²⁴

investigated Fe-doped (by vapor deposition) C₆₀ monolayers on silica. In-plane transport properties of the Fe thin film were investigated and a universal, scale-dependent weak-localization correction to the anomalous Hall effect was observed. Compared to metal surfaces, insulator surfaces allow studies of dopant effects without interference from relatively strong metal surface fullerene interactions. However, Hebard's experiments do not further understanding of the system in the ultra-thin Fe-film limit, since the transport measurements were conducted in the Boltzmann regime. First-principles calculations such as we have performed can provide observations and understanding complementary to the experiments. In general, metal doping in C₆₀ thin films can be prepared by evaporation-deposition procedure, and C₆₀ can be the under-layer (exohedral doping),^{129, 131, 153} or an over-layer, or sandwiched between two layers of metal according to the order of deposition.^{125, 129, 133, 134} The electronic properties and the metal-C₆₀ interaction are found to depend strongly on the concentration of dopants and the type of metal.

This chapter reports our study of the structure, electronic and magnetic structure of iron-doped the C₆₀-*h*-BN/Ni(111) systems. We focus on the trend of charge transfer as a function of Fe concentration. We choose *h*-BN/Ni(111) systems as a way to reduce complexity compared with amorphous silica. With current techniques the *h*-BN/Ni(111) system can be prepared experimentally. In fact, the *h*-BN monolayer is commensurate with the Ni(111) surface and the system has been studied by several experimental groups.¹⁵⁴⁻¹⁵⁶ It was found that the *h*-BN physisorbs on the metal surfaces and the electronic structure of the *h*-BN monolayer is independent of the metal substrate. Later, this surface was also prepared in experiments to study C₆₀ monolayer-motion-induced

charging and electron-phonon coupling.¹⁴³ The separation of electronic structure and the inert nature of the *h*-BN provide an insulating layer that separates the C₆₀ molecules from the metal surface. As a result, the fullerene layer has a relatively weaker interaction¹⁵¹ with the surface compared to noble metal surfaces.¹⁵⁷ This feature is very useful for preparing quasi-2D electronic systems. Our previous calculations agree very well with experiments with and without C₆₀ adsorption.¹⁵⁷

Before moving to the next section, a brief summary of previous work on the metal-C₆₀ interaction is necessary. In processes of tailoring electronic structure, charge transfer at metal-C₆₀ interface has been a focus of many investigations. Numerous studies, both experiment and theory, have investigated the charging of the lowest unoccupied states of C₆₀ molecules in gas phase,¹⁵⁸⁻¹⁶⁰ solids,^{146, 147, 161} and thin films^{126, 129, 132, 134, 138, 162} (including monolayers). In some experiments, metal atoms are deposited over C₆₀ monolayers or thin films,^{129, 133, 135, 162} akin to systems we have used in this chapter. It is well-established that C₆₀ charge transfer from metallic surface to the molecules is about 1 electron or less in systems for a C₆₀ monolayer deposited on the surface. The situation is different when metal atoms are doped into a C₆₀ thin film or solid, in which case more than one electron can transfer to a fullerene molecule. Nevertheless, theoretical studies of C₆₀-transition metal and non-alkali metal system are mainly done for gas phase, that is, a single molecule complex.

6.1.1 Method and Computational Details

As in previous chapters, we used the VASP package and PAW methodology. Two types of exchange-correlation approximation were used to calculate the exchange and correlation potentials: the spin-dependent PW91 GGA⁴¹ and the local spin density approximation (LSDA) as parameterized by Perdew and Zunger.²⁹ In some cases,

GGA+U and LSDA+U calculations were performed to check possible gap opening at the Fermi surface. For the DFT+U calculations, we used the rotationally invariant approach by Liechtenstein *et al.*,³⁴ with the effective on-site Coulomb value (U) of 4.5eV and the effective on-site exchange (J) value of 0.89eV for Fe atoms as proposed by Cao *et al.*¹⁶³

We utilized convergence tests performed in our previous work on a C_{60} monolayer supported by h -BN/Ni (111)¹⁵¹. In geometry optimization, surface Brillouin-zone integrations were performed on a k mesh of $2 \times 2 \times 1$ for h -BN/Ni(111) (4×4) substrate upon C_{60} adsorption. An $8 \times 8 \times 1$ k -mesh was chosen for calculating the density of states of Fe_n -doped C_{60}/h -BN/Ni (111). The energy cutoff was 500 eV. A Gaussian smearing of 0.1eV was used for the Fermi surface broadening. Finally, the force convergence was 0.01eV/ \AA and energy convergence was 10 meV/unit cell.

The equilibrium lattice constant¹⁵¹ is 2.50 \AA and 3.52 \AA for h -BN and bulk Ni. The system has a layered configuration, which contains a Fe_n -doped C_{60} monolayer, a h -BN monolayer, and a seven-layer Ni (111) slab. For the most stable adsorption sites of a C_{60} monolayer on h -BN/Ni (111), the distance between the bottom hexagon of C_{60} and the h -BN surface is 3.6 \AA . Furthermore, the wall-wall distance between two C_{60} molecules is 3.2 \AA while their center-center distance is 9.9 \AA . The thickness of vacuum between two slabs is ~15 \AA . In order to search for the stable structure of Fe_n -doped C_{60} monolayer on h -BN/Ni (111), all the atoms were allowed to relax except for the two bottom layers of Ni, which were fixed at the ideal bulk geometry.

In the equilibrium state, the Fe- C_{60} binding energy is a crucial indicator to determine the effect of Fe. It is computed as

$$E_b = (E_{total,doped} - E_{total,undoped} - nE_{Fe})/n, \quad (6-1)$$

where the first two terms refer to the total energies of C_{60} adsorbed on h -BN/Ni(111) with and without Fe doping, respectively, n specifies the number of dopant Fe atoms, and E_{Fe} is the energy of an individual Fe atom with spin-polarization corrections.

The spin-dependent density of states (DOS) and spin-dependent projected density of states (PDOS) are crucial quantities for estimating charge transfer and magnetic moments. In VASP, the PDOS is obtained via projecting the DOS in spheres of Wigner radii centered at nuclei. The total DOS is the sum of the spin-up and spin-down DOS, and the density of spin states (DOSS) is the DOS difference between spin-up and spin-down DOS. The projected density of spin states (PDOSS) is the DOSS projected on subsystems in the same way as for the PDOS.

Electronic charge transfer at the Fe- C_{60} interface is also an important quantity in this chapter. To estimate charge transfer, we have integrated the PDOS of each subsystem from the bottom of the valence band to the Fermi level, and thus obtained the total charge of the subsystem. For example, the charge transferred to C_{60} is calculated by subtracting the total charge of a C_{60} molecule for a pure C_{60} monolayer from the total charge projected on the C_{60} monolayer in the Fe- C_{60}/h -BN/Ni(111) complex. All integrations are scaled such that the sum of electrons is the total number of electrons of the system. We have also used the Bader analysis¹⁶⁴ to compute the charge transfer. The two methods give slightly different results, but the trend are the same. The Bader analysis is advantageous because it provides a unique definition of charge on each atom and it is easy to compute. However, the PDOS analysis offers information of orbital-specific information. We therefore present both results in this chapter.

The charge difference before and after doping is calculated as

$$\Delta\rho(\vec{r}) = \rho_{total}(\vec{r}) - \rho_{C_{60}-hBN/Ni(111)}(\vec{r}) - \sum_{i=1}^n \rho_{Fe_i}(\vec{r}), \quad (6-2)$$

and spin density is the density difference between spin-up and spin-down electrons.

Finally, the magnetic moment is computed from the population difference between spin-up and spin-down electrons. The magnetic moments projected on subsystems are the integrated PDOSs from the bottom of the valence band to the Fermi level.

6.1.2 Results and Discussions

6.1.2.1 Structure

This section presents the ground state and some isomeric geometric structures of Fe_n-doped C₆₀ monolayer supported by *h*-BN/Ni(111). The *h*-BN/Ni(111) surface is a composite surface in which the Ni(111) surface is covered by monolayer hexagonal boron nitride (*h*-BN). The concentration of Fe doping (*n*/C₆₀) is 1-4 and 15 atoms. For *n*=1-4, we exhausted initial configurations in which the Fe atoms sit at different interstitial sites of C₆₀. For *n*=15, two initial configurations were tested. The procedure for geometry optimizations is described in the foregoing section. Here we report structures and energies of the most stable configurations found in our search. Figure 6-1 to 6-5 depict the lowest energy Fe_n-C₆₀ structures supported by *h*-BN/Ni(111). Binding energies of various configurations and systems are given in Table 6-1.

Figure. 6-1 a shows the most stable structure of an Fe₁-doped C₆₀ monolayer on the surface. The Fe atom is located in the center of the interstitial space of the fcc C₆₀ molecular lattice, and forms two bonds to each adjacent C₆₀ molecule. The bond lengths between the Fe atom and its nearest C atoms are 2.22 Å and 2.29 Å, respectively. The three C-Fe-C angles shown in Figure 6-1a are about 38°. The distance between the Fe

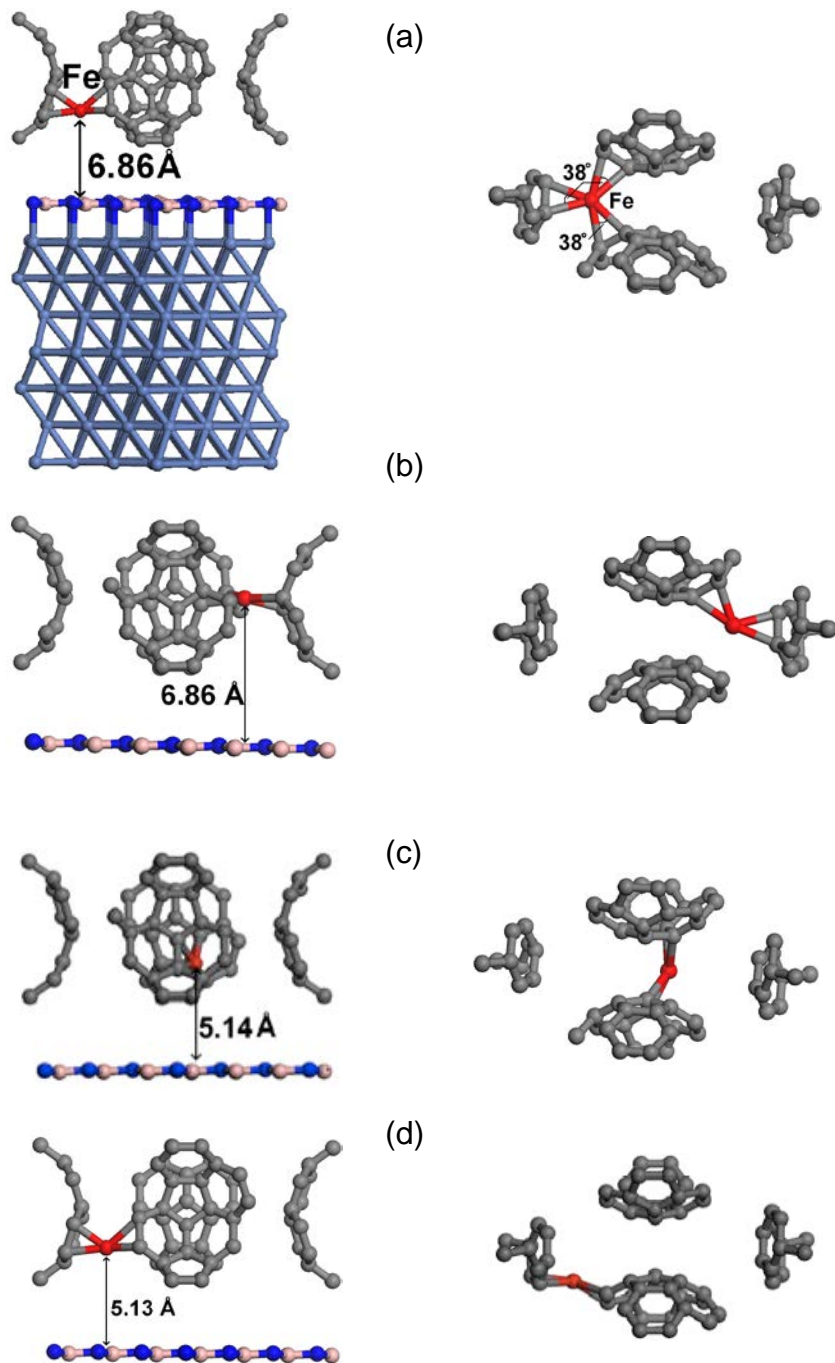


Figure 6-1. Fe₁-doped C₆₀ monolayer configurations on an *h*-BN/Ni (111) surface. Panel (a)-(d): Structure of the configurations according to binding energy. (a) is the most stable and (d) the least. Left column is side view and right is top view. The red, grey, dark blue, pink and indigo balls represent iron, carbon, nitrogen, boron and nickel atoms, respectively. Note only parts of C₆₀

molecules in 4 unit cells are not shown for a clear view. View of whole molecules is presented in Figure 6-6 to 6-8.

atom and the *h*-BN surface is 6.86 Å. The binding energy of 3.04eV/Fe atom is a result of the strong Fe-C bonding. The other possible sites are shown in Figure 6-1 (b)-(d), listed from high to low binding energies.

For *n*=2, the two Fe atoms energetically prefer to stay apart in the interstitial space of the C₆₀ molecules. As shown in Figure 6-2 (a), Fe1 binds to three neighboring C₆₀ molecules with the lengths ranging from 2.25 Å to 2.27 Å, nearly equal. This Fe atom locates in the middle of the interstitial site. The three C-Fe-C angles shown in Figure 6-2 (a), are all 38°. Even though the Fe1 atom is a neighbor of three C₆₀ molecules, Fe2 positions itself off the middle of the interstitial site. This Fe atom only binds to two C₆₀ molecules. The two nearest bond lengths are 2.16 Å and 2.23 Å, respectively. The two C-Fe-C angles are 39°. On this off-middle site the Fe atom is too far away to form bonds with the third C₆₀ molecule, where the shortest Fe-C distance is 2.40 Å. The distance between the Fe (1 or 2) and *h*-BN is 6.85 Å. The relaxed Fe₂C₆₀ structure is similar to FeC₆₀, except for one more Fe atom adding on another separate interstitial site. The distance between the two Fe atoms is 5.81 Å. The binding energy in Fe₂C₆₀ is 3.11 eV/Fe, only 0.07 eV higher than that in FeC₆₀, implying a small Fe-Fe interaction mediated by a C₆₀ molecule. Other doping sites are depicted in Figure 6-2 (b)-(d).

Table 6-1. Binding energy of Fe atoms at various sites in eV.

	FeC ₆₀	Fe ₂ C ₆₀	Fe ₃ C ₆₀	Fe ₄ C ₆₀	Fe ₁₅ C ₆₀
a	3.04	3.11	3.12	3.23	3.41
b	2.95	2.85	2.87	3.18	3.21
c	2.02	2.30	2.71	3.05	
d	1.99	2.18			

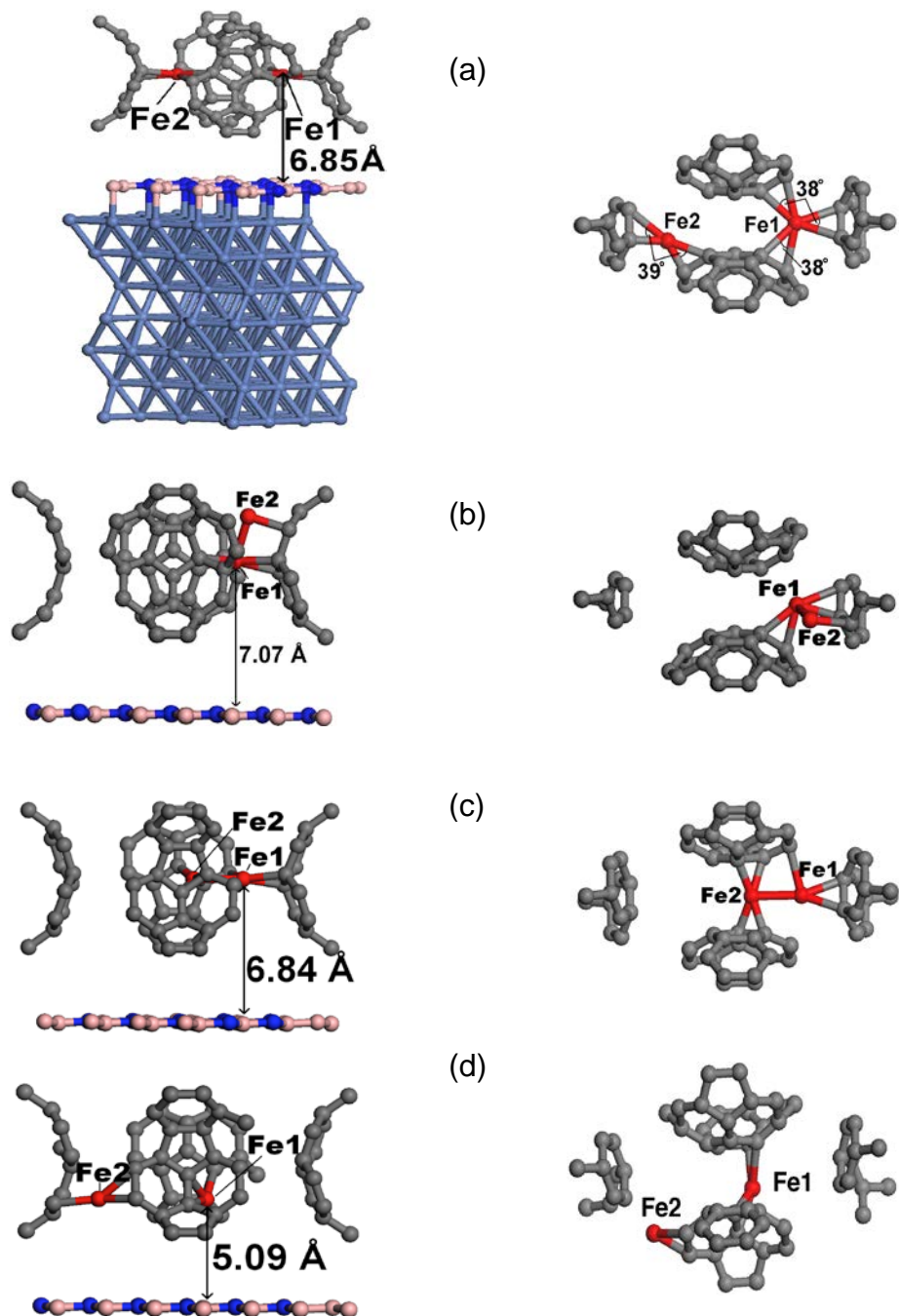


Figure 6-2. Same as Figure 6-1 for Fe₂-doped C₆₀ monolayer on an *h*-BN/Ni (111) surface.

Next, a third Fe atom was added into the optimized structure of Fe₂C₆₀ followed by further structural relaxation. Figure 6-3 (a) shows the most stable structure of Fe₃C₆₀.

The additional Fe atom locates further away from the BN layer compared to the other two Fe. It binds to two nearest C₆₀ molecules via 4 Fe-C bonds and to the adjacent Fe atom. The lengths of the Fe-C bonds are 1.97 Å – 2.19 Å. The two C-Fe3-C angles are 41° and 42°, respectively and the length of the Fe1-Fe3 bond is 2.28 Å. For Fe1, the Fe1-C bond lengths range from 2.07 Å to 2.23 Å, which are shorter than those in the Fe₂C₆₀ complex. The two C-Fe1-C angles are 38° and 39°, respectively. On the other side, the Fe2 atom binds to three C₆₀ molecules, two bonds each to two C₆₀ and one bond to the remaining one. The bond lengths are 2.06 Å – 2.33 Å. The two C-Fe2-C angles are both 39° (Figure 3a). The distance between Fe1 and the *h*-BN surface is the same as in FeC₆₀ and 0.01 Å more than in Fe₂C₆₀ (Figure 6-1 (a) and 6-2 (a)). The binding energy in Fe₃C₆₀ is 3.12eV/Fe atom, contributed by the Fe-C and Fe-Fe bonds, very close to the value of Fe₂C₆₀. The other two configurations are shown in Figure 6-3 (b)-(c).

The Fe₄C₆₀ system is the largest one for which an extensive energy minimum search was performed. Figure 6-4a shows the most stable structure for Fe₄C₆₀ supported by *h*-BN/Ni (111). It is notable that three iron atoms, Fe1, Fe3 and Fe4, form a trimer with the Fe-Fe bond lengths ranging from 2.40 Å to 2.89 Å. The one atom (Fe2) is separated from the cluster by the C₆₀, the same as in previous cases. All Fe atoms form Fe-C bonds, with bond length ranging from 1.95 Å to 2.32 Å, to adjacent C₆₀ molecules. The distance between Fe1 at the lowest position and *h*-BN is 7.03 Å, a substantial increase from the 1-3 Fe-doped systems. The binding energy in Fe₄C₆₀ is higher than that in FeC₆₀ by 0.19eV/Fe atom and Fe₂C₆₀ by 0.12eV/Fe atom, suggesting

that the Fe_3 cluster has high stability in the interstitial spaces of C_{60} monolayer. Again, the other two structures are shown in Figure 6-4 b and c.

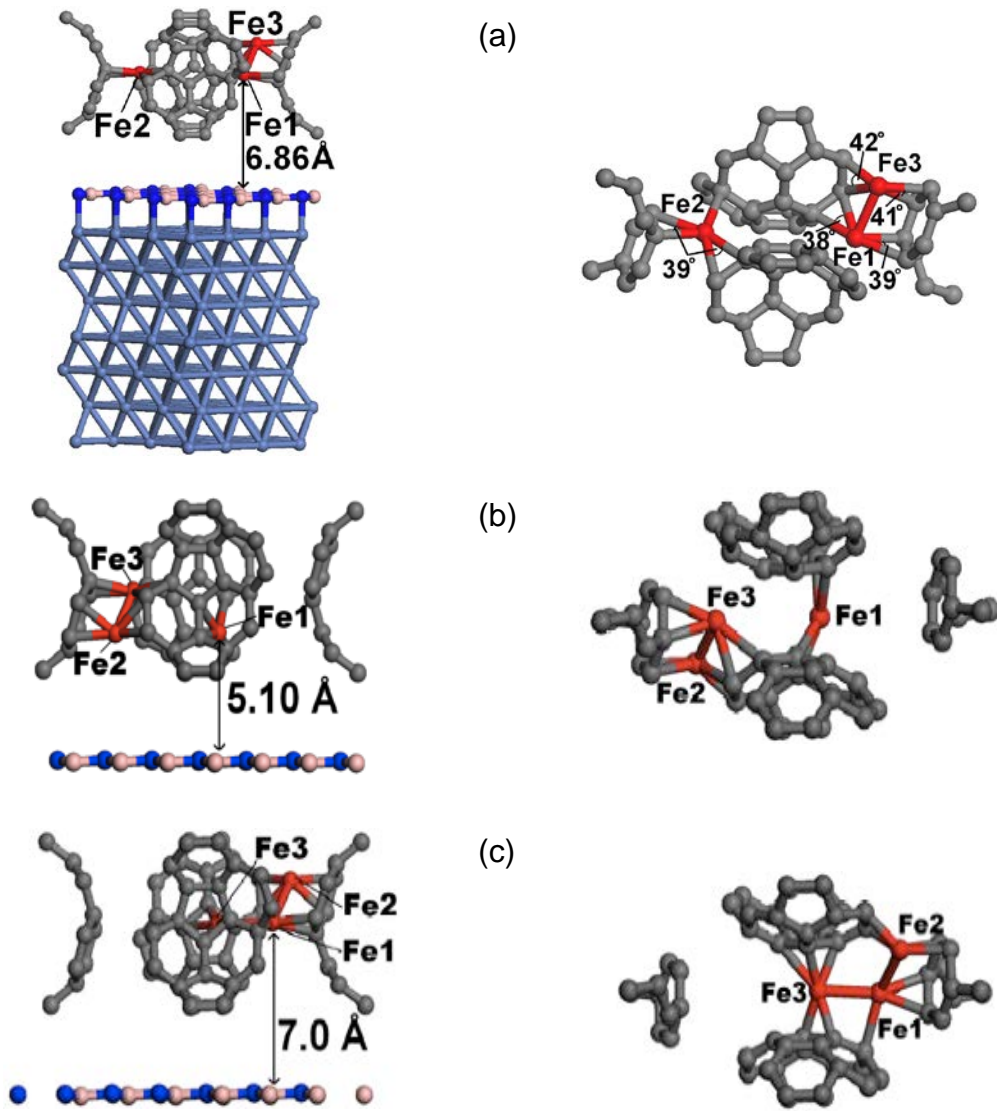


Figure 6-3. Fe_3 -doped C_{60} monolayer on an $h\text{-BN}/\text{Ni}(111)$ surface. Similar to Figure 6-1 with (a) being the most stable on and (c) the least.

Finally, we investigated the behavior of a heavily doped $\text{Fe}_n\text{C}_{60}\text{-}h\text{-BN}/\text{Ni}(111)$, with $n=15$. Starting with the optimized structure of Fe_4 -doped system, 11 Fe atoms were added randomly over the C_{60} monolayer. We repeated the process twice with different

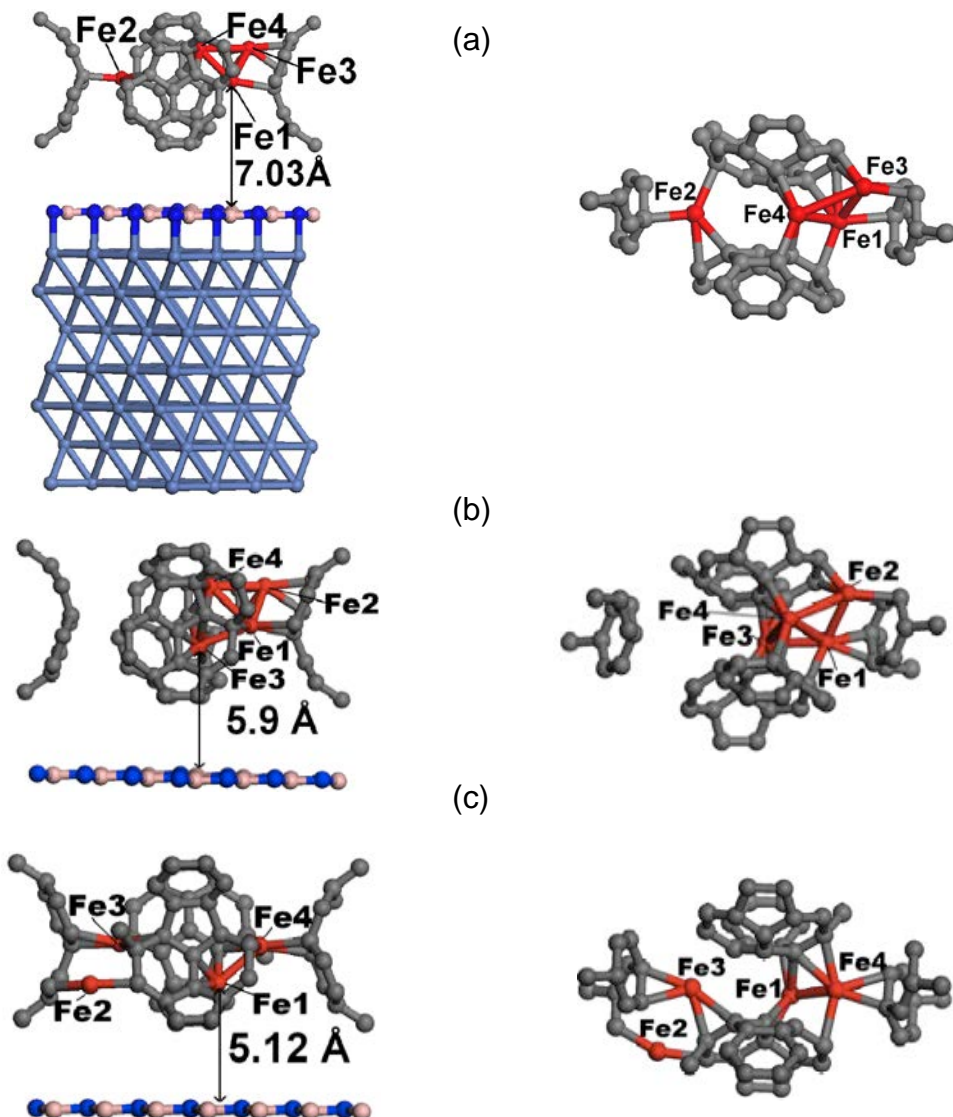


Figure 6-4. Same as Figure 6-3 for Fe_4 -doped C_{60} monolayer on an $h\text{-BN}/\text{Ni}(111)$ surface.

initial configurations of the 11 ad-atoms. The configuration with the lower energy is presented here. Note that this configuration may not be the most energetically stable state. However, our interest is in the morphology of the $\text{Fe}_{15}\text{C}_{60}$ complex and its impact on electronic and magnetic properties. Figure 6-5b shows the positions of the first 4 Fe atoms in interstitial sites, and the extra 11 Fe atoms distributed over the C_{60} monolayer. All of the Fe atoms form bonds with at least one other Fe atom, except for one (Fe2). Out of the 15 Fe atoms, seven form bonds to the neighboring C_{60} molecules. The

distance between Fe1 and *h*-BN is 7.23 Å, 0.2 Å higher than that in the Fe₄C₆₀ complex. Other low-lying atoms, Fe1, Fe3 and Fe4, are shifted slightly away from the BN layer due to Fe-Fe interaction. The binding energy in Fe₁₅C₆₀ is 3.41eV/Fe atom, higher than that in Fe₄C₆₀ by 0.18eV/Fe atom. The second structure with a little less binding energy is shown in Figure 6-5b.

6.1.2.2 Electronic and Magnetic Properties

The bonding of Fe to C₆₀, in Fe_n-C₆₀/*h*-BN/Ni(111) complexes (*n*=1-4, 15) may involve two possible types of interaction: (i) ionic bonding, with the characteristic feature being charge transfer from the metal towards C₆₀ and (ii) covalent bonding, characterized by hybridization between metal *s* and *d* states and C₆₀ orbitals. Following structural relaxation, we have calculated the spin-dependent DOS and PDOS, and analyzed charge transfer, spin distribution, and spin populations projected on the individual orbitals. All the electronic calculations shown below were performed with both spin-dependent GGA and LDA. For *n*=4 and 15, we used GGA+U and LDA+U to examine possible the gap at the Fermi level. Changes in charge transfer and magnetic moments as obtained from GGA+U (LDA+U) are compared with those from GGA (LDA).

Upon obtaining the structure of various systems, we have performed Bader analysis to study the charge rearrangement. Table 6-2 provides information about the charge change in subsystems as a function of the number of Fe atoms and doping sites. It is clear that charge transfer to C₆₀ increases monotonically as the number of Fe atoms increases, ranging from about 1e⁻ to 5e⁻. One also concludes that Fe atoms and the Ni(111) substrate always lose electrons, while C₆₀ and the monolayer *h*-BN always gains electrons. In addition, the magnetic moment of C₆₀ is always in the direction

opposite to the total moment of the systems. In the following sections, we discuss a detailed analysis based on an integration of PDOS, which is different from the Bader method, and focus on the most stable structures.

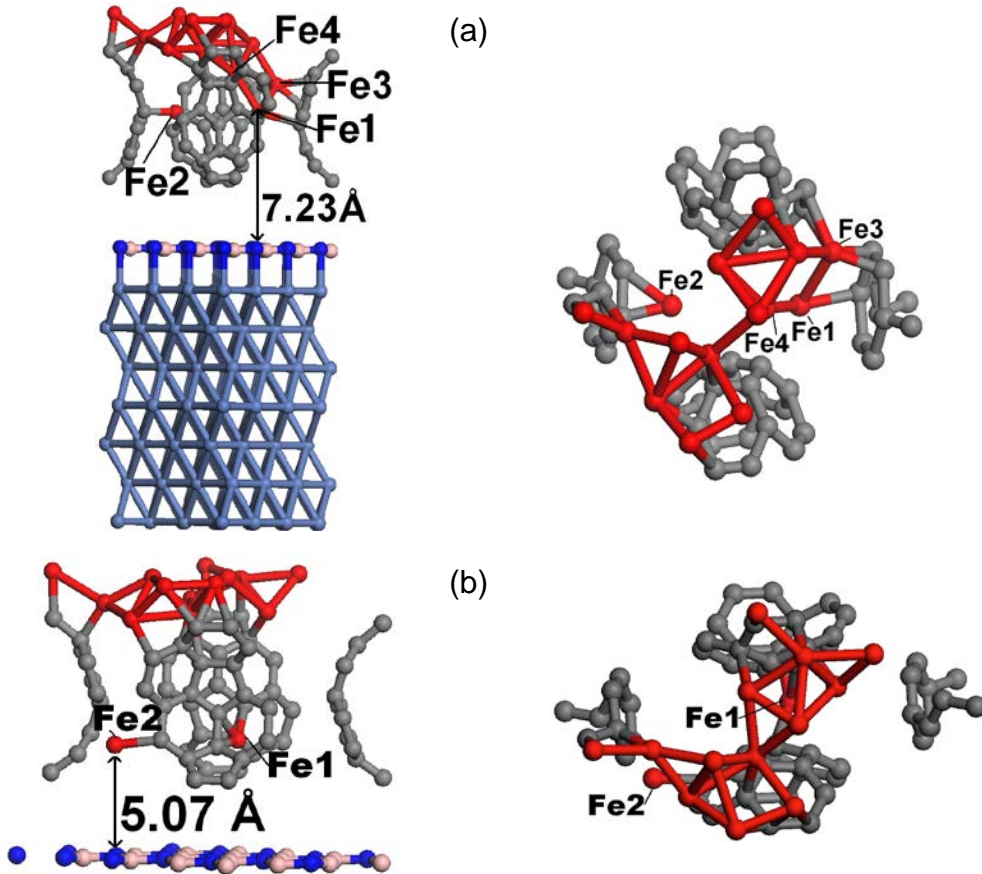


Figure 6-5. Two isomers of a Fe_{15} -doped C_{60} monolayer on an $h\text{-BN}/\text{Ni}$ (111) surface. Panel (a) is more stable than panel (b).

6.1.2.2.1. FeC_{60}

We performed the DOS calculations on the optimized FeC_{60} configuration. Figure 6-6a shows the site-projected DOS of C_{60} and the Fe atom. The energy for PDOS ranges from -5eV to 2eV and the Fermi level is shifted to zero in each case. In the GGA calculations, four main features are observed in the spectrum for C_{60} : peaks at -2.58eV (HOMO-1), -1.43eV (HOMO), 0.29eV (LUMO) and 1.33eV (LUMO + 1). The LUMO

peaks remain above the Fermi level. The LUMO level is partially filled. This partial filling of the LUMO level is a consequence of charge transfer from the metal to the molecule. Integrating the PDOS of doped C₆₀ up to the Fermi energy, the estimated charge transferred toward C₆₀ is 0.95 electrons/C₆₀ molecule, slightly lower than the number given by the Bader method (see Table 6-2). Compared to a C₆₀ monolayer on a metal surface without dopants, the charge transfer from the Fe atom to C₆₀ per C-Fe contact^{150, 157} is much more significant. This large value is a result of the difference in the electron affinity between the Fe and C₆₀.^{127, 129} Thus, ionic character contributes to the Fe-C₆₀ bonding. Close examination of the C₆₀ HOMO state in the PDOS also shows that the electron density is shared by the C₆₀ HOMO and the Fe s and *d* orbitals. A small amount of hybridization also occurs at the C₆₀ HOMO-1 band (see Figure 6-6 a). This level mixing signals the covalent nature of the Fe-C₆₀ bonding.

The spin-density of states of the C₆₀-Fe system is obtained by taking the difference of DOS and PDOS of the spin-up and spin-down electrons. As seen in Figure 6-6 b, the spin-up electron, by convention, is the majority spin of Fe and also of the system, but more electrons with the minority spin (spin down) occupy the bands near the Fermi level. Consequently, the spin-down electrons are preferentially transferred from Fe towards C₆₀. The projected density of spin states (PDOSS) of C₆₀ indeed shows that the spin-down electrons dominate the bands of C₆₀ near the Fermi level. Integrating the PDOSS distributions on C₆₀ and Fe, respectively, we list the spin populations for the individual orbitals in Table 6-3. These numbers indicate an intra-atomic charge transfer from 4s to 4p and 3d within the Fe atom. Note that the spin projected onto the C₆₀ is

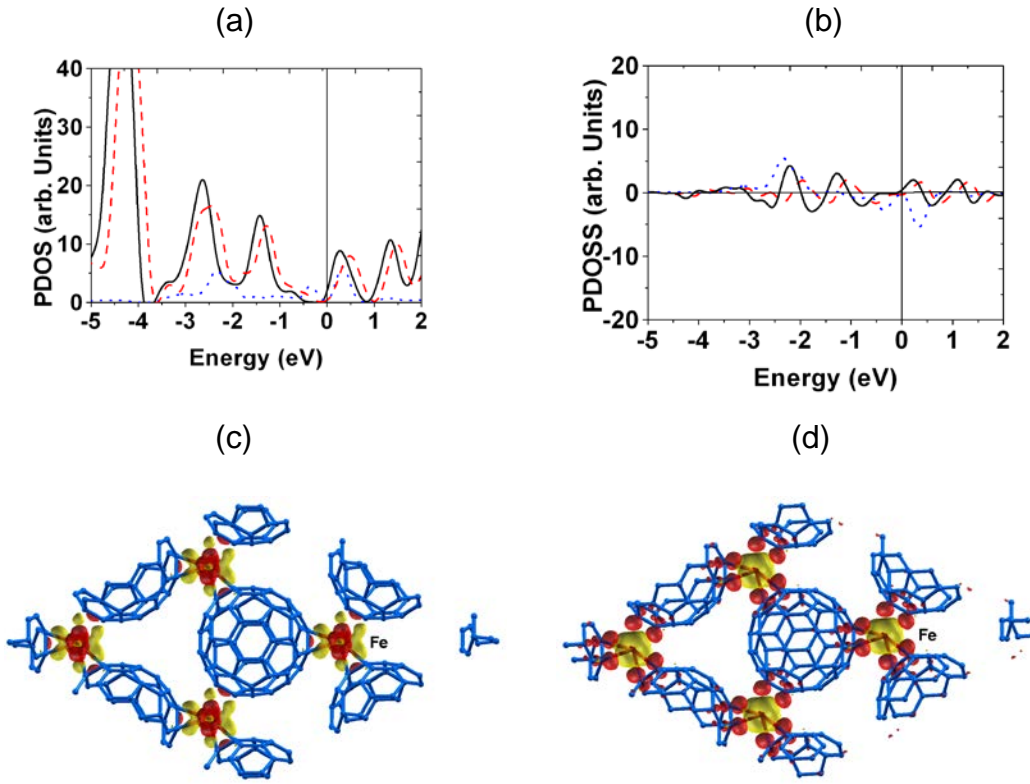


Figure 6-6. Projected densities of states (PDOS) panel and projected densities of spin states (PDOSS) on monolayer C₆₀ and a Fe atom for FeC₆₀/h-BN/Ni(111): (a) PDOS of C₆₀ in GGA (black solid) and LDA (red dash), and PDOS of Fe in GGA (blue dot), Fermi level is at energy of 0; (b) PDOSS of C₆₀ in GGA (black solid) and LDA (red dash), and PDOSS of Fe in GGA (blue dot). Panel (c) and (d) are iso-surfaces of charge density difference and spin density, with yellow representing charge accumulation in (c) and positive spin in (d), and red charge depletion and negative spin.

down, opposite to the majority spin that is dominated by the Fe 3d electrons. Also note that a pure C₆₀ has the same populations of spin-up and spin-down and thus zero net spin. The negative magnetic moment on C₆₀ (-0.37 (μ_B)) that aligns anti-parallel to that of the Fe atom is a direct consequence of Fermi level alignment and charge transfer. The contribution to charge transfer from the spin minority exceeds that from the spin majority by roughly 40%. The total spin projected on the Fe is 2.45 and 1.96 μ_B using

GGA and LDA, respectively. Further analysis of orbitals indicates that spin density transfer is from Fe 3d to C 2p orbitals (Table 6-3). In a study of Fe-doped single C₆₀

Table 6-2: Charge transfer and magnetic moments as computed by the Bader method

	Fe _n C ₆₀ /h-BN/Ni	ΔQ_{Fe}	ΔQ_{C60}	$\Delta Q_{h\text{-}BN}$	$\Delta Q_{Ni(111)}$	$m_{Fe}(\mu_B)$	$m_{C60}(\mu_B)$
n=1	Config. a						
	GGA	-0.87	+1.04	+1.29	-1.46	+2.47	-0.38
	LDA	-0.84	+1.00	+1.22	-1.38	+2.20	-0.39
	Config. b						
	GGA	-0.89	+1.08	+1.16	-1.35	+2.23	-0.51
	Config. c						
	GGA	-0.95	+1.12	+1.27	-1.44	+2.45	-0.33
	Config. d						
n=2	GGA	-0.95	+1.12	+1.28	-1.46	+2.47	-0.32
	Config. a						
	GGA	-1.70	+1.87	+1.30	-1.47	+4.73	-0.74
	LDA	-1.66	+1.84	+1.21	-1.38	+4.54	-0.70
	Config. b						
	GGA	-1.38	+1.57	+1.27	-1.45	+4.56	-0.40
	Config. c						
	GGA	-1.65	+1.87	+1.26	+1.48	+4.13	-0.42
n=3	Config. d						
	GGA	-1.90	+2.07	+0.73	-0.90	+5.04	-0.07
	Config. a						
	GGA	-2.46	+2.66	+1.27	-1.47	+7.00	-0.73
	LDA	-2.32	+2.50	+1.19	-1.37	+6.56	-0.62
	Config. b						
	GGA	-2.50	+2.66	+1.28	-1.44	+7.11	-0.54
	Configuration c						
n=4	GGA	-2.46	+2.67	+1.25	-1.46	+6.34	-0.40
	Config. a						
	GGA	-3.10	+3.29	+1.27	-1.46	+9.49	-0.57
	LDA	-2.92	+3.10	+1.19	-1.37	+9.14	-0.49
	Config. b						
	GGA	-3.02	+3.23	+1.25	-1.46	+8.62	-0.62
	Config. c						
	GGA	-3.28	+3.45	+1.23	-1.40	+9.16	-1.03
n=15	Config. a						
	GGA	-5.09	+5.24	+1.24	-1.39	+29.93	-0.69
	LDA	-4.76	+4.89	+1.19	-1.32	+25.39	-0.30
	Config. b						
	GGA	-4.55	+4.69	+1.24	-1.37	+40.34	-0.16

where the Fe atom is inside the C₆₀, Tang *et al.*¹⁶⁵ found that the magnetic moment of the Fe atom is 2.19 μ_B and the spin projected on the C₆₀ is -0.19 (μ_B), opposite to that projected on the Fe atom. In our investigations, the Fe atom is incorporated at the interstitial site of the C₆₀ molecules (exohedral doping). Evidently, the negative sign of spin of the molecule is independent of the doping site of the Fe atom. The charge density difference as computed via Equation 6-2 is depicted in Figure 6-6 c, where the iso-surface value is 0.04e/ \AA^3 . Interestingly, the charge transfer to C₆₀ mainly stays at the interface between the Fe atom and the molecule, similar to the monolayer C₆₀ on metal surfaces^{150, 157}. The spin density distribution also was computed and the iso-surface at a value of 0.01e/ \AA^3 is plotted in Figure 6-6 d. As can be seen, the down spin is mainly distributed at the contact point of Fe and C₆₀.

6.1.2.2.2. Fe₂C₆₀

Compared to single Fe atom doping, two Fe atoms have more valence electrons available for charge transfer to C₆₀. Integration of the PDOS from the bottom of the valence band to the Fermi level shows a charge transfer of 1.76e⁻ from two Fe atoms to the molecule, 0.81e⁻ more than the single Fe doping. This number again is slightly lower compared to the Bader analysis. These electrons are accumulated at the tail of the LUMO band, as seen in Figure 6-7 a. Due to the orbital energy matching, the HOMO and HOMO-1 bands of C₆₀ hybridize with the Fe orbitals. As the PDOS of Fe orbitals broadens, the HOMO and HOMO-1 bands of C₆₀ spread out. This broadening enhances the hybridization (or vice versa) and the covalent character of the Fe-C bonds.

The large charge transfer to C₆₀ doubles the magnetic moment of C₆₀, compared to the FeC₆₀ system, in both GGA and LDA calculations (Table 6-3). Figure 6-7 b shows

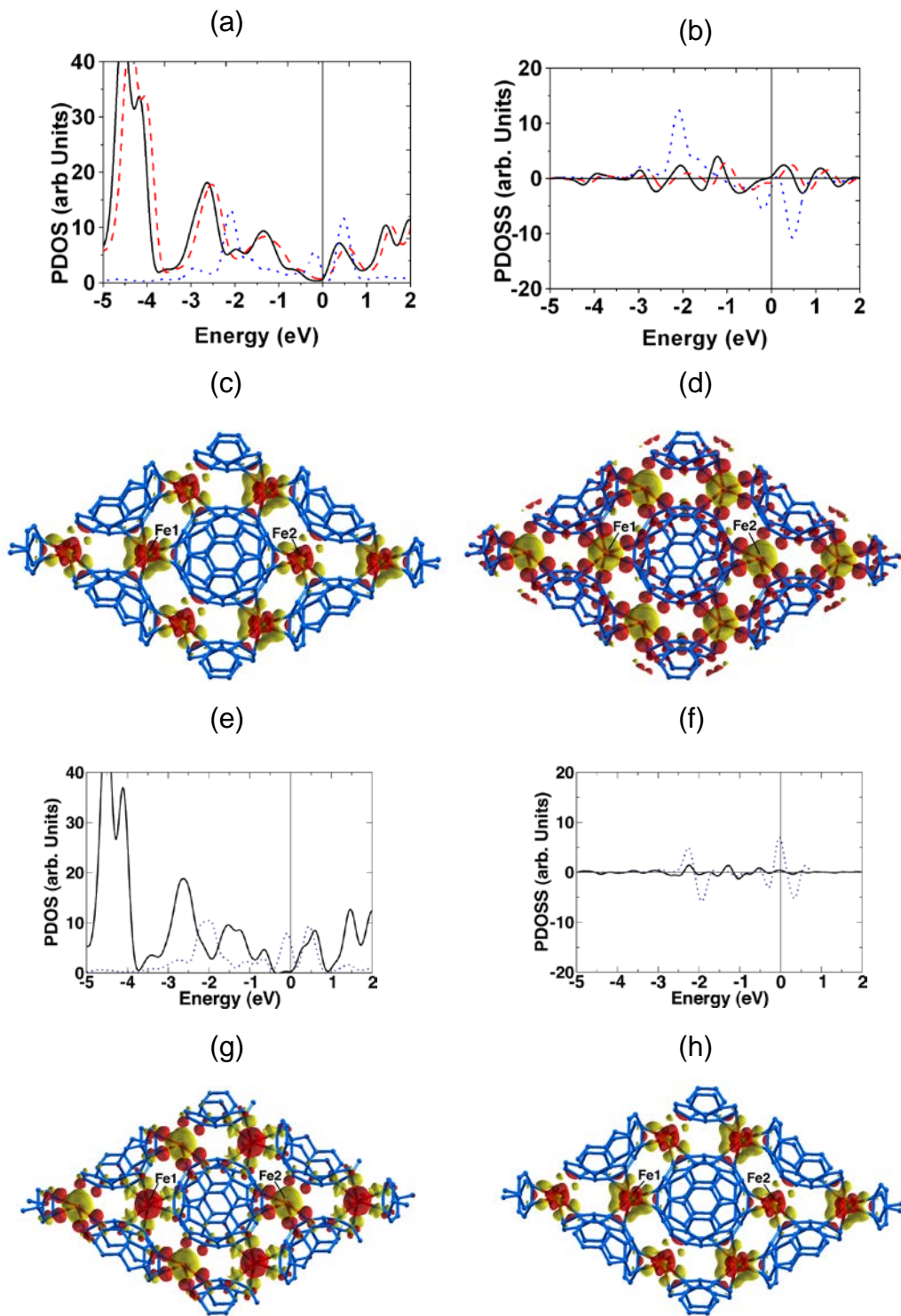


Figure 6-7. Projected densities of states (PDOS) and projected densities of spin states (PDOSS) on monolayer C_{60} and two Fe atoms for $\text{Fe}_2\text{C}_{60}/h\text{-BN}/\text{Ni}(111)$. Panels (a)-(d) are for the FM state: (a) PDOS of C_{60} in GGA (black solid) and LDA (red dash), and PDOS of Fe in GGA (blue dot), Fermi level at energy of 0; (b) PDOSS of C_{60} in GGA (black solid) and LDA (red dash), and PDOSS of

Fe in GGA (blue dot). Panel (c) and (d) are iso-surfaces of charge density difference and spin density, with yellow representing charge accumulation in (c) and positive spin in (d), and red charge depletion and negative spin. Panel (e)-(f) present the same information as panel (a)-(d) for the AFM state.

the PDOSS distributions on C₆₀ and two Fe atoms. The PDOSS on C₆₀ in Fe₂C₆₀ is similar to that in FeC₆₀ (Figure 6-6 b), except for the higher population of electrons with the spin-minority elements observed on the energy region from -0.9eV to the Fermi level, a consequence of enhanced charge transfer to C₆₀. We again have computed the charge density difference and spin density. The iso-surfaces of values 0.04e/Å³ and 0.01e/Å³ for charge and spin, respectively, are depicted in Figure 6-7 c and d. Compared to Figure 6-1, charge transfer to C₆₀ is enhanced and still concentrated at contact point. The spin density spreads out more compared to one Fe doping.

For Fe₂ doping, there is an AFM state with energy almost the same as the FM state (~10⁻⁴ eV higher in energy). For this state, the charge transfer to C₆₀ is 1.74e⁻ and 1.27e⁻ from Bader and PDOS (Figure 6-7 e) analysis, respectively. The net spin of the system and net spin on C₆₀ (Figure 6-7 f) are zero. Figure 6-7 g and h are the same plots as in Figure 6-7 c and d but for the AFM states. The two charge difference patterns are very similar (c and g) but the two spin patterns are substantially different.

6.1.2.2.3. Fe₃C₆₀

Figure 6-8 (a) shows the PDOSs of C₆₀ and 3 Fe atoms. The distortion in HOMO and LUMO bands suggests a large charge transfer from Fe to C₆₀ and strong hybridization between the Fe and C₆₀ orbitals. We obtain a charge transfer of 1.95 electrons/molecule to C₆₀, increasing by 11% from Fe₂C₆₀. Compared to the 2.66 e⁻ from the Bader analysis, the PDOS under estimated the charge transfer by more than half of an electron. However, this discrepancy does not change the observed trend.

C_{60} doped with three Fe atoms has a rather high spin-down population near the Fermi level, as seen in Figure 6-8 b. The negative magnetic moment of C_{60} originates from the majority of transferred electrons being spin-down. These electronic and magnetic phenomena imply that heavy metal doping broadens states in C_{60} to the extent that features of the C_{60} -like orbitals start to vanish. The magnetic moment of C_{60} retains the same orientation (anti-parallel to that of the Fe atoms). Its absolute value, calculated in GGA, is doubled from Fe_1 -doped C_{60} , and slightly larger than that in Fe_2 -doped C_{60} (see Table 6-3). In contrast, the absolute value calculated in LDA becomes smaller by 0.07 (μ_B), compared to that in Fe_2 -doped C_{60} . Figures 6-8c and d depict charge difference, and spin density, respectively. A close view of the spin density (Figure 6-8e) shows that while spin on each Fe atom is positive (or spin-up) (yellow) there is a spin-down distribution (red) between the two Fe atoms. This is a result of interaction with C_{60} molecule since there is no spin-down population between two isolated Fe atoms. The molecule transfers some spin-down electrons back to Fe to enhance Fe bonding.

6.1.2.2.4. Fe_4C_{60}

Incorporation of four Fe atoms enhances the interaction between Fe and the C_{60} monolayer. Figure 6-9 a shows the PDOS of C_{60} and 4 Fe atoms. Similar to the Fe_3C_{60} system, the C_{60} -like feature vanishes because of the large charge transfer from the Fe orbitals to the π -like orbitals of C_{60} and the strong hybridization between the Fe 3d and C_{60} orbitals. The charge transfer toward C_{60} is 2.10 electron/molecule, an increase of 8% compared to that in the Fe_3C_{60} system. Note again, this number is smaller than that from Bader's method (3.29e⁻).

For heavily doped C_{60} , Li *et al.*¹⁶² studied the electronic states of an Yb-doped C_{60} monolayer on Ag(111) using the synchrotron radiation photoemission technique. Doping

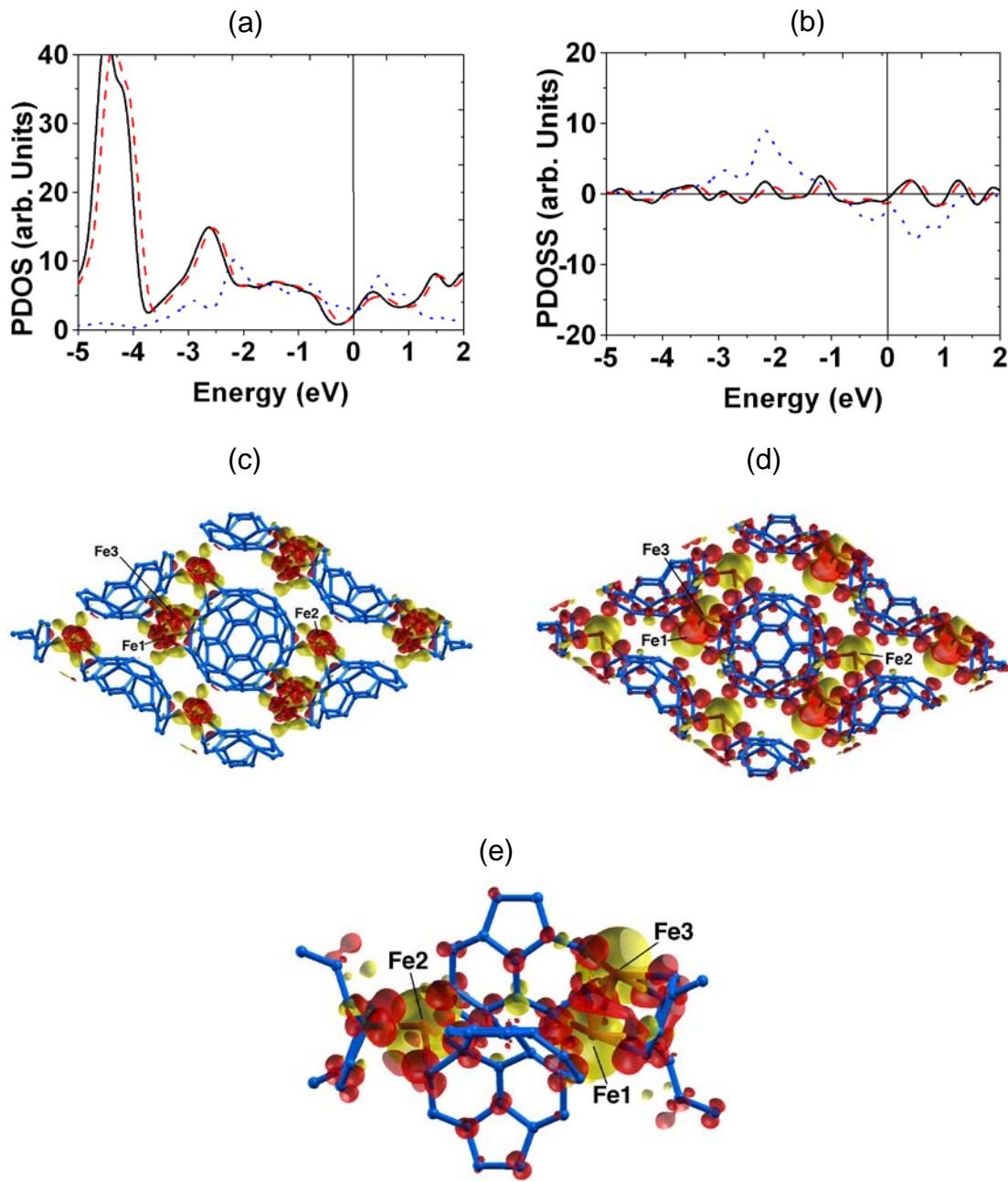


Figure 6-8. Projected densities of states (PDOS) and projected densities of spin states (PDOSS) on monolayer C_{60} and three Fe atoms for $Fe_3C_{60}/h\text{-BN}/Ni(111)$: (a) PDOS of C_{60} in GGA (black solid) and LDA (red dash), and PDOS of Fe in GGA (blue dot), Fermi level at energy of 0; (b) PDOSS of C_{60} in GGA (black solid) and LDA (red dash), and PDOSS of Fe in GGA (blue dot). Panel (c) and (d) are iso-surfaces of charge density difference and spin density, with

yellow representing charge accumulation in (c) and positive spin in (d), and red charge depletion and negative spin. Panel (e) is a close view of spin density.

with more than 3 Yb atoms/ C_{60} causes the electronic properties of the sample to change from metallic to semi-conducting because of the modulation in the LUMO+1 band.¹⁶² Li's observations suggest that calculations beyond GGA and LDA should be performed. Therefore, we have added an additional U term for the treatment of strong on-site 3d electron-electron interactions on Fe ($U = 4.5$ eV) as suggested by Cao *et al.*¹⁶³. Our focus here is on the electron density of the band of C_{60} near the Fermi level. Our results show that neither GGA+U nor LDA+U produces a band gap near E_F (see Figure 6-9 a), which means the system stays metallic.

Similar to previous systems, the minority-spin levels again dominate the Fermi level, as seen in Figure 6-9 b. The calculated magnetic moment on C_{60} is 0.52 (μ_B) in GGA+U (or 0.54 (μ_B) in LDA+U), which is slightly smaller than the GGA (or LDA) result, as seen in Table 6-1. Inclusion of Coulomb interactions on the Fe 3d orbital has a strong effect on the spin states of the system. The magnetic moment of Fe using GGA+U increases by 20% from the GGA result while the value calculated using LDA+U increases by 23% from the LDA. The charge difference and spin density are also similar to Fe₃-doped C_{60} , except that the detailed patterns are more complicated due to the added Fe atoms. Therefore, they are not shown in the Figure 6-9.

6.1.2.2.5. $Fe_{15}C_{60}$

The next questions are: how many electrons at most can a C_{60} accept? And would the electronic signature (valence bands) of the C_{60} molecules be seen when the system is heavily doped? To understand the large n limit, we have investigated $Fe_{15}C_{60}$ on the

same supporting surface. Figure 6-10 a shows the PDOS of the heavily doped C₆₀ and 15 Fe atoms. Substantial charge transfer, 4.61 electrons/molecule (compared to 5.24 e⁻ from the Bader analysis), and strong hybridization smear the C₆₀-like valence band completely. It is difficult to distinguish the HOMO and LUMO peaks in the spectrum of C₆₀. The doped C₆₀ retains metallic characteristics. Saturation in charge transfer to C₆₀ is not observed.

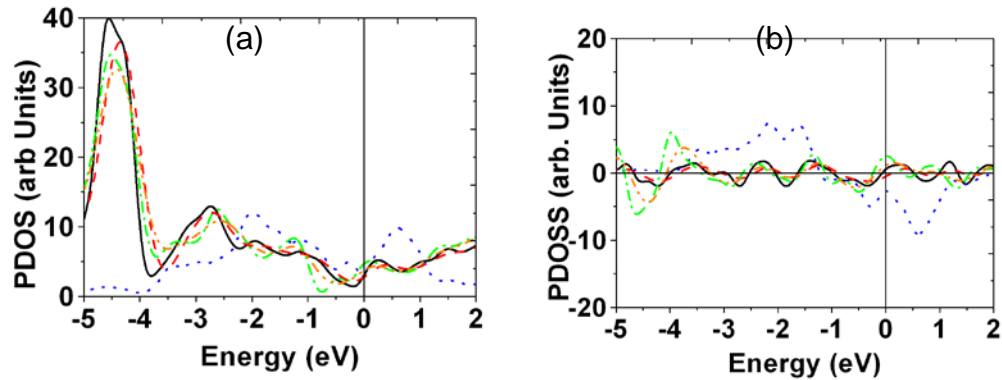


Figure 6-9. Projected densities of states (PDOS) and projected densities of spin states (PDOSS) on monolayer C₆₀ and four Fe atoms for Fe₄C₆₀/h-BN/Ni(111): (a) PDOS of C₆₀ in GGA (black solid), LDA (red dash), GGA+U (green dash-dot) and LDA+U (orange dash-dot-dot), and PDOS of Fe in GGA (blue dot), Fermi level at energy of 0; (b) PDOSS of C₆₀ in GGA (black solid), LDA (red dash) and GGA+U (green dash-dot) and LDA+U (orange dash-dot-dot), and PDOSS of Fe in GGA (blue dot).

Figure 6-10 b shows the spin-different distributions of C₆₀ and 15 Fe atoms. The magnetic moment of Fe obtained within either GGA or LDA becomes much larger than those in Fe_nC₆₀ ($n = 1-4$) as expected. In contrast, the magnetic moment of C₆₀ drops slightly from Fe₄C₆₀ from GGA calculations and maintains nearly the same value using LDA (Table 6-3).

For the same reason as for the 4-Fe system, we performed calculations with inclusion of the Hubbard U. Our results show again that the system is metallic. We note

that the magnetic moment on Fe atoms increases substantially as a results of inclusion of the U term.

Table 6-3. Spin populations on the individual orbitals of Fe and C₆₀, ↑ spin up, ↓ spin down, *m* magnetic moment.

	Fe				C ₆₀		
	s	p	d	m _{Fe} (μ _B)	s	p	m _{C60} (μ _B)
FeC₆₀/h-							
BN/Ni							
GGA	↑0.01	↑0.01	↑2.42	+2.45	↓0.01	↓0.35	-0.37
LDA	↑0.04	↑0.01	↑1.92	+1.96	↓0.01	↓0.38	-0.38
Fe₂C₆₀/h-							
BN/Ni							
GGA	↑0.03	↑0.02	↑4.66	+4.71	↓0.03	↓0.68	-0.71
LDA	↑0.07	↑0.01	↑3.38	+3.46	↓0.03	↓0.67	-0.70
Fe₃C₆₀/h-							
BN/Ni							
GGA	↑0.03	↑0.03	↑6.76	+6.82	↓0.04	↓0.71	-0.76
LDA	↑0.03	↑0.03	↑6.40	+6.46	↓0.02	↓0.60	-0.63
F^e₄C₆₀/h-							
BN/Ni							
GGA	↑0.04	↑0.03	↑9.14	+9.21	↓0.04	↓0.66	-0.70
LDA	↑0.03	↑0.05	↑8.74	+8.82	↓0.03	↓0.55	-0.58
GGA + U	↑0.02	↑0.01	↑11.00	+11.03	↓0.04	↓0.48	-0.52
LDA+U	↑0.01	↑0.01	↑10.75	+10.77	↓0.03	↓0.51	-0.54
Fe₁₅C₆₀/h-							
BN/Ni							
GGA	↑0.02	↓0.13	↑29.47	+29.36	↓0.05	↓0.53	-0.58
LDA	↓0.02	↑0.02	↑24.29	+24.29	↓0.03	↓0.49	-0.51
GGA+U	↑0.08	↓0.01	↑38.80	+38.87	↓0.06	↓0.49	-0.54
LDA+U	↓0.05	↓0.11	↑30.70	+30.54	↓0.05	↓0.62	-0.66

6.1.3 Summary and Conclusions

The structural, electronic and magnetic properties of the Fe_n-C₆₀ complexes (*n* = 1-4 and 15) were investigated in this chapter via DFT. The amount of charge transfer increases monotonically as the number of Fe atoms increases. At low Fe doping concentration (*n* = 1 or 2), individual Fe atoms diffuse in the interstitial spaces of the C₆₀ monolayer and bind to C₆₀. The binding energy is mainly due to the Fe-C bonds. When *n*=3 or more, Fe atoms cluster around the C₆₀ molecule as well as bind to C₆₀.

molecules. The binding energy is therefore from both Fe-Fe and Fe-C bonds. Large Fe concentration gives rise to higher binding energy in the Fe_nC_{60} complex but far less than the cohesive energy, 4.28eV/Fe atom,¹⁶⁶ of crystalline Fe (fcc). Charge transfer, as a function of number of metal atoms, was investigated by both the Bader analysis and PDOS, with the former giving a larger transfer to C_{60} than the latter. Doping with Fe atoms results in modifications of the C_{60} LUMO-derived bands, which are enhanced by

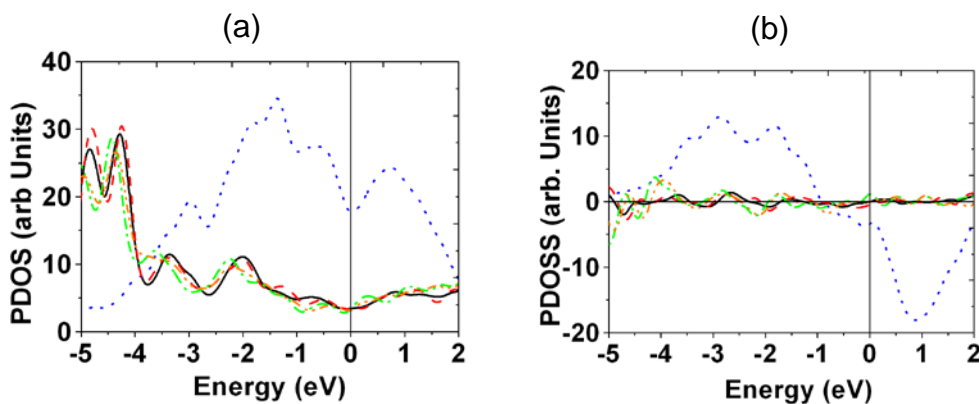


Figure 6-10. Projected densities of states (PDOS) and projected densities of spin states (PDOSS) on monolayer C_{60} and fifteen Fe atoms for $\text{Fe}_{15}\text{C}_{60}/\text{h-BN}/\text{Ni}(111)$: (a) PDOS of C_{60} in GGA (black solid), LDA (red dash), GGA+U (green dash-dot) and LDA+U (orange dash-dot-dot), and PDOS of Fe in GGA (blue dot), Fermi level at energy of 0; (b) PDOSS of C_{60} in GGA (black solid), LDA (red dash) and GGA+U (green dash-dot) and LDA+U (orange dash-dot-dot), and PDOSS of Fe in GGA (blue dot).

increasing electron occupation. Analysis of PDOS shows that the charge transfer occurs mainly between the Fe- $3d$ orbitals and the t_{1u} orbitals of C_{60} , indicating that ionic character dominates the Fe- C_{60} bonding. Hybridization also is observed among the C_{60} and Fe orbitals (mainly with Fe s and d orbitals). Therefore, a covalent effect also exists in the Fe- C_{60} bonding. Furthermore, doping with Fe induces a negative magnetic moment in C_{60} , aligning it anti-parallel with Fe. The value of this moment varies roughly within a factor of two. In contrast to charge transfer, magnetic moment values obtained

by Bader's method and PDOS analysis are very close in value. Heavy Fe-doping does not destroy the structure of C₆₀, but deforms the electronic structure of C₆₀. Unlike alkali metal doped system, the Fe-doped systems do not undergo a metal-semiconductor transition. Our results present a comprehensive description of the interaction between the transition-metal atom/cluster and the C₆₀ thin film, which is important for understanding nano-structured, quasi-two dimensional conducting systems.

6.2 C₆₀ on defected Au(111) surface³

Surfaces with a regular array of energetic sites can be utilized as templates for growing nano-scale structures from site-specific nucleation.¹⁶⁸⁻¹⁷² For example, the Au(111) surface with the so-called herringbone reconstruction^{173, 174} can form a surface dislocation network, and can guide the growth of ordered two-dimensional arrays of metal islands. The reactive "elbow sites",^{169, 175} where the nucleation of the metal islands takes place, are the key for such a guiding function. In terms of the C₆₀ molecule adsorption on Au(111) at room temperature, the formation of closed-packed molecular monolayers long has been identified as a consequence of nucleation at step edges without any preferential attachment of C₆₀ molecules to the elbow sites.¹⁷⁶⁻¹⁷⁹ However, recent investigations have shown that the adsorption of C₆₀ molecule on noble metal surface involves vacancies at room temperature.¹⁸⁰ Single-atom vacancy pit has been proposed for Ag(111) adsorption,¹⁸⁰ while the seven-atom pit model has been proposed for Cu(111).¹⁸¹

Our collaborators have performed an experiment involving C₆₀ molecule adsorption on the Au(111) surface.¹⁶⁷ The adsorption of C₆₀ molecule on Au(111) is

³ This work has been published in Physical Review B.¹⁶⁷

quite different at low temperature compared to room temperature. On one hand, at 46 K, the C₆₀ molecules, either single molecule or small clusters, prefer to attach on the elbow sites. As the temperature goes up, the molecules sitting at the elbow sites start to move away and aggregate to island. Most elbow sites are depleted of individually adsorbed molecules by 284K. On the other hand, surprisingly, if the C₆₀ molecules are deposited onto Au(111) at room temperature, single molecule adsorption at the elbow sites is observed. This “controversy” can only be explained by different bonding configurations at low temperature and room temperature. Following the observation that the Au atoms can jump out of the elbow site, it is proposed that a pit vacancy model may apply to the system, i.e. the C₆₀ molecules are adsorbed onto the vacancies formed from moving of the Au atoms at room temperature. We thus performed DFT calculations to investigate the adsorption of C₆₀ molecules onto pit vacancy model on Au(111) surface.

6.2.1 Method and Computational Details

As before, we performed plane wave PAW^{53, 83} DFT²⁸ calculations with VASP^{84, 85} to investigate adsorption energies of C₆₀ molecules on one-, three-, and seven-atom pits. We used local density approximations^{29, 30} (LDA). A seven-layer slab with the two bottom layers fixed was employed to simulate the Au(111) surface, on top of which a monolayer C₆₀ was adsorbed. The thickness of the vacuum between the molecule and neighbor metal surface was larger than 15 Å and a (3 × 3 × 1) Monkhorst-Pack k-point mesh¹⁰⁷ was used.

6.2.2 Results and Discussions

On all three defect sites, the most stable configurations correspond to a hexagon of the C₆₀ in contact with the surface (shown in Figure 6-11). The center of the hexagon

aligns with the center of the vacancy along the z-direction. Geometry optimization shows very little change in C₆₀ molecular structure in all three cases. We follow the same method by Li *et al.*¹⁸⁰ to describe the surface reconstruction in the vertical (z) direction (See Table 6-4). On average, atoms in the bottom hexagon of C₆₀ molecules are 1.80 Å, 1.68 Å and 0.15 Å above the first Au layer in one-atom, three-atom, and seven-atom pits, respectively. Vacancies shorten the distance between first layer and second layer Au atoms locally compared to a perfect Au(111) surface.

We also calculated the intra-layer buckling amplitude (Δ_i). The largest buckling occurs in the second layer in systems with one-atom and three-atom pits, and the first layer in the system with a seven-atom pit which causes larger buckling in layer 3-5 (indicated by Δ_{3-5}) than the two smaller pits.

To investigate surface reconstruction, we also examined the in-plane displacement of atoms near the three vacancies. Table 6-4 lists the calculated deviations of lateral positions (compared to positions in a perfect Au(111) surface) of those atoms right next to the centers of vacancies. Only atoms in the first and second layers show significant lateral displacement, denoted as Δ_{xy-1} and Δ_{xy-2} , respectively. Interestingly, atoms in the first layer appear to be repelled from the center of vacancies, especially near the seven-atom pit where atoms move by 0.18 Å; but in the second layer, atoms near a vacancy are attracted inward in the one-atom and three-atom cases. Atoms in the second layer near a seven-atom pit move outward just as ones in the first layer because of the direct contact with a C₆₀ molecule.

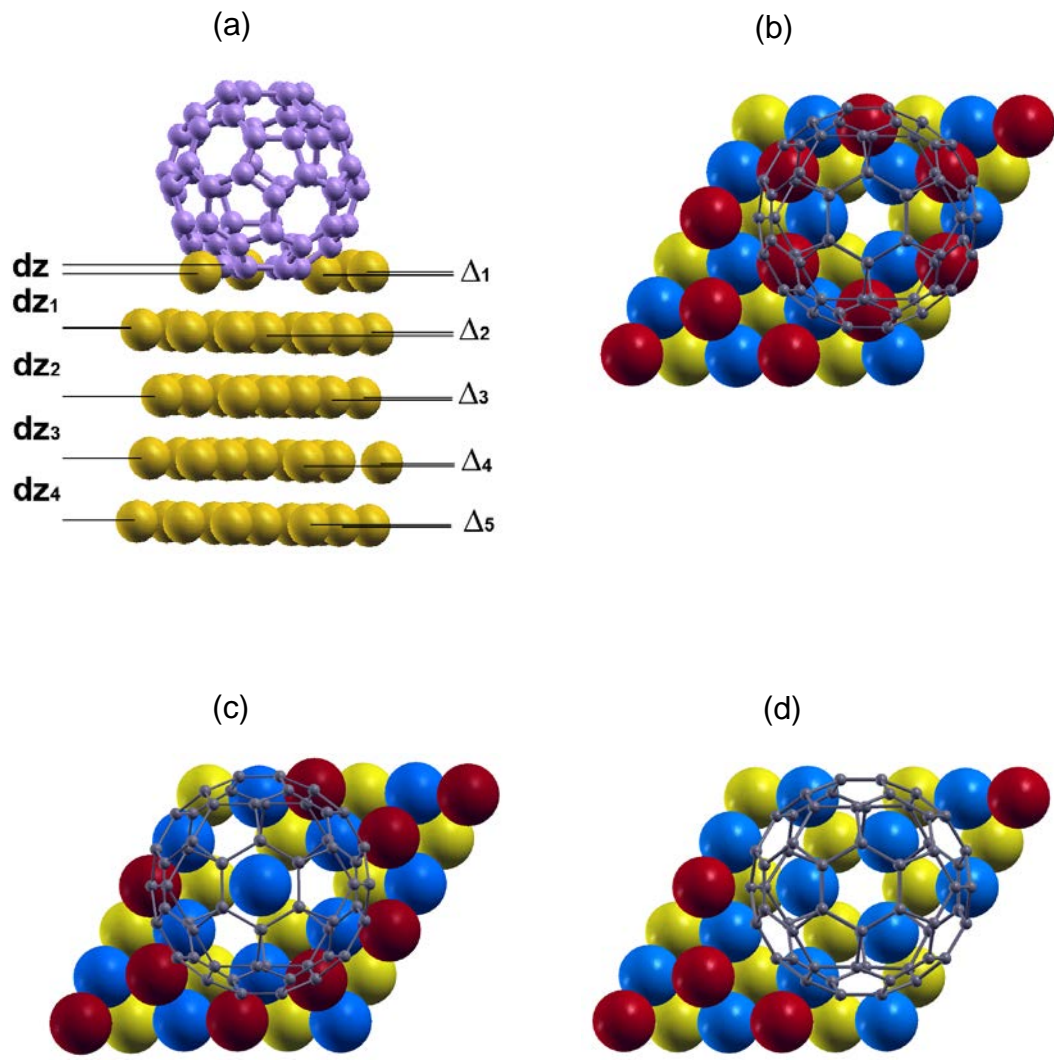


Figure 6-11. C_{60} molecules on vacancy sites of Au(111) surface. Panel (a) is side view of C_{60} on a 7-atom pit. Panel (b), (c) and (d) are top view of C_{60} on 1-, 3- and 7-atom pits, respectively, in which first, second and third Au layers are shown in dark/red, grey/blue, and light/yellow, respectively.

Calculated adsorption energies are 2.07 eV, 2.33 eV and 2.56 eV for one-atom, three-atom and seven-atom vacancies, respectively. This trend agrees with our intuition. Compared to a perfect Au surface of 1.2 eV,¹⁷² the energy difference signals the cause of defect trapping of C_{60} since the translational motion of the molecule on Au(111) is nearly barrierless. At 46 K, both individual molecules and small clusters appear 6.2 Å

above the substrate surface in STM images. The individual molecules observed at room temperature are about 4 Å above the surface, which is in good agreement with the seven-atom pit model shown in Figure 6-11 a and d. Height measurement in STM is not always a reliable method for measuring the position of adsorbed species because of electronic effects. However, the 2.2 Å difference in measured heights is too large for a pure electronic effect. This height difference is in very good agreement with that measured for C₆₀ molecules sitting on the upper terrace and those on the lower terrace sharing a common step.¹⁸²

Table 6-4. Structure and energies: dz is the average inter-planar distance, Δ the average intra-layer buckling amplitude, and Δ_{xy} the average lateral displacement of atoms surrounding a vacancy (see Figure 6-11)

	1-atom pit	3-atom-pit	7-atom pit
dz (Å)	1.80	1.68	0.15
dz ₁ (Å)	2.32	2.27	2.25
dz ₂ (Å)	2.34	2.35	2.36
dz ₃ (Å)	2.35	2.35	2.35
dz ₄ (Å)	2.35	2.35	2.35
Δ ₁ (Å)	0.04	0.05	0.10
Δ ₂ (Å)	0.09	0.11	0.03
Δ ₃ (Å)	0.01	0.01	0.03
Δ ₄ (Å)	0.01	0.01	0.04
Δ ₅ (Å)	0.01	0.01	0.01
Δ _{xy_1} (Å)	0.04	0.18	0.02
Δ _{xy_2} (Å)	-0.05	-0.06	0.03
Adsorption Energy (eV)	2.07	2.33	2.56

In conclusion, our DFT calculations on the strong bonding configuration observed at room temperature show that the molecules are trapped by seven-atom pits with adsorption energy 2.56 eV. This value is significantly higher than the energy for a C₆₀ sitting on a defect-free Au(111), in a good agreement with the experiment.

CHAPTER 7

SYMMETRY BREAKING INDUCED BY EPITAXIAL STRAIN IN BIMNO₃ THIN FILM

Multiferroics normally refers to materials exhibiting the coexistence of magnetic and electric orders.¹⁸³ Due to both potential device applications and the physical essence of this unique property, extensive experimental and theoretical effort has been drawn in multiferroics. The ferromagnetic and ferroelectric BiMnO₃ (BMO) is one of the most fundamental members in the multiferroic family. Bulk BMO has been determined to be FM and FE by early experiments.¹⁸⁴ The saturated magnetization of bulk BMO is 3.6 μ_B at 5K and the electric polarization is observed as 62 nC/cm² at 87K. Density functional studies showed that the ferroelectricity is caused by the displacement of Bi atoms from centrosymmetric positions, due to the 6s² electron lone pairs¹⁸⁵. This theory contradicts recent experiments, in which C2/c symmetry is observed by both electron and neutron diffraction¹⁸⁶. The inversion symmetry is further supported by DFT with Hubbard-like on-site interaction correction.¹⁸⁷

BMO thin film has been grown on SrTiO₃ (STO), introducing a -0.77% strain.¹⁸⁸⁻¹⁹¹ The compressive strain greatly raises the electric polarization (16 μ C/cm² by Son *et al.*¹⁹¹ and 23 μ C/cm² by Jeen *et al.*¹⁹⁰), yet reduces the magnetic moments (2.2 μ_B /Mn by Eerenstein *et al.*¹⁸⁸ and 1 μ_B /Mn by Jeen *et al.*¹⁹⁰). The strain effect on BMO thin film was studied by Hatt *et al.* using density functional theory. They found that the C2/c symmetry remains up through as high as 4% strain, and the calculated electric polarization is at most 0.1 μ C/cm².¹⁹² The origin of the ferroelectricity in BMO, both bulk and epitaxial strained thin film, therefore remains in controversy. To understand the ferroelectricity, a hidden long-range AFM interaction has been suggested to induce C2/c symmetry breaking.^{193, 194} In fact, slight frustration in orbital ordering¹⁹⁵ (OO) exists even

in BMO bulk.¹⁹⁶ Such frustration could be enhanced in the strained thin film, possibly altering the FM ground state.¹⁹⁷ The fact that the saturated magnetic moment decreases in thin film implies the existence of AFM ordering. In addition, the ordered oxygen vacancy has been proposed to understand the ferroelectric behavior.^{198, 199}

In this chapter, we study the strain effect on BMO thin film, as well as the magnetic properties, using DFT. Note that Hatt *et al.* only considered FM order.¹⁹² We find that inversion symmetry breaking can be caused by the emergence of AFM order in a strained thin film. Due to the limited experimental data of the structure of the BMO thin film, only C2/c symmetry is considered in our calculation.

7.1 Method and Computational Details

Our calculations utilized the DFT+U method²⁸ within LDA³¹ for structural optimization and the HSE06 hybrid functional³⁶ for more refined energy and polarization calculations, which is implemented in plane-wave based VASP package^{84, 85}. For Mn 3d electrons, we used U=6 eV and J=0.8 eV. A $6 \times 6 \times 4$ k-point mesh¹⁰⁷ and 500eV energy cut-off were used. Thresholds for self-consistent calculation and structure optimization were set as 10^{-5} eV and 0.02 eV/Å, respectively. The polarizability calculations were based on the Berry phase method^{57, 58} as described in Section 2.5.

7.2 Results and Discussions

Figure 7-1a shows the conventional monoclinic unit cell with C2/c symmetry of bulk BMO. Its distorted perovskite-type 40-atom unit cell is determined experimentally to have $a=9.54$ Å, $b=5.61$ Å, $c=9.86$ Å, $\alpha=\gamma=90^\circ$, and $\beta=110.65^\circ$.¹⁸⁶ Experimentally, the (111) plane of the monoclinic unit cell (also refers to pseudocubic (001)) is oriented to the SrTiO₃ (001) surface, causing a compressive -0.77% strain.¹⁹⁰ For simplicity, we use

the 20-atom primitive cell instead, as shown in Figure 7-1b. The axis of the primitive cell (indicated by subscript 0) can be linked to the monoclinic unit cell by

$$\vec{a} = \vec{a}_0 + \vec{b}_0, \quad \vec{b} = \vec{b}_0 - \vec{a}_0, \quad \text{and} \quad \vec{c} = \vec{c}_0. \quad (7-1)$$

Thus the (011) plane of the primitive cell (denoted as $(011)_{\text{pr}}$) is then the $(001)_{\text{ps}}$ plane.

We first fully optimized the primitive cell using LDA+U. We introduced the epitaxial strain onto $(011)_{\text{pr}}$, following the method described in Hatt's paper.¹⁹² The b_0 and c_0 are altered according to the strain, yet the volume and b_0/c_0 ratio are conserved. The a_0 axis is varied in the direction perpendicular to the $(011)_{\text{pr}}$ plane to keep the volume.

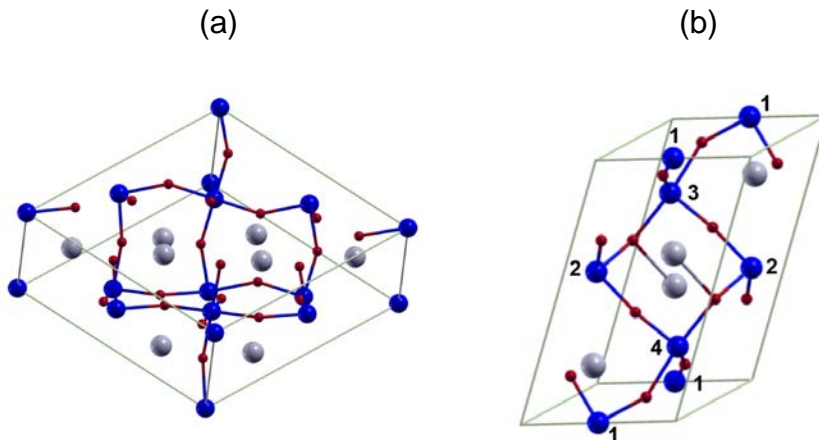


Figure 7-1. (a) Monoclinic 40-atom unit cell of BMO. (b) 20-atom primitive cell of BMO. Bi atoms are in grey. Mn atoms are large blue (dark) spheres. O atoms are small red (dark) spheres.

One primitive cell has four Mn atoms, numbered as in Figure 7-1b. Besides the ferromagnetic configuration (FM), magnetic orders can possibly be antiferromagnetic, including (up, up, down, down) (AFM_1), (up, down, up, down) (AFM_2), and (up, down, down, up) (AFM_3), as well as ferrimagnetic, including (up, down, down, down) (Ferri_1), (down, up, down, down) (Ferri_2), (down, down, up, down) (Ferri_3) and (down, down, down, up) (Ferri_4). Note that AFM_1 is the G-type AFM order. We need

to stress that the other AFM orders, AFM_2 and AFM_3, are similar to the E-type AFM order which is observed in TbMnO_3 .^{200, 201} E-type AFM features zigzag chains of the parallel spins in one plane, while AFM_2 and AFM_3 have zigzag chains in both in-plane and out-of-plane directions. This is due to its highly distorted and incommensurate structure. For the same reason, C-type and A-type AFM configurations cannot be considered in this case.

After optimization of internal coordinates by LDA+U, energies of each spin configuration were then refined with the HSE06 hybrid functional. We found that AFM_2 and AFM_3 are energetically degenerate, which can be understood by symmetry, so we only present results for AFM_2 in the rest of the chapter. The AFM_2 and AFM_3 orderings are energetically more stable than AFM_1 (G-type). The Ferri_2 is the most stable among four ferrimagnetic configurations for all strains we have investigated. LDA+U calculations show that FM is the ground state from 0 to -4 percent of strain. Under -5% strain, Ferri_3 is more stable than FM, by 5 meV per formula unit (shown in Figure 7-2 a). In addition, different U values in the LDA+U calculation (from 3 eV to 8 eV) do not change the prediction of the ground state under strain. However, the HSE06 hybrid functional predicts a different situation (shown in Figure 7-2b). According to the HSE06 calculations, AFM_2 state is more stable than FM and Ferri_2, in the range of -1.9% to -2.7% compressive strain, while FM is the ground state under 0% to -1.9% strain. For higher strain, from -2.7% to -5%, Ferri_3 is more stable than the other two. Since the HSE06 hybrid functional has been proven to be more accurate at describing energetic information,²⁰² it is reasonable to believe the emergence of the AFM_2 state would occur under about 2% compressive strain.

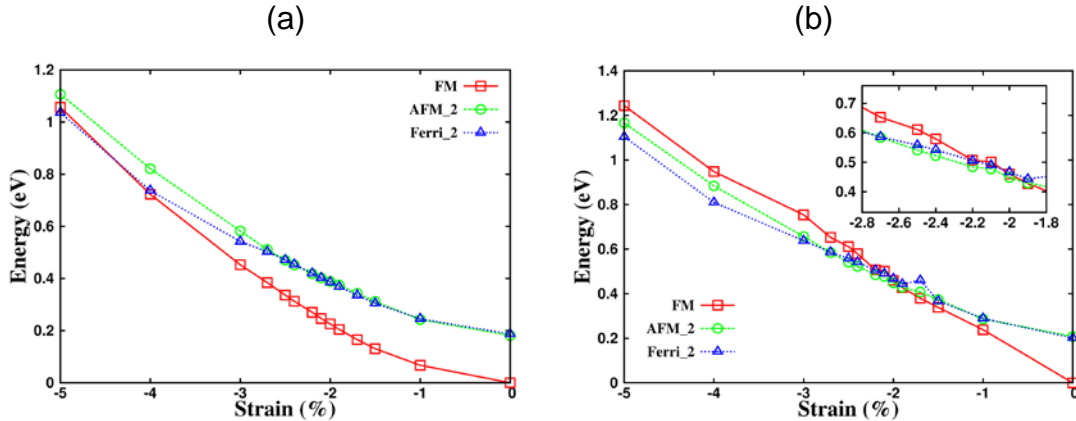


Figure 7-2. The energies per primitive cell for FM, AFM_2, and Ferri_2 magnetic configurations. (a) is the LDA+U result and (b) is from the HSE06 hybrid functional. Only the most stable AFM and Ferri orders are shown.

It is interesting to discuss the inversion symmetry for different spin configurations. FM always keeps inversion symmetry, so we cannot expect inversion symmetry breaking when FM is the ground state. AFM_1 is G-type AFM, which is also centrosymmetric, while AFM_2 breaks inversion symmetry. The lowest ferrimagnetic configuration, Ferri_2, is still centrosymmetric. Therefore, the origin of the ferroelectric behavior of strained BMO can be explained by the switching of the magnetic order under compressive strain, from FM to AFM_2. Under appropriate strain (between -1.9% and -2.7%), the non-centrosymmetric spin configuration of the ground state induces structural centrosymmetry breaking, leading to the emergence of ferroelectricity. The non-uniformed strain explanation thus is supported by our calculation.

Figure 7-3a shows the pattern of atomic displacements within a primitive cell under the -2.2% compressive strain, when AFM_2 is the ground state. Apparently the displacements are non-centrosymmetric. Fig. 7-3b shows a fractal of the $(001)_{ps}$ plane of BMO under 2.2% compressive strain. The Mn-O-Mn angles are in the range of 146° to 155° , indicating a strong octahedral tilting. Spin density of the states within 2 eV

below Fermi level is also plotted. Compared to the spin density of the FM ground state in bulk form (not shown here), orientations of Mn e_g orbitals remain about the same, except the one at Mn3 atom. The orientation is initially the same as Mn4 atom in bulk (in-plane), but switches to out-of-plane under strain. It is also elongated in the Mn2'-Mn3 direction. In addition, such a pattern does not change if a 40-atom unit cell is used.

We then calculated the electric polarization for all the spin configurations, using the Berry-phase method combined with the HSE06 functional. The FM state shows quite low polarization under all strains, agreeing with Hatt et al. With the Ferri_2 configuration, BMO also shows nearly zero polarization for all strains. In contrast, the AFM_2 configuration shows higher electric polarization. Combined with the previous energy calculation, we plot the electric polarization of the ground states versus strain in Figure 7-3c. Clearly, the BMO system with the AFM ground state has the electric polarization, which is comparable to experiment results.

One may wonder that the strain created by STO may not be enough to switch the ground state from FM to AFM_2. Though STO only creates compressive -0.77% strain, the strain may not be evenly distributed over the BMO thin film. Thus, the local strain is still possibly higher than -0.77%, which would allow the FM to AFM_2 transition to happen locally. Overall, the electric dipole could still be observed and a lower magnetic moment per Mn atom would appear.

We need to stress that we do not exclude the possibility of other magnetic orderings, for example, long-range order and spin waves. Both long-range AFM orders and spin waves are much more complicated and expensive to treat, especially for the HSE06 calculation. However, we have proven that FM is not the ground state. Inversion

symmetry would be broken under certain strain, and the electric polarization is created. It is also possible that strain can induce a structural phase transition, which could destroy the inversion symmetry, however no experiment has observed such a behavior.

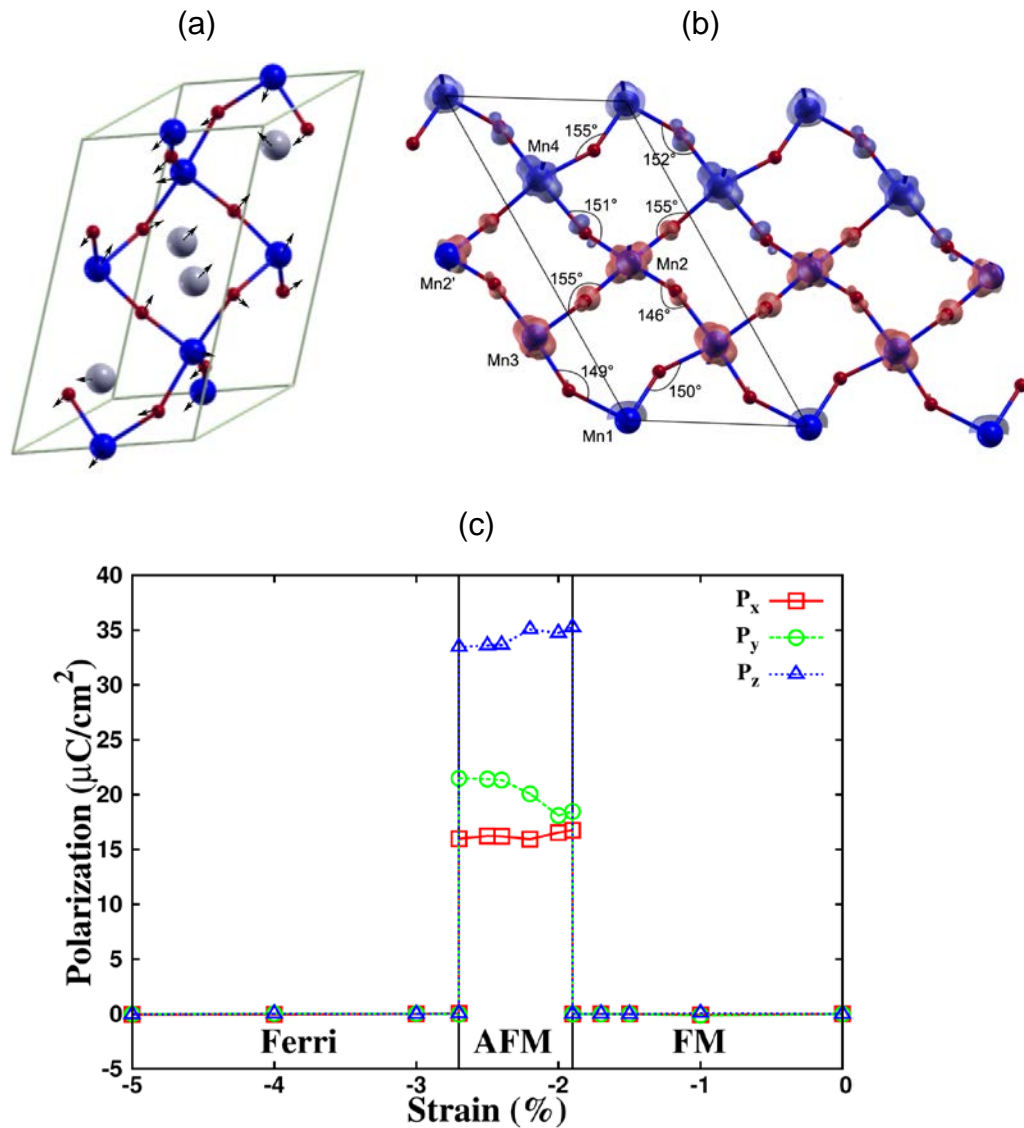


Figure 7-3. (a) The atomic displacements of a primitive cell under 2.2% strain. (b) Isosurface of spin-density of the states within 2 eV below Fermi surface of BMO thin film under 2.2% strain. The isovalue is $0.17 \text{ e}/\text{\AA}^3$. Blue refers to spin-up and Red refers to spin-down. (c) The calculated polarization of the ground state corresponding to the strain.

7.3 Summary and Conclusions

This chapter reports the study of the magnetic and ferroelectric properties of epitaxially strained BMO thin film using DFT with LDA+U and a hybrid functional. The phase transition of magnetic order from FM to AFM around a certain range of strain (-1.9% to -2.7%) is found to be a reasonable explanation of the enhancement of the electric polarization in strained BMO thin film. Inversion symmetry, which is incompatible with the ferroelectricity, breaks during the phase transition. The uneven strain model can justify the possibility that the phase transition happens on STO substrate. Our theory also explains the reduction of magnetization of Mn atoms. We suggest that more experiments are needed for further understanding of the structure and magnetic properties in the BMO thin film.

CHAPTER 8

FIRST-PRINCIPLES STUDIES OF Ta_2O_5 POLYMORPHS⁴

Tantalum pentoxide (Ta_2O_5)²⁰⁴ or tantalum, is a potential alternative to SiO_2 because of its high breakdown voltage, high dielectric constant,²⁰⁵ and excellent step coverage characteristics.²⁰⁶ In addition to its applications as dielectric films²⁰⁷ this material also has been used experimentally for optical coatings²⁰⁸ and corrosion coatings.²⁰⁹ The inspiration for the work in this chapter arises from the need for optical coatings in ultra-precision measurements. In ongoing experiments conducted by the laser interferometer gravitational observatory (LIGO), alternating layers of SiO_2 and Ta_2O_5 are used as coatings for the test masses in gravitational wave detectors. It is predicted that the limiting noise in wave detection will be the thermal noise that is closely related to mechanical dissipation and properties of the coating materials.^{210, 211} For the SiO_2/Ta_2O_5 coatings studied, the mechanical dissipation appears to be associated with the Ta_2O_5 component of the coatings.²¹² In addition, the film elastic properties of SiO_2/Ta_2O_5 coatings can significantly influence the expected level of coating thermal noise.²¹⁰ The structural and mechanical properties of Ta_2O_5 films are thus of considerable importance.

Tantala has many crystalline forms, including those which are oxygen-rich and oxygen-deficient. A phase transformation in pure bulk Ta_2O_5 at ~1360 °C was reported²¹³ long ago, but the nature of the structure for each phase continued to stimulate research activity. At low temperature, various polymorphs have been proposed because of the difficulty in growing single crystals of the low-temperature form Ta_2O_5 (L- Ta_2O_5) using conventional high-temperature techniques. A variety of L- Ta_2O_5 structures can be stabilized by adding certain amounts of other oxides.²¹⁴⁻²²⁰ The first

⁴ This work has been published in Physical Review B.²⁰³

one was reported by Stephenson *et al.*²¹⁹ in 1971. The group used the X-ray powder diffraction method and proposed a crystal structure with an orthorhombic unit cell that consists of 22 Ta and 55 O atoms with a large number of oxygen vacancies. Those were then identified as the main cause for a large leakage current.²²¹ In a later study, a vacancy-free L-Ta₂O₅ orthorhombic structure (β -Ta₂O₅) which contains only 4 tantalum and 10 oxygen atoms in the unit cell was observed via x-ray diffraction,²¹⁴ and verified by calculations using DFT with both LDA and GGA²²² functionals. Besides β -Ta₂O₅, experimenters also had reported a hexagonal structure for the low temperature phase of Ta₂O₅ (δ -Ta₂O₅).²²³ Fukumoto *et al.*²²⁴ studied the crystal structure of hexagonal Ta₂O₅, which has the space group of *P*6/*mmm*, using first-principles ultrasoft pseudo-potential calculations. Interestingly, a very recent first-principles study²²⁵ showed that both β -Ta₂O₅ and δ -Ta₂O₅ show some instability with large super cells used to optimize the structure.

For the high-temperature form of Ta₂O₅ (H-Ta₂O₅), orthorhombic, tetragonal and monoclinic models have been proposed.^{220, 226, 227} Similar to L-Ta₂O₅, single crystal H-Ta₂O₅ can be grown with the help of other oxides. Two types of modulation have been proposed for TiO₂-stabilized H-Ta₂O₅. One was determined by Liu *et al.*²²⁸ in 2006 using the conventional solid-state reaction method and advanced laser irradiation technique to hold the pure H-Ta₂O₅ structure at room temperature. They identified the tetragonal structure of pure Ta₂O₅ with the space group *I*4₁/*amd* using transmission electron microscopy (TEM). For the second high temperature tantalum, Makovec *et al.*²²⁹ constructed a complicated structural model from analysis of electron diffraction data and high resolution electron microscopy (HREM) electron images of the solid solutions in the

series $(1-x)\text{Ta}_2\text{O}_5-x\text{TiO}_2$ with $x=0.0-0.1$. The proposed monoclinic crystalline structure is based on edge sharing of an oxygen octahedron-hexagonal bi-pyramid – octahedron molecule building block. This unit block repeats 4 times in a unit cell of high temperature of Ta_2O_5 .

So far, experimental information is mostly limited to structure determination. Crystal-structure-specific mechanical and optical properties are yet to be determined. Compared to the experimental work on Ta_2O_5 mentioned above, theoretical effort, in particular for the high-temperature phases of Ta_2O_5 is even further far behind. We will see later that even the low-temperature phases are not well understood. In this chapter, we present our theoretical results on tantalum starting with the two relatively simple, low temperature Ta_2O_5 polymorphs and followed by a high temperature structure and a complicated low temperature structure. Both have partial oxygen occupation issues that have been studied using the virtual crystal approximation (VCA).²³⁰ In addition, we present our results for a model amorphous structure.

The rest of the chapter is organized as follows: In the second section, we discuss theoretical methods. In the third section, we present our results on structures (8.3.1), cohesive energy and density of states (8.3.2) and elastic moduli (8.3.3) and finally, in the forth section we discuss and conclude our investigations.

8.1 Method and Computational Details

As before, all calculation were done with plane wave PAW^{53, 83} and VASP package.^{83, 84, 229} The exchange and correlation potentials were calculated using the GGA with PW91 parameterization⁴¹. The energy cutoff was 520 eV for wave functions. Gaussian smearing of 0.1 eV was used for Fermi surface broadening. Surface Brillouin-zone integrations were performed on a Monkhorst-Pack¹⁰⁷ k mesh of $8 \times 8 \times 8$ in the

Methfessel-Paxton scheme²³¹ for two low-temperature crystal structures of Ta₂O₅, as well as 8 × 8 × 1 for the high-temperature structure of Ta₂O₅. With these k meshes, the total energies are converged to 0.01 eV. The equilibrium lattice constants for different Ta₂O₅ structures were obtained through total energy minimization. The force tolerance for geometry relaxation was 0.02 eV/Å. For electronic properties, the HSE06 hybrid functional^{232, 233} also was used to calculate the density of states and for comparison with results obtained from PW91.

To simulate systems with partially occupied sites, we constructed pseudo-potentials via the virtual crystal approximation.²³⁰ In VCA, partially occupied sites are assumed to be fully occupied by pseudo-atoms with the pseudo-potential modified by occupancy. Without VCA, many possible configurations can be generated and hence a large supercell is needed to investigate the system.

In the equilibrium state, the cohesive energy is calculated as

$$E_c = (E_{total} - n_{Ta}E_{Ta} - n_OE_O)/(n_{Ta} + n_O), \quad (8-1)$$

where E_{total} is the total energy per cell of a configuration. n_A specifies the number of a particular element (A= Ta, O, Si) in that unit cell, and E_A (A= Ta, O, Si) is the energy of an individual atom calculated with spin-dependent DFT.

Elastic properties can be obtained by calculating the elastic tensor c_{ij} , that relates the stress with the strain for a given system²³⁴, that is,

$$\sigma_i = \sum_{j=1,6} c_{ij} \varepsilon_j, \quad (8-2)$$

where σ_i are stress components, ε_j are small strains. We used the *ab initio* calculation to relate stress response to strains. Elastic constants can be obtained by solving a set

of linear equations of c_{ij} .²³⁵ For all crystalline systems we studied, 1.5% strain is added in six patterns. To obtain sufficiently accurate elastic constants, we adopted stricter convergence and relaxation criteria than the ones used for total energy determination. The force tolerance in relaxation in this study is set to 0.01 eV/Å, and the stress values vary less than 0.02 kBar.

The number of independent elastic constants varies depending on crystalline symmetry. In the case of orthorhombic β -Ta₂O₅, nine independent elastic constants are involved according to Ravindran *et al.*²³⁶ Both the polycrystalline bulk modulus (B) and shear modulus (G) can be determined based on c_{ij} . Two methods, the Voigt approximation²³⁷ (index V) and the Reuss approximation²³⁸ (index R), were proposed. Hill²³⁹ proved that these two methods correspond to upper and lower bounds on the true polycrystalline elastic constants. An approximation can be made by averaging the Voigt and Reuss method results,

$$G = \frac{1}{2}(G_R + G_V) \text{ and } B = \frac{1}{2}(B_R + B_V). \quad (8-3)$$

The average Young's modulus Y and Poisson's ratio ν can be determined by

$$Y = \frac{9BG}{3B+G} \text{ and } \nu = \frac{3B-2G}{2(3B+G)}. \quad (8-4)$$

Reuss moduli (G_R and B_R) and Voigt moduli (G_V and B_V) are written as²³⁶,

$$B_R = \frac{1}{(s_{11} + s_{22} + s_{33}) + 2(s_{12} + s_{13} + s_{23})} \quad (8-5)$$

$$B_V = \frac{1}{9}(c_{11} + c_{22} + c_{33}) + \frac{2}{9}(c_{12} + c_{13} + c_{23}) \quad (8-6)$$

$$G_R = \frac{15}{4(s_{11} + s_{22} + s_{33}) - 4(s_{12} + s_{13} + s_{23}) + 3(s_{44} + s_{55} + s_{66})} \quad (8-7)$$

$$G_V = \frac{1}{15} (c_{11} + c_{22} + c_{33} - c_{12} - c_{13} - c_{23}) + \frac{1}{5} (c_{44} + c_{55} + c_{66}), \quad (8-8)$$

where s_{ij} are the elastic compliance constants, and \mathbf{s} is the inverse of the elastic tensor \mathbf{c} .

The directional dependence of Young's modulus in an orthorhombic crystal can be calculated by²⁴⁰

$$Y = \frac{1}{l_1^4 s_{11} + l_2^4 s_{22} + l_3^4 s_{33} + 2l_1^2 l_2^2 s_{12} + 2l_2^2 l_3^2 s_{23} + 2l_1^2 l_3^2 s_{23} + l_1^2 l_2^2 s_{66} + l_1^2 l_3^2 s_{55} + l_2^2 l_3^2 s_{44}}. \quad (8-9)$$

where l_i are direction cosines to x, y, z, and s_{ij} are the elastic compliance constants.

Young's modulus along axis "i" then becomes

$$Y_i = \frac{1}{s_{ii}} \quad (8-10)$$

where i can be 1,2,3.

For some systems, we also computed directly the bulk modulus according to the second derivative of energy as,

$$B = -V_0 \frac{d^2 E}{dV^2}, \quad (8-11)$$

where V_0 is the volume in the equilibrium state, and d^2E/dV^2 denotes the second derivative of energy with respect to volume. Young's modulus and Poisson's ratio are

$$Y = \left(\frac{L_0}{A_0} \right) \frac{d^2 E}{dL^2}, \quad (8-12)$$

$$\nu = -\frac{1}{2} \frac{L_0}{A_0} \frac{dA}{dL}, \quad (8-13)$$

where L_0 is the original length of the material. A_0 is the original cross-sectional area through which the force is applied. d^2E/dL^2 denotes the second derivative of the energy with respect to length. Comparison of the direct approach and approximated approach are made for some (001) directions to confirm our results.

The primary reason for performing the direct calculations is check the validity of the VCA. The values of modulii and Poisson ratio from Equations 8-11 to 8-13 are different from the ones from Equations 8-2 to 8-10 because of some constraints applied during calculations. For obtaining mechanical properties, one should use Equations 8-2 to 8-10.

8.2 Results and Discussions

8.2.1 Structures

This section presents the four equilibrium structures of low- and high-temperature tantalum. In addition, an amorphous model also is discussed.

8.2.1.1 δ and β L-Ta₂O₅

The two low-temperature structures are δ -Ta₂O₅ and β -Ta₂O₅, which crystallize in a hexagonal structure and an orthorhombic structure respectively (see Figure 8-1 a-b). Both of them contain 4 tantalum and 10 oxygen atoms per cell, thus the Ta:O ratio is 2:5. The experimentally reported space groups are *p6/mmm* for the δ -phase and *pccm* for the β -phase, respectively. However, the optimized structures show large distortions when the symmetry constraint is lifted. This phenomenon was discussed in a recent work²²⁵ where large super-cells were used. Similarly, negative phonon frequencies were obtained if symmetry was kept, indicating an unstable system. After structure optimizations without the symmetry constraints, these two structures distort further and the phonon frequencies at the Gamma point become positive. The optimized lattice

parameters are listed in Table 8-1. In the hexagonal structure (δ -Ta₂O₅), the optimized lattice parameters are slightly larger than the experimental values, leading to a density 4% less than the experimental value. The results with the symmetry constraint (Table 8-1, numbers in parenthesis) are comparable to the values proposed by Sahu *et al*²²² and the density is 2% smaller compared to experiments. Note that the calculated *a* and *c* parameters are larger than those from the experiment, but the *c/a* ratio from both calculations remains the same as the experimental ratio at 0.535. The fully optimized orthorhombic structure (β -Ta₂O₅) has larger lattice parameters *a* and *b* but a smaller *c*, compared to the experiments²²³. Calculations with symmetry constraints show better agreement with experimental data. In particular, the calculated *c/a* ratio agrees well, again, with the experimental value 1.25. Densities from our calculation are 4% lower than the measured values, the same as in δ -Ta₂O₅. Our results do show that δ -Ta₂O₅ has higher density than β -Ta₂O₅, which is in agreement with experiment. Tables 8-1a and 1b provide detailed descriptions of Ta-O bond length and Ta-O-Ta bond angle before and after distortion which are also depicted in Figure 8-2 a-b.

However, one of the four basis oxygen atom sites in the unit cell has a fractional occupancy of 75%, which makes the actual total number of oxygen atoms 30. As a result, The O/Ta ratio is still 2.5. The positions of the two missing oxygen atoms are random. To address the partial occupancy issue, we performed a number of calculations with different approaches including using an oxygen-rich crystal, the virtual crystal approximation (VCA)²³⁰, and various combinations of two selected vacancy sites.

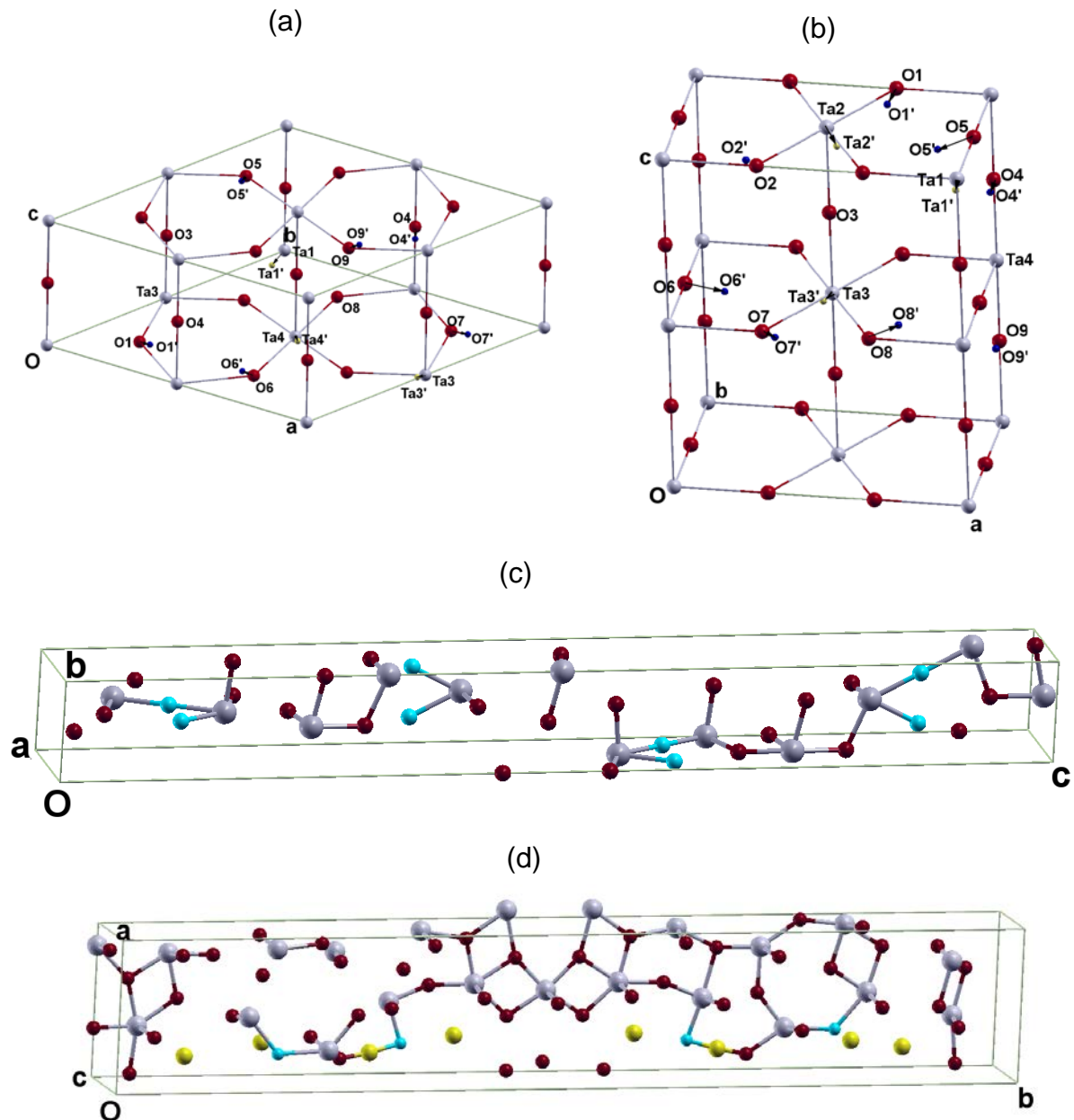


Figure 8-1. Panel (a): Structure of δ -phase Ta_2O_5 . Panel (b): Structure of β -phase Ta_2O_5 . The grey (light) atoms are Ta and red (dark) ones are oxygen. Yellow (light small) atoms are distorted Ta atoms and blue (dark small) ones are distorted oxygen atoms. Distorted atoms are labeled with primes. Panel (c): Structure of tetragonal phase Ta_2O_5 . The blue (grey) atoms are partially occupied oxygen sites. Panel (d): Structure of low temperature phase 77-atom Ta_2O_5 . Blue (grey large) are oxygen atoms with 75% occupancy and yellow (grey small) atoms are oxygen atoms with 25% occupancy.

Table 8-1. The optimized lattice constants, a , b , c . Numbers in parenthesis are calculated with symmetry constraints. All lengths are in unit of Å.

	a (Å)	b (Å)	c (Å)	Density (g/cm ³)
L-Ta₂O₅ δ-phase				
Expt.	7.25		3.88	8.37
Sahu <i>et al.</i>	7.12		3.80	8.86
Ours	7.39 (7.31)		3.90 (3.91)	8.01 (8.17)
L-Ta₂O₅ β-phase				
Expt.	6.22	3.68	7.79	8.29
Sahu <i>et al.</i>	6.19	3.63	7.66	8.59
Ours	6.38 (6.30)	3.82 (3.72)	7.58 (7.89)	7.99 (7.99)
H-Ta₂O₅				
Liu <i>et al.</i>	3.86		36.18	8.23
O-rich	3.91		35.82	8.20
with VCA	3.85		37.45	7.95
Defect_1	3.85	3.96	36.23	8.02
Defect_2	3.85	3.96	36.21	8.02
77-atom L-Ta₂O₅				
Expt.	6.20	40.29	3.89	8.37
Ours	6.74	40.37	3.84	7.79
Amorphous with VCA	11.92	12.88	13.14	8.79
	11.61	11.96	12.29	6.82

Note that we fully expect explicit vacancy models to fail completely for electronic structure characterization. However, for mechanical properties, they can provide a reference point to check the VCA results. In it, a 0.75-factored modification of the oxygen pseudo-potential was made and applied to 8 oxygen sites where vacancy can possibly occur, so that the number of oxygen atoms is effectively 30. In Table 8-1, the crystal without oxygen vacancies is denoted as O-rich, while two with two specific oxygen vacancies are denoted as defect_1 and defect_2, which are typical ones among 28 different combinations of vacant sites. We have fully relaxed the lattice and internal atomic positions for all four tetragonal models. Unlike the L-tantala, this H-tantala crystal does not show visible distortion from the experimentally proposed structure when oxygen sites are either 75% or 100% occupied.

Table 8-2. Comparison of bond lengths and angles of symmetric and optimized δ-phase structure. All lengths are in unit of Å and angles in degree.

		Symmetric	Distorted
Bond Length	Ta1-O2	1.96	1.99
	Ta2-O1	1.99	1.95
	Ta2-O6	1.99	1.94
	Ta2-O4	1.96	1.94
	Ta3-O7	1.99	2.23
	Ta4-O5	1.99	2.10
	Ta4-O9	1.99	1.90
Angle	Ta2-O1-Ta3	132.8	121.4
	Ta2-O6-Ta4	132.8	157.9
	Ta1-O2-Ta1	122.2	145.3
	Ta3-O5-Ta4	180.0	121.9
	Ta3-O9-Ta4	132.8	160.8
	Ta3-O7-Ta2	132.8	157.2
	Ta2-O4-Ta2	180.0	164.9

The optimized geometry parameters are shown in Table 1 and structure in Figure 8-1 c. Both tetragonal structures, one with 32-O and the other with 30-O effectively, maintain the tetragonal unit cell, whereas the two with explicit vacancies do not. For Tetragonal_32O the optimized a and c are 3.91 and 35.82 Å, respectively, which leads to a density of 8.20 g/cm³. The internal atomic coordinates do not show substantial deviation from experimental data. When VCA was used, the optimized lattice parameter a (3.85 Å) is very close to the experiment result (3.86 Å), but c is elongated, which leads to a density 2.9% smaller than the measured one. Systems with two randomly selected vacancies also show lower densities than non-vacancy O-rich model according to our calculation. This trend indicates that VCA is not the reason of the discrepancy between calculations and experiments.

Table 8-3. Comparison of bond lengths and angles of symmetric and optimized β -phase structure. All lengths are in unit of Å and angles in degree.

		Symmetric	Distorted
Bond Length	Ta1-O5	1.84	1.93
	Ta2-O1	2.14	2.19
	Ta2-O2	1.98	2.19
	Ta3-O7	1.94	2.18
	Ta3-O8	1.96	2.19
	Ta4-O6	1.93	1.85
	Ta4-O9	1.93	1.95
Angle	Ta1-O5-Ta1	180.0	138.7
	Ta2-O1-Ta1	122.2	112.7
	Ta2-O2-Ta1	122.2	177.5
	Ta2-O3-Ta3	180.0	159.2
	Ta4-O6-Ta4	180.0	138.7
	Ta3-O7-Ta4	122.5	107.8
	Ta3-O8-Ta4	122.5	180.0
	Ta1-O9-Ta4	180.0	158.7

8.2.1.3 77-atom L-Ta₂O₅

With the capability of VCA and reasonable test results from H-tantala, it is computationally feasible to study the W₂O₅-stabilized low-temperature Ta₂O₅ phase proposed by Stephenson and Roth²¹⁹. In the unit cell, there are 22 Ta sites and 62 O sites. However, due to oxygen vacancies, 4 O sites have 75% occupancy and 8 O sites have 25% occupancy, which effectively makes 55 O atoms in a unit cell and keeps the Ta:O ratio as 2:5. Experimentally, the unit cell is determined to be orthorhombic, with lattice constants a=6.198 Å, b=40.29 Å, and c=3.888 Å. For the two different occupancies of O vacancy sites, we have constructed two types of VCA potentials, 75% and 25% respectively. After full relaxation without symmetry constraint, the orthorhombic unit cell is maintained but the lattice constants change to a=6.74 Å, b=40.37 Å and c=3.84 Å. The optimized unit cell is shown in Figure 8-1 d. (different vacancy sites are in different colors.) The density decreases from 8.37 g/cm³ to 7.79

g/cm^3 after relaxation. Similar to the H- Ta_2O_5 , the symmetry of the structure is lower than for the other two L- Ta_2O_5 . The internal coordinates have also been fully relaxed without imposing any symmetry constraints.

8.2.1.4 Model amorphous Ta_2O_5

The last system we present in this chapter is a model structure for the amorphous phase of Ta_2O_5 . Because there is no published force field, we have not been able to perform a molecular dynamics calculation to obtain amorphous structures. Instead, we used Monte Carlo method to assign positions to Ta and O atoms randomly, with constraints on the range of interatomic distance and coordination numbers. We constructed a cubic unit cell, with 48 Ta and 120 O atoms. Full structure relaxation was performed and an orthorhombic structure with lattice constants $a=11.92 \text{ \AA}$, $b=12.88 \text{ \AA}$ and $c = 13.14 \text{ \AA}$ was obtained; see Figure 8-2 a. To examine this amorphous structure, we calculated the pair correlation, which reflects the radial distribution of Ta-O and Ta-Ta distances for (Figure 8-2 b and 8-c). The pair correlation shows quite good amorphous characteristics, and is in good agreement with experimental data.²⁴¹ However, the calculated density of this model (8.79 g/cm^3) is much higher than for all other models. Therefore, we have to take oxygen vacancies into consideration.

According to Cooks *et al.*²¹¹ and Penn *et al.*,²¹² the density of Ta_2O_5 amorphous thin film ranges from 74% to 93% of bulk density, depending on different experimental conditions. The decrease in density may come from partial oxygen occupancy (or vacancy) in thin films (similar to the situation in the tetragonal H- Ta_2O_5). To include vacancy effects, we followed the same procedure for constructing amorphous structures, but used an 80%-occupied VCA potential for oxygen atoms. In a unit cell of 32 tantalum and 100 oxygen sites, that gives effectively 80 O atoms, were positioned

randomly. After full relaxation, an $11.61 \text{ \AA} \times 11.96 \text{ \AA} \times 12.29 \text{ \AA}$ unit cell was obtained, with density 6.82 g/cm^3 . It is 82.3% of the density of β -phase $\text{L-Ta}_2\text{O}_5$, within the foregoing range of 74%-93%.

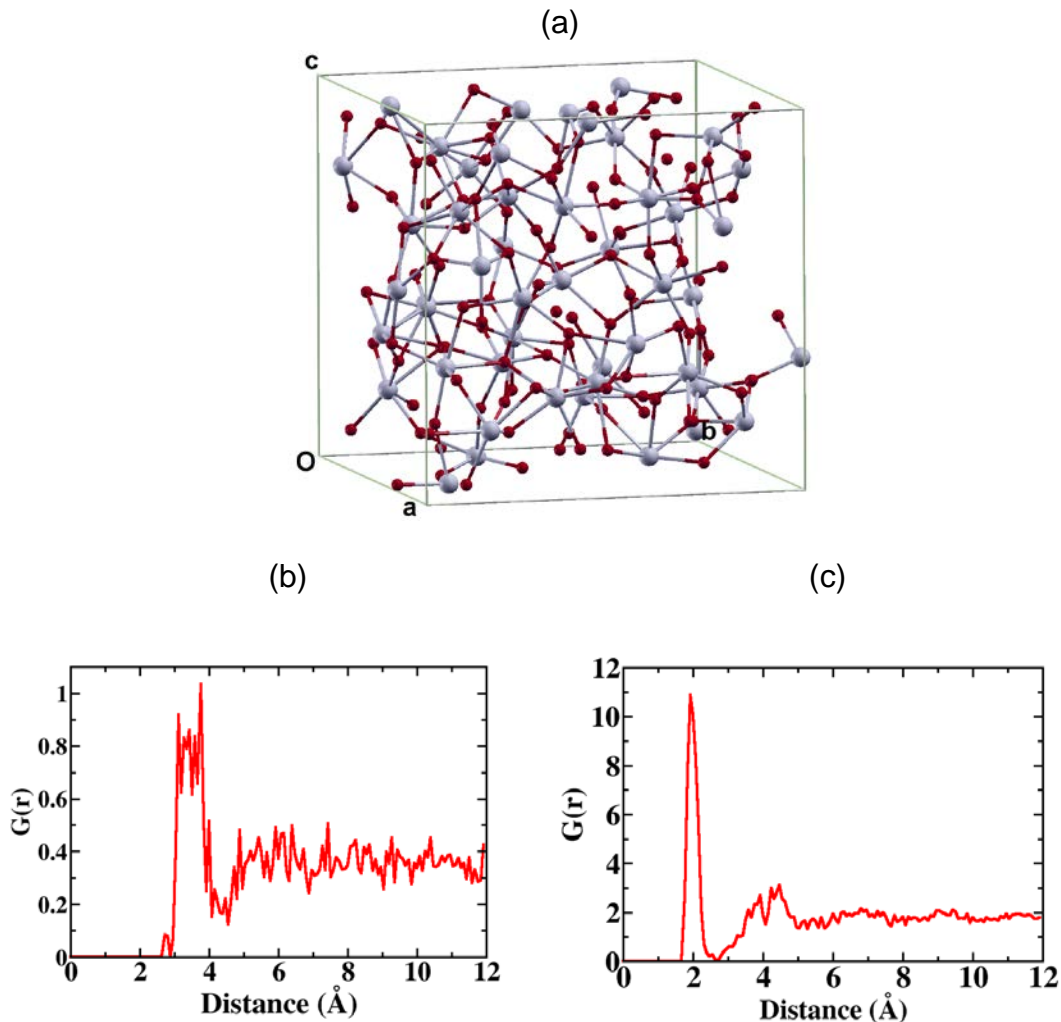


Figure 8-2. Panel (a): Structure of amorphous Ta_2O_5 . Ta atoms are in grey (light) and oxygen atoms are in red (dark). Panel (b): pair correlation function of Ta-Ta in a $2 \times 2 \times 2$ super cell. Panel (c): Pair correlation function of Ta-O in a $2 \times 2 \times 2$ super cell.

8.2.2 Energetics and electronic structure

We calculated the Ta-O cohesive energies for the models mentioned above, relative to the energies of the isolated Ta and O atoms. Results are listed in Table 8-4. Cohesive energies of the hexagonal δ - Ta_2O_5 (7.46 eV) and the orthorhombic β - Ta_2O_5

(7.41 eV) are quite similar with only a 50 meV/atom difference, indicating that the two phases are isomeric. Coincidentally, the difference between the two phases seems to be the same regardless whether or not one imposes symmetry condition on the crystal during calculations. Our results from symmetry-constrained calculations agree with those of Sahu *et al.* For H-Ta₂O₅, tetragonal structure with VCA structure has a cohesive energy 7.21 eV/atom, which is lower than the two L-Ta₂O₅ phases, as expected. Similar to the value within VCA, the two structures each with two O vacancies both have a cohesive energy of 7.26 eV/atom, indicating that VCA is a reasonable approximation. Interestingly, the orthorhombic 77-atom L-Ta₂O₅ calculated using VCA has the second lowest energy, that is, 7.33 eV. Our amorphous model without vacancy shows a 7.23 eV/atom cohesive energy, which is even higher than for the tetragonal VCA model (not a surprise). However, the cohesive energy of the amorphous VCA model is 6.77 eV/atom, which is lower than any other model discussed here. One should not take the exact value of this particular number too seriously, because it merely provides a clue on how the cohesive energy decreases as the systems have partially occupied oxygen sites, or equivalently, the energy decreases when there are vacancies.

Densities of state (DOS) of were calculated, including the δ -phase, β -phase, tetragonal H-Ta₂O₅ and the 77-atom low-T model. To obtain a sensible band gap, which is known to be underestimated by DFT with conventional LDA or GGA, we used the HSE06 hybrid functional to calculate the DOS of the first three systems. Figure 8-3

Table 8-4. Numbers of oxygen and tantalum atoms, and cohesive energy. Values in parentheses are calculated with symmetry constraints. All lengths are in unit of Å.

	n_{Ta}	n_O	O/Ta	E_c (eV/atom)
L-Ta ₂ O ₅ δ-phase	4	10	2.5	7.46 (7.20)
L-Ta ₂ O ₅ β-phase	4	10	2.5	7.41 (7.15)
O-rich H-Ta ₂ O ₅	12	32	2.67	7.18
with VCA	12	30	2.67	7.21
Defect_1	12	30	2.5	7.26
Defect_2	12	30	2.5	7.26
77-atom L-Ta ₂ O ₅	22	55	2.5	7.33
168-atom	48	120	2.5	7.23
Amorphous with VCA	32	80	2.5	6.77

shows the DOS for L- and H-Ta₂O₅ structures. As shown in Figure 8-3 a and b, GGA gives a 1.1 eV gap and 0.1 eV gap for δ-phase and β-phase, respectively, both in a good agreement with Sahu *et al.*²²² However, the HSE06 functional widens the gaps to 2.0 eV and 0.9 eV for the two phases. For tetragonal H-tantala, GGA predicts a metallic system whereas HSE06 opens a gap of 0.9 eV, a substantial improvement over the GGA results (Figure 8-3 c). GGA with VCA shows metallic property for tetragonal H-tantala, which is the same as the O-rich (Figure 8-3 d). Since we currently do not have a VCA potential suitable for use with the HSE06 hybrid functional and construction and test of such potential would constitute a major separate effort, we do not have DOS information on the 77-atom low-T systems (Figure 8-3 e).

8.2.3 Elastic Moduli

In this section, we discuss the mechanical properties of the Ta₂O₅ models. Our focus is on the elastic moduli, including bulk modulus, Young's modulus and Poisson's ratio. All of the calculations started with the equilibrium states for the Ta₂O₅ structures. Table 8-5 presents elastic tensors and derived mechanical functions using Equations 8-3 to 8-13. Because of symmetry, the number of independent elements varies from

system to system. In this case, we remove symmetry constraints and allow all six distortions for every system. Based on the elastic tensors thus obtained, the symmetry is basically maintained in our calculation, though some small deviations exist. For example, c_{11} and c_{22} are different by 5 GPa for O-rich H-Ta₂O₅. All elements of elastic tensor are taken into calculation of elastic constants, which effectively is an average of those elements corresponding to symmetry. Our calculations show that the lower and upper limit of the shear modulus, G_R and G_V from all systems range 49-97 GPa, and those of bulk moduli range 105-221 GPa, Young's moduli 152-233 GPa, and Poisson's ratio 0.25-0.34. We take this as an indication that these crystals have moderately similar mechanical properties when averaged over all directions. It can be seen that the H-Ta₂O₅ (both for the O-rich and VCA model) has higher elastic moduli and Poisson's ratio than the three L-Ta₂O₅ structures, indicating that H-Ta₂O₅ is stiffer. The virtual crystal approximation makes tetragonal H-Ta₂O₅ have a higher shear modulus and Young's modulus than the O-rich model, but lower bulk modulus. Among the three L-Ta₂O₅ crystalline structures, hexagonal δ -Ta₂O₅ shows lower moduli and Possion's ratio than the other two. The last three rows in Table 8-5 are Young's moduli along the x, y, and z directions, respectively. We will compare Y_z with the direct approach below.

8.2.4 Technical remarks: VCA and direct approach

In the direct approach, the conventional way to compute the bulk modulus using first-principles calculations is via Equation 8-11. The volume change for each Ta₂O₅ structure discussed above was achieved by changing the lattice constants. For the two L-Ta₂O₅ systems with small unit cells, all of the atoms were allowed to relax in the cells with the selected volumes, while for all large systems, the internal coordinates were

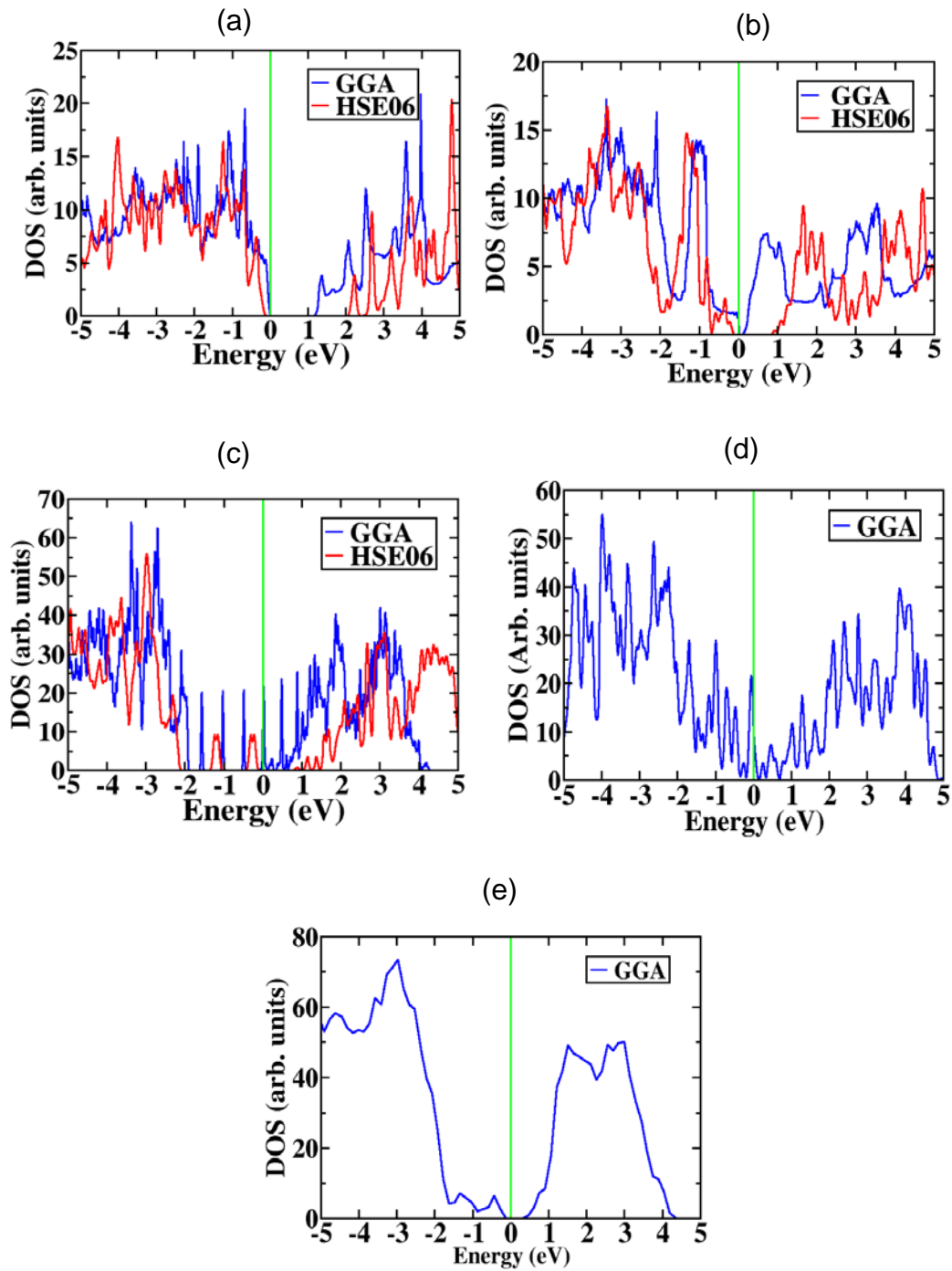


Figure 8-3. Panel (a): DOS of $\delta\text{-Ta}_2\text{O}_5$. Panel (b): DOS of $\beta\text{-Ta}_2\text{O}_5$. Panel (c): DOS of tetragonal $\text{H-Ta}_2\text{O}_5$. Panel (d): DOS of tetragonal $\text{H-Ta}_2\text{O}_5$ with VCA. Panel (e): DOS of low temperature 77 atoms. GGA results are in blue and HSE06 results are in red. Green lines indicate the Fermi level, which is adjusted to be zero.

Table 8-5. Elastic constants, Bulk moduli, Shear moduli, Young's moduli, and Poisson's ratio of different phases of Ta₂O₅. Y_x, Y_y and Y_z are Young's modulus along a, b and c axis.

	Orthorhombic β-Ta ₂ O ₅ (GPa)	Hexagonal δ-Ta ₂ O ₅ (GPa)	Tetragonal O-rich (GPa)	Tetragonal_VCA (GPa)	Orthorhombic 77 atoms L- Ta ₂ O ₅ (GPa)
C ₁₁	290	175	379	445	224
C ₁₂	126	104	173	67	106
C ₁₃	52	169	131	130	44
C ₂₂	263	167	374	443	256
C ₂₃	115	3	130	132	42
C ₃₃	428	403	366	326	430
C ₄₄	78	47	65	64	51
C ₅₅	39	46	65	64	54
C ₆₆	52	57	62	62	36
G _R	64	49	77	81	57
G _V	80	72	84	97	76
B _R	171	105	221	207	140
B _V	174	110	221	208	144
Y	189	152	215	233	172
v	0.32	0.26	0.34	0.34	0.30
Y _x	229	108	283	392	179
Y _y	188	97	280	389	204
Y _z	378	398	304	259	418

scaled proportionally to the changes in lattice constants. The O-rich H-Ta₂O₅ is found to have the largest bulk modulus, 246 GPa (Table 8-6). All other vacancy-doped tetragonal H-Ta₂O₅ models, including defect_1, defect_2 and VCA, are calculated to be 217-227 GPa. The both moduli of two L-Ta₂O₅ structures are nearly the same values (228 GPa and 223 GPa), which are quite close to those reported by Sahu *et al.*²²² However, they are quite different from the values obtained from the elastic tensor, especially in the case of the δ-phase (108 GPa). A possible explanation for the discrepancy is that relaxation of shape could lower the bulk modulus, whereas we do not let the unit cell shape relax in our calculation. The bulk modulus of the amorphous model is 234 GPa and the lowest bulk modulus is 163 GPa for the amorphous VCA model.

Direct calculation of Young's modulus involves much more effort compared to that for the bulk modulus. We focus only on the (001) direction for all systems for comparison with values listed in Table 8-5 (Y_z). To determine the ratio of tensile stress to tensile strain, we elongated and compressed the lattice parameter c . For all systems, Young's moduli were calculated statically. Our calculation shows that high Young's modulus (667 GPa for δ -phase and 606 GPa for β -phase) is a characteristic of the two L-Ta₂O₅ crystals. These values are much higher than the Y_z (398 GPa for δ -phase and 378 GPa for β -phase), which is caused by relaxation of internal coordinates. The high Y values suggest that (001) is a very stiff direction, which is consistent with results in Table 8-5. The H-Ta₂O₅ structures show relatively lower Young's moduli than L-Ta₂O₅ and agree well with Table 8-5. A range of values has been obtained for tetragonal H-Ta₂O₅ models. The O-rich system has a value of 430 GPa, while the two specific vacancy-doped models have 360 GPa and 380 GPa, respectively. Young's modulus H-Ta₂O₅ with VCA is obtained as 345 GPa. The calculated Young's modulus of the amorphous phase is about 320 GPa, which is much higher than the experimentally measured 140 GPa (No amorphous phase was calcuated in Table 8-5). Our results suggest that the amorphous VCA model may be useful for systematically approaching experimental value. Based on our calculation, oxygen vacancies and disorder in crystals cause the materials to soften.

Finally, Poisson's ratios, the ratio of transverse contraction strain to axial extension strain, of these systems, was computed. As seen in Table 8-2, the values of Poisson's

Table 8-6. Bulk moduli, Young's moduli, and Poisson's ratio of different phases of Ta_2O_5 . Y are Young's modulus along c axis, calculated via direct method for validating VCA.

	B (GPa)	Y (GPa)	ν
Exp. (amorphous thin film)		140	0.23
O-rich H- Ta_2O_5	246	430	0.23
with VCA	224	345	0.22
Defect_1	217	360	0.23
Defect_2	227	380	0.23
168-atom Amorphous	234	320	0.27
with VCA	163	263	0.20

ratios in the (001) direction range from 0.09 to 0.23 in the low- and high-temperature crystalline phases, which are lower compared to poly-crystalline averaged values. Poisson's ratio of amorphous system is determined as 0.27. Note that the Possion's ratios calculated directly are in the z direction, so it can be possible that the value is lower than the values in Table 8-5. The amorphous system with oxygen defects described by VCA structure has a Poisson's ration of 0.20. The experimental value of 0.23 lies between 0.20 and 0.27, suggesting that fine tuning the amorphous-VCA model can possibly improve the agreement between theory and experiment.

Since results from VCA and explicit defect models yield similar mechanical properties, as listed in Table 8-6, the VCA seems to be a good approach for modeling vacancies. However, the values from the direct approach are quite different from the ones obtained by using Equation 8-2 to 8-10. The reason is the constraints applied during calculations. For example, uniform lattice scaling in all directions is used for bulk modulus calculations, and fixed angles (among three lattice vectors) are assumed when loading the strain in one direction for calculating Young's modulus. These constraints lead to inaccurate values for systems as sensitive as Ta_2O_5 .

8.3 Summary and Conclusion

In conclusion, the calculated mechanical properties of tantalum peroxide systems show that the Ta_2O_5 crystalline polymorphs and its derivatives have similar mechanical properties but are highly anisotropic. The (001) direction of the high-temperature phase is rather soft compared to all three low-temperature phases, but the (100) and (010) directions are stiffer. All L- Ta_2O_5 phases are energetically more stable than the H- Ta_2O_5 and the amorphous phase. In systems such as H- Ta_2O_5 , 77-atom orthorhombic L- Ta_2O_5 and the amorphous structure, oxygen vacancies (or partial occupancy), soften the materials and lower the cohesive energy. Mass density and Young's modulus also decrease when the systems have oxygen vacancies. By comparison with experimental data, we conclude that the amorphous structure with oxygen vacancy is a good structure model for investigation of a Ta_2O_5 thin film but a thorough investigation is needed in future studies. We also suggest that more experimental measurements should be carried out to understand various crystalline phases.

CHAPTER 9 CONCLUSIONS

We have employed DFT and the PBE and HSE06 functionals to study the adsorption of N₂ and O₂ molecules and Ag_n⁺ cluster cations. The HSE06 hybrid functional is able to predict the right trends of 2D to 3D transition, while PBE fails. For adsorption of nitrogen molecules, polarization dominates the process resulting in exclusively physisorption states. We have found that the physisorption to sites at obtuse corners is stronger than to those at acute ones, which can be explained by the difference of their distance to the charge center. For oxygen molecules, a transition from physisorption to molecular chemisorption occurs with $n > 3$, which is accompanied by charge transfer from cations to the O₂ and O₂ bond elongation. We have also used Ag₄⁺O₂ as an example to understand cooperative nitrogen and oxygen coadsorption. First, the N₂ adsorption energy of some sites far from O₂ increases when there is an O₂ adsorbed on a Ag_n⁺ without inducing extra charge transfer to O₂. Second, when sites near O₂ are also occupied, the charge transfer to O₂ and the O₂ bond length increases but the adsorption energy stay comparable to pure N₂ adsorption. Third, an N₂-induced extra charge transfer results in enhanced binding for the second adsorption shell.

To understand the enhancement of Ag nanofractal fragmentation by chlorine pollution, we have performed a detailed density functional study of (Ag₅₅)₂ dumbbell structures with and without chloridization, as well as surface diffusion of Ag_n and Ag_nCl_m ($n = 1$ to 4) clusters on Ag(111) surfaces. For a single Ag₅₅ cluster, surface adsorption of Cl atoms tends to loosen up the first two layers on the surface. We have shown that the binding energy between two Ag₅₅ icosahedrons in the dumbbell structure is reduced by 17% with surface coverage of chlorine (19 Cl atoms on each Ag₅₅). We also

demonstrated that Ag_nCl_m clusters are generally more mobile than Ag_n clusters on $\text{Ag}(111)$ surfaces for $n=1-4$. The formation energies of Ag_nCl_m imply that Ag_3Cl_3 and Ag_4Cl_4 are good candidates as basic units for Ag surface diffusion in addition to the monomer AgC . The energy barrier calculations indicate that AgCl and Ag_4Cl_4 have barriers substantially lower than their corresponding pure silver clusters, and Ag_3Cl_3 has a barrier slightly lower than Ag_3 . Finally, our investigations have also uncovered diffusion paths of the clusters.

We have demonstrated the concept of molecular magnetocapacitance, in which the quantum part of the capacitance becomes spin-dependent, and is tunable by an external magnetic field. This molecular magnetocapacitance can be realized using single molecule nano-magnets and/or other nano-structures that have antiferromagnetic ground states. As a proof of principle, first-principles calculation of the nano-magnet $[\text{Mn}_3\text{O}(\text{sao})_3(\text{O}_2\text{CMe})(\text{H}_2\text{O})(\text{py})_3]$ shows that the charging energy of the high-spin state is 260 meV lower than that of the low-spin state, yielding a 6% difference in capacitance. A magnetic field of $\sim 40\text{T}$ can switch the spin state, thus changing the molecular capacitance. A smaller switching field may be achieved using nanostructures with a larger moment. Molecular magnetocapacitance could lead to revolutionary device designs, e.g., by exploiting the Coulomb blockade magnetoresistance whereby a small change in capacitance can lead to a huge change in resistance.

We have also investigated the electronic and magnetic properties of the $\text{Fe}_n\text{-C}_{60}$ complexes ($n = 1-4$ and 15). The amount of charge transfer increases monotonically as the number of Fe atoms increases. At low concentration of Fe doping ($n = 1$ or 2), individual Fe atoms diffuse in the interstitial spaces of C_{60} monolayer and bind to C_{60} .

The binding energy is mainly due to the Fe-C bonds. When $n=3$ or more, Fe atoms cluster around the C_{60} molecule as well as bind to C_{60} molecules. Large Fe concentration gives rise to higher binding energy in the Fe_nC_{60} complex. Doping with Fe atoms results in modifications of the C_{60} LUMO-derived bands, which are enhanced by increasing electron occupation. Analysis of PDOS shows that the charge transfer occurs mainly between the Fe- $3d$ orbitals and the t_{1u} orbitals of C_{60} , indicating that the ionic character dominates the Fe- C_{60} bonding. A covalent effect also exists in the Fe- C_{60} bonding. Furthermore, doping with Fe induces a negative magnetic moment in C_{60} , aligning in anti-parallel with Fe. The value of this moment varies roughly within a factor of 2. Heavy Fe-doping does not destroy the structure of C_{60} , but it deforms the electronic structure of C_{60} . Unlike alkali metal doped systems, the Fe-doped systems do not undergo a metal-semiconductor transition.

We have studied the strong bonding of C_{60} molecule on Au(111) surface at room temperature, as well as the weak bonding at low temperature. We calculated the strong bonding configuration at room temperature, i.e., molecules are trapped by a seven-atom pit, with adsorption energy 2.56 eV, which is significantly higher than the energy for a C_{60} sitting on a one-atom pit, or weak bonding on Au(111).

We have also investigated the magnetic and ferroelectric properties of epitaxially strained BMO thin film, using DFT with LDA+U and a hybrid functional. The phase transition of magnetic order from FM to AFM around a certain range of strain (-1.9% to -2.7%) is found to be a reasonable explanation of the enhancement of the electric polarization in strained BMO thin film. Inversion symmetry, which is incompatible with the ferroelectricity, breaks during the phase transition. The uneven strain model can

justify the possibility that the phase transition happens on STO substrate. Our theory also explains the reduction of magnetization of Mn atoms. We suggest that more experiments are needed for further understanding of the structure and magnetic properties in the BMO thin film.

Finally, we have studied the structure, energetics, elastic tensors, and mechanical properties of four crystalline forms of Ta_2O_5 with exact stoichiometry as well as a model amorphous structure. The calculated mechanical properties of tantalum peroxide systems show that the Ta_2O_5 crystalline polymorphs and its derivatives have similar mechanical properties but are highly anisotropic. The (001) direction of the high-temperature phase is rather soft compared to all three low-temperature phases, but the (100) and (010) directions are stiffer. All L- Ta_2O_5 phases are energetically more stable than the H- Ta_2O_5 and the amorphous phase. In systems such as H- Ta_2O_5 , 77-atom orthorhombic L- Ta_2O_5 and the amorphous structure, oxygen vacancies (or partial occupancy), soften the materials and lower the cohesive energy. The mass density and Young's modulus also decrease when the systems have oxygen vacancies. By comparison with experimental data, we conclude that the amorphous structure with oxygen vacancy is a good structural model for investigation of a Ta_2O_5 thin film but a thorough investigation is needed in future studies. We also suggest that more experimental measurements should be carried out to understand various crystalline phases.

LIST OF REFERENCES

- ¹ G. C. Bond and D. T. Thompson, *Catalysis Reviews-Science and Engineering* 41, 319 (1999).
- ² F. Esch, S. Fabris, L. Zhou, T. Montini, C. Africh, P. Fornasiero, G. Comelli, and R. Rosei, *Science* 309, 752 (2005).
- ³ B. Hammer, *Topics in Catalysis* 37, 3 (2006).
- ⁴ P. Li, D. E. Miser, S. Rabiei, R. T. Yadav, and M. R. Hajaligol, *Applied Catalysis B-Environmental* 43, 151 (2003).
- ⁵ P. Lu, T. Teranishi, K. Asakura, M. Miyake, and N. Toshima, *Journal of Physical Chemistry B* 103, 9673 (1999).
- ⁶ M. Mavrikakis, P. Stoltze, and J. K. Norskov, *Catalysis Letters* 64, 101 (2000).
- ⁷ B. Z. Zhan, M. A. White, T. K. Sham, J. A. Pincock, R. J. Doucet, K. V. R. Rao, K. N. Robertson, and T. S. Cameron, *Journal of the American Chemical Society* 125, 2195 (2003).
- ⁸ W. X. Zhang, C. B. Wang, and H. L. Lien, *Catalysis Today* 40, 387 (1998).
- ⁹ X. Zhang and K. Y. Chan, *Chemistry of Materials* 15, 451 (2003).
- ¹⁰ K. S. Novoselov, A. K. Geim, S. V. Morozov, D. Jiang, Y. Zhang, S. V. Dubonos, I. V. Grigorieva, and A. A. Firsov, *Science* 306, 666 (2004).
- ¹¹ K. S. Novoselov, D. Jiang, F. Schedin, T. J. Booth, V. V. Khotkevich, S. V. Morozov, and A. K. Geim, *Proceedings of the National Academy of Sciences of the United States of America* 102, 10451 (2005).
- ¹² K. S. Novoselov, A. K. Geim, S. V. Morozov, D. Jiang, M. I. Katsnelson, I. V. Grigorieva, S. V. Dubonos, and A. A. Firsov, *Nature* 438, 197 (2005).
- ¹³ A. K. Geim and K. S. Novoselov, *Nature Materials* 6, 183 (2007).
- ¹⁴ S. Y. Zhou, G. H. Gweon, J. Graf, A. V. Fedorov, C. D. Spataru, R. D. Diehl, Y. Kopelevich, D. H. Lee, S. G. Louie, and A. Lanzara, *Nature Physics* 2, 595 (2006).
- ¹⁵ R. H. Baughman, A. A. Zakhidov, and W. A. de Heer, *Science* 297, 787 (2002).
- ¹⁶ N. Hamada, S. Sawada, and A. Oshiyama, *Physical Review Letters* 68, 1579 (1992).
- ¹⁷ S. Iijima, *Nature* 354, 56 (1991).

- ¹⁸ S. J. Tans, M. H. Devoret, H. J. Dai, A. Thess, R. E. Smalley, L. J. Geerligs, and C. Dekker, *Nature* 386, 474 (1997).
- ¹⁹ S. J. Tans, A. R. M. Verschueren, and C. Dekker, *Nature* 393, 49 (1998).
- ²⁰ J. Kong, N. R. Franklin, C. W. Zhou, M. G. Chapline, S. Peng, K. J. Cho, and H. J. Dai, *Science* 287, 622 (2000).
- ²¹ M. Y. Han, B. Ozyilmaz, Y. B. Zhang, and P. Kim, *Physical Review Letters* 98 (2007).
- ²² Y. W. Son, M. L. Cohen, and S. G. Louie, *Physical Review Letters* 97 (2006).
- ²³ Y. W. Son, M. L. Cohen, and S. G. Louie, *Nature* 444, 347 (2006).
- ²⁴ X. F. Duan, C. M. Niu, V. Sahi, J. Chen, J. W. Parce, S. Empedocles, and J. L. Goldman, *Nature* 425, 274 (2003).
- ²⁵ L. Y. Jiao, L. Zhang, X. R. Wang, G. Diankov, and H. J. Dai, *Nature* 458, 877 (2009).
- ²⁶ A. Szabo and N. S. Ostlund, *Modern quantum chemistry : introduction to advanced electronic structure theory* (Dover Publications, Mineola, N.Y., 1996).
- ²⁷ P. Hohenberg and W. Kohn, *Physical Review B* 136, B864 (1964).
- ²⁸ W. Kohn and L. J. Sham, *Physical Review* 140, 1133 (1965).
- ²⁹ D. M. Ceperley and B. J. Alder, *Physical Review Letters* 45, 566 (1980).
- ³⁰ J. P. Perdew and A. Zunger, *Physical Review B* 23, 5048 (1981).
- ³¹ J. P. Perdew, K. Burke, and M. Ernzerhof, *Physical Review Letters* 77, 3865 (1996).
- ³² V. I. Anisimov, J. Zaanen, and O. K. Andersen, *Physical Review B* 44, 943 (1991).
- ³³ M. Cococcioni and S. de Gironcoli, *Physical Review B* 71, 035105 (2005).
- ³⁴ A. I. Liechtenstein, V. I. Anisimov, and J. Zaanen, *Physical Review B* 52, R5467 (1995).
- ³⁵ A. D. Becke, *Journal of Chemical Physics* 98, 1372 (1993).
- ³⁶ J. Heyd, G. E. Scuseria, and M. Ernzerhof, *Journal of Chemical Physics* 118, 8207 (2003).
- ³⁷ C. T. Lee, W. T. Yang, and R. G. Parr, *Physical Review B* 37, 785 (1988).

- 38 M. Levy, Physical Review A 26, 1200 (1982).
- 39 L. Tisza, A. Shimony, and H. Feshbach, *Physics as natural philosophy : essays in honor of Laszlo Tisza on his seventy-fifth birthday* (MIT Press, Cambridge, Mass., 1982).
- 40 J. P. Perdew and K. Burke, International Journal of Quantum Chemistry 57, 309 (1996).
- 41 J. P. Perdew and Y. Wang, Physical Review B 45, 13244 (1992).
- 42 A. D. Becke, Physical Review A 38, 3098 (1988).
- 43 J. Jaramillo, G. E. Scuseria, and M. Ernzerhof, Journal of Chemical Physics 118, 1068 (2003).
- 44 J. Paier, M. Marsman, K. Hummer, G. Kresse, I. C. Gerber, and J. G. Angyan, Journal of Chemical Physics 124, 154709 (2006).
- 45 A. D. Becke, Journal of Chemical Physics 96, 2155 (1992).
- 46 K. Kim and K. D. Jordan, Journal of Physical Chemistry 98, 10089 (1994).
- 47 C. Adamo and V. Barone, Journal of Chemical Physics 110, 6158 (1999).
- 48 L. Kleinman and D. M. Bylander, Physical Review Letters 48, 1425 (1982).
- 49 N. Troullier and J. L. Martins, Physical Review B 43, 8861 (1991).
- 50 N. Troullier and J. L. Martins, Physical Review B 43, 1993 (1991).
- 51 A. M. Rappe, K. M. Rabe, E. Kaxiras, and J. D. Joannopoulos, Physical Review B 41, 1227 (1990).
- 52 D. Vanderbilt, Physical Review B 41, 7892 (1990).
- 53 P. E. Blöchl, Physical Review B 50, 17953 (1994).
- 54 R. J. E. Clausius, *Die mechanische Behandlung der Electricität* (F. Vieweg, Braunschweig, 1879).
- 55 R. Resta, Ferroelectrics 136, 51 (1992).
- 56 R. M. Martin, Bulletin of the American Physical Society 17, 102 (1972).
- 57 D. Vanderbilt and R. D. Kingsmith, Physical Review B 48, 4442 (1993).
- 58 R. D. Kingsmith and D. Vanderbilt, Physical Review B 47, 1651 (1993).

- 59 R. Resta, Journal of Physics-Condensed Matter 12, R107 (2000).
- 60 F. Wilczek and A. Shapere, *Geometric phases in physics* (World Scientific, Singapore ; Teaneck , N.J., 1989).
- 61 Y. N. Wu, M. Schmidt, J. Leygnier, H. P. Cheng, A. Masson, and C. Brechignac, Journal of Chemical Physics 136, 024314 (2012).
- 62 P. Jena ed., *Proceedings of the international symposium on the physics and chemistry of small clusters* (Wiley, New York, 1987).
- 63 M. Sundaram, S. A. Chalmers, P. F. Hopkins, and A. C. Gossard, Science 254, 1326 (1991).
- 64 J. I. Brauman, Science 271, 889 (1996).
- 65 M. Mantina, R. Valero, and D. G. Truhlar, Journal of Chemical Physics 131, 064706 (2009).
- 66 L. M. Molina, S. Lee, K. Sell, G. Barcaro, A. Fortunelli, B. Lee, S. Seifert, R. E. Winans, J. W. Elam, M. J. Pellin, I. Barke, V. von Oeynhausen, Y. Lei, R. J. Meyer, J. A. Alonso, A. F. Rodriguez, A. Kleibert, S. Giorgio, C. R. Henry, K. H. Meiwes-Broer, and S. Vajda, Catalysis Today 160, 116 (2011).
- 67 A. Sanchez, S. Abbet, U. Heiz, W. D. Schneider, H. Hakkinen, R. N. Barnett, and U. Landman, Journal of Physical Chemistry A 103, 9573 (1999).
- 68 M. Andersson and A. Rosen, Journal of Physics-Condensed Matter 22, 334223 (2010).
- 69 T. M. Bernhardt, International Journal of Mass Spectrometry 243, 1 (2005).
- 70 G. M. Koretsky and M. B. Knickelbein, Journal of Chemical Physics 107, 10555 (1997).
- 71 S. M. Lang and T. M. Bernhardt, Journal of Chemical Physics 131, 024310 (2009).
- 72 M. Schmidt, P. Cahuzac, C. Brechignac, and H. P. Cheng, Journal of Chemical Physics 118, 10956 (2003).
- 73 M. Schmidt, A. Masson, and C. Brechignac, Physical Review Letters 91, 243401 (2003).
- 74 M. Schmidt, A. Masson, and C. Brechignac, Journal of Chemical Physics 122, 134712 (2005).
- 75 T. Davran-Candan, M. E. Gunay, and R. Yildirim, Journal of Chemical Physics 132, 174113 (2010).

- 76 L. D. Socaciu, J. Hagen, T. M. Bernhardt, L. Woste, U. Heiz, H. Hakkinen, and U. Landman, *Journal of the American Chemical Society* 125, 10437 (2003).
- 77 M. B. Torres, E. M. Fernandez, and L. C. Balbas, *Journal of Physical Chemistry A* 112, 6678 (2008).
- 78 S. A. Varganov, R. M. Olson, M. S. Gordon, and H. Metiu, *Journal of Chemical Physics* 119, 2531 (2003).
- 79 B. Yoon, H. Hakkinen, U. Landman, A. S. Worz, J. M. Antonietti, S. Abbet, K. Judai, and U. Heiz, *Science* 307, 403 (2005).
- 80 H. J. Xiang, S. H. Wei, and X. G. Gong, *Journal of the American Chemical Society* 132, 7355 (2010).
- 81 P. Weis, T. Bierweiler, S. Gilb, and M. M. Kappes, *Chemical Physics Letters* 355, 355 (2002).
- 82 E. M. Fernandez, J. M. Soler, I. L. Garzon, and L. C. Balbas, *Physical Review B* 70, 165403 (2004).
- 83 G. Kresse and D. Joubert, *Physical Review B* 59, 1758 (1999).
- 84 G. Kresse and J. Furthmuller, *Computational Materials Science* 6, 15 (1996).
- 85 G. Kresse and J. Furthmuller, *Physical Review B* 54, 11169 (1996).
- 86 G. Makov, R. Shah, and M. C. Payne, *Physical Review B* 53, 15513 (1996).
- 87 G. Henkelman, A. Arnaldsson, and H. Jonsson, *Computational Materials Science* 36, 354 (2006).
- 88 S. Haupt, J. Kaller, D. Schooss, D. Cameron, and M. M. Kappes, *Zeitschrift Fur Physik D-Atoms Molecules and Clusters* 40, 331 (1997).
- 89 D. Schooss, S. Gilb, J. Kaller, M. M. Kappes, F. Furche, A. Kohn, K. May, and R. Ahlrichs, *Journal of Chemical Physics* 113, 5361 (2000).
- 90 M. M. Biener, J. Biener, and C. M. Friend, *Langmuir* 21, 1668 (2005).
- 91 M. M. Biener, J. Biener, and C. M. Friend, *Surface Science* 601, 1659 (2007).
- 92 A. Bogicevic, S. Ovesson, P. Hyldgaard, B. I. Lundqvist, H. Brune, and D. R. Jennison, *Physical Review Letters* 85, 1910 (2000).
- 93 P. J. Feibelman, *Physical Review Letters* 85, 606 (2000).
- 94 B. K. Min, X. Deng, D. Pinnaduwage, R. Schalek, and C. M. Friend, *Physical Review B* 72, 121410 (2005).

- 95 S. Y. Quek, M. M. Biener, J. Biener, J. Bhattacharjee, C. M. Friend, U. V. Waghmare, and E. Kaxiras, *Journal of Physical Chemistry B* 110, 15663 (2006).
- 96 M. Shen, D.-J. Liu, C. J. Jenks, P. A. Thiel, and J. W. Evans, *Journal of Chemical Physics* 130, 094701 (2009).
- 97 A. Lando, N. Kebaili, P. Cahuzac, C. Colliex, M. Couillard, A. Masson, M. Schmidt, and C. Brechignac, *European Physical Journal D* 43, 151 (2007).
- 98 B. Yoon, V. M. Akulin, P. Cahuzac, F. Carlier, M. de Frutos, A. Masson, C. Mory, C. Colliex, and C. Brechignac, *Surface Science* 443, 76 (1999).
- 99 C. Brechignac, P. Cahuzac, N. Kebaili, A. Lando, A. Masson, and M. Schmidt, *Journal of Chemical Physics* 121, 9617 (2004).
- 100 N. Kebaili, P. Cahuzac, A. Masson, and C. Brechignac, submitted.
- 101 T. Ala-Nissila, R. Ferrando, and S. C. Ying, *Advances in Physics* 51, 949 (2002).
- 102 C. M. Chang, C. M. Wei, and S. P. Chen, *Physical Review Letters* 85, 1044 (2000).
- 103 C. M. Chang, C. M. Wei, and J. Hafner, *Journal of Physics-Condensed Matter* 13, L321 (2001).
- 104 S. S. Hayat, M. A. Ortigoza, M. A. Choudhry, and T. S. Rahman, *Physical Review B* 82, 085405 (2010).
- 105 M. C. Marinica, C. Barreteau, M. C. Desjonquieres, and D. Spanjaard, *Physical Review B* 70, 075415 (2004).
- 106 C. Ratsch and M. Scheffler, *Physical Review B* 58, 13163 (1998).
- 107 H. J. Monkhorst and J. D. Pack, *Physical Review B* 13, 5188 (1976).
- 108 G. Mills and H. Jonsson, *Physical Review Letters* 72, 1124 (1994).
- 109 S. Luryi, *Applied Physics Letters* 52, 501 (1988).
- 110 W. Chen, T. P. Smith, M. Buttiker, and M. Shayegan, *Physical Review Letters* 73, 146 (1994).
- 111 F. Haque, M. Langhirt, E. del Barco, T. Taguchi, and G. Christou, *Journal of Applied Physics* 109, 07B112 (2011).
- 112 H. B. Heersche, Z. de Groot, J. A. Folk, H. S. J. van der Zant, C. Romeike, M. R. Wegewijs, L. Zobbi, D. Barreca, E. Tondello, and A. Cornia, *Physical Review Letters* 96, 206801 (2006).

- ¹¹³ M. H. Jo, J. E. Grose, K. Baheti, M. M. Deshmukh, J. J. Sokol, E. M. Rumberger, D. N. Hendrickson, J. R. Long, H. Park, and D. C. Ralph, *Nano Letters* 6, 2014 (2006).
- ¹¹⁴ T. Komeda, H. Isshiki, J. Liu, Y. F. Zhang, N. Lorente, K. Katoh, B. K. Breedlove, and M. Yamashita, *Nature Communications* 2, 1038 (2011).
- ¹¹⁵ S. Voss, O. Zander, M. Fonin, U. Rudiger, M. Burgert, and U. Groth, *Physical Review B* 78, 155403 (2008).
- ¹¹⁶ L. Michalak, C. M. Canali, M. R. Pederson, M. Paulsson, and V. G. Benza, *Physical Review Letters* 104, 017202 (2010).
- ¹¹⁷ G. J. Iafrate, K. Hess, J. B. Krieger, and M. Macucci, *Physical Review B* 52, 10737 (1995).
- ¹¹⁸ V. V. Shorokhov, E. S. Soldatov, and S. P. Gubin, *Journal of Communications Technology and Electronics* 56, 326 (2011).
- ¹¹⁹ J. Cano, T. Cauchy, E. Ruiz, C. J. Milios, C. C. Stoumpos, T. C. Stamatatos, S. P. Perlepes, G. Christou, and E. K. Brechin, *Dalton Transactions*, 234 (2008).
- ¹²⁰ C. J. Milios, A. G. Whittaker, and E. K. Brechin, *Polyhedron* 26, 1927 (2007).
- ¹²¹ L. A. Ponomarenko, R. Yang, R. V. Gorbachev, P. Blake, A. S. Mayorov, K. S. Novoselov, M. I. Katsnelson, and A. K. Geim, *Physical Review Letters* 105 (2010).
- ¹²² X. G. Zhang, Z. C. Wen, H. X. Wei, and X. F. Han, *Physical Review B* 81, 155122 (2010).
- ¹²³ X. G. Zhang and T. Xiang, *International Journal of Quantum Chemistry* 112, 28 (2012).
- ¹²⁴ L. Li, Y. N. Wu, and H. P. Cheng, *Journal of Chemical Physics* 132, 074702 (2010).
- ¹²⁵ T. R. Ohno, Y. Chen, S. E. Harvey, G. H. Kroll, J. H. Weaver, R. E. Haufler, and R. E. Smalley, *Physical Review B* 44, 13747 (1991).
- ¹²⁶ M. R. C. Hunt, S. Modesti, P. Rudolf, and R. E. Palmer, *Physical Review B* 51, 10039 (1995).
- ¹²⁷ R. Manaila, A. Belu-Marian, D. Macovei, G. Brehm, D. T. Marian, and I. Baltog, *Journal of Raman Spectroscopy* 30, 1019 (1999).
- ¹²⁸ M. R. C. Hunt, P. Rudolf, and S. Modesti, *Physical Review B* 55, 7889 (1997).
- ¹²⁹ A. F. Hebard, R. R. Ruel, and C. B. Eom, *Physical Review B* 54, 14052 (1996).

- ¹³⁰ A. Fartash, Journal of Applied Physics 79, 742 (1996).
- ¹³¹ D. W. Owens, C. M. Aldao, D. M. Poirier, and J. H. Weaver, Physical Review B 51, 17068 (1995).
- ¹³² E. I. Altman and R. J. Colton, Physical Review B 48, 18244 (1993).
- ¹³³ T. R. Ohno, Y. Chen, S. E. Harvey, G. H. Kroll, P. J. Benning, J. H. Weaver, L. P. F. Chibante, and R. E. Smalley, Physical Review B 47, 2389 (1993).
- ¹³⁴ A. F. Hebard, C. B. Eom, Y. Iwasa, K. B. Lyons, G. A. Thomas, D. H. Rapkine, R. M. Fleming, R. C. Haddon, J. M. Phillips, J. H. Marshall, and R. H. Eick, Physical Review B 50, 17740 (1994).
- ¹³⁵ Z. Y. Rong and L. Rokhinson, Physical Review B 49, 7749 (1994).
- ¹³⁶ Y. Y. Wang, R. Yamachika, A. Wachowiak, M. Grobis, and M. F. Crommie, Nature Materials 7, 194 (2008).
- ¹³⁷ C. Papadopoulos, R. S. van den Boogaard, S. Clutterbuck, G. M. Lindsay, and S. R. Winnitoy, Nanotechnology 18, 245306 (2007).
- ¹³⁸ D. Bonifazi, A. Kiebele, M. Stohr, F. Y. Cheng, T. Jung, F. Diederich, and H. Spillmann, Advanced Functional Materials 17, 1051 (2007).
- ¹³⁹ S. S. Jester, P. Weis, M. Hillenkamp, O. T. Ehrler, A. Bottcher, and M. M. Kappes, Journal of Chemical Physics 124, 144704 (2006).
- ¹⁴⁰ L. Chen, W. Chen, H. Huang, H. L. Zhang, J. Yuhara, and A. T. S. Wee, Advanced Materials 20, 484 (2008).
- ¹⁴¹ S. A. Burke, J. M. Mativetsky, S. Fostner, and P. Grutter, Physical Review B 76, 035419 (2007).
- ¹⁴² H. Imahori, Bulletin of the Chemical Society of Japan 80, 621 (2007).
- ¹⁴³ M. Muntwiler, W. Auwarter, A. P. Seitsonen, J. Osterwalder, and T. Greber, Physical Review B 71, 121402 (2005).
- ¹⁴⁴ W. Chen, H. L. Zhang, H. Xu, E. S. Tok, K. P. Loh, and A. T. S. Wee, Journal of Physical Chemistry B 110, 21873 (2006).
- ¹⁴⁵ M. S. Dresselhaus, G. Dresselhaus, and P. C. Eklund, *Science of fullerenes and carbon nanotubes* (Academic Press, San Diego, 1996).
- ¹⁴⁶ A. F. Hebard, M. J. Rosseinsky, R. C. Haddon, D. W. Murphy, S. H. Glarum, T. T. M. Palstra, A. P. Ramirez, and A. R. Kortan, Nature 350, 600 (1991).
- ¹⁴⁷ O. Gunnarsson, Reviews of Modern Physics 69, 575 (1997).

- ¹⁴⁸ P. M. Allemand, K. C. Khemani, A. Koch, F. Wudl, K. Holczer, S. Donovan, G. Gruner, and J. D. Thompson, *Science* 253, 301 (1991).
- ¹⁴⁹ L. L. Wang and H. P. Cheng, *Physical Review B* 69 (2004).
- ¹⁵⁰ L. L. Wang and H. P. Cheng, *Physical Review B* 69, 045404 (2004).
- ¹⁵¹ J. G. Che and H. P. Cheng, *Physical Review B* 72, 115436 (2005).
- ¹⁵² P. Mitra, R. Misra, A. F. Hebard, K. A. Muttalib, and P. Wolfe, *Physical Review Letters* 99, 046804 (2007).
- ¹⁵³ A. Devenyi, R. Manaila, A. Belu-Marian, D. Macovei, M. Manciu, E. M. Popescu, M. Tanase, D. Fratiloiu, N. D. Mihai, P. B. Barna, J. Labar, G. Safran, A. Kovacs, and T. Braun, *Thin Solid Films* 335, 258 (1998).
- ¹⁵⁴ E. Rokuta, Y. Hasegawa, K. Suzuki, Y. Gamou, C. Oshima, and A. Nagashima, *Physical Review Letters* 79, 4609 (1997).
- ¹⁵⁵ C. Oshima and A. Nagashima, *Journal of Physics-Condensed Matter* 9, 1 (1997).
- ¹⁵⁶ A. Nagashima, N. Tejima, Y. Gamou, T. Kawai, and C. Oshima, *Physical Review Letters* 75, 3918 (1995).
- ¹⁵⁷ L. L. Wang and H. P. Cheng, *Physical Review B* 69, 165417 (2004).
- ¹⁵⁸ J. R. Heath, S. C. Obrien, Q. Zhang, Y. Liu, R. F. Curl, H. W. Kroto, F. K. Tittel, and R. E. Smalley, *Journal of the American Chemical Society* 107, 7779 (1985).
- ¹⁵⁹ I. M. L. Billas, C. Massobrio, M. Boero, M. Parrinello, W. Branz, F. Tast, N. Malinowski, M. Heinebrodt, and T. P. Martin, *Computational Materials Science* 17, 191 (2000).
- ¹⁶⁰ W. Branz, I. M. L. Billas, N. Malinowski, F. Tast, M. Heinebrodt, and T. P. Martin, *Journal of Chemical Physics* 109, 3425 (1998).
- ¹⁶¹ S. Fujiki, Y. Kubozono, M. Kobayashi, T. Kambe, Y. Rikiishi, S. Kashino, K. Ishii, H. Suematsu, and A. Fujiwara, *Physical Review B* 65, 235425 (2002).
- ¹⁶² H. N. Li, X. X. Wang, S. L. He, K. Ibrahim, H. J. Qian, R. Su, J. Zhong, M. I. Abbas, and C. H. Hong, *Surface Science* 586, 65 (2005).
- ¹⁶³ C. Cao, P. J. Hirschfeld, and H. P. Cheng, *Physical Review B* 77, 220506 (2008).
- ¹⁶⁴ R. F. Bader, *Atoms in Molecules - A Quantum Theory* (Oxford University Press, Oxford, 1990).
- ¹⁶⁵ C. M. Tang, K. M. Deng, J. L. Yang, and X. Wang, *Chinese Journal of Chemistry* 24, 1133 (2006).

- ¹⁶⁶ P. H. T. Philipsen and E. J. Baerends, *Physical Review B* 54, 5326 (1996).
- ¹⁶⁷ L. Tang, X. Zhang, Q. M. Guo, Y. N. Wu, L. L. Wang, and H. P. Cheng, *Physical Review B* 82, 125414 (2010).
- ¹⁶⁸ J. Biener, E. Farfan-Arribas, M. Biener, C. M. Friend, and R. J. Madix, *Journal of Chemical Physics* 123, 94705 (2005).
- ¹⁶⁹ D. D. Chambliss, R. J. Wilson, and S. Chiang, *Journal of Vacuum Science & Technology B* 9, 933 (1991).
- ¹⁷⁰ K. Morgenstern, J. Kibsgaard, J. V. Lauritsen, E. Laegsgaard, and F. Besenbacher, *Surface Science* 601, 1967 (2007).
- ¹⁷¹ A. W. Stephenson, C. J. Baddeley, M. S. Tikhov, and R. M. Lambert, *Surface Science* 398, 172 (1998).
- ¹⁷² Y. F. Zhang, N. Zhu, and T. Komeda, *Journal of Physical Chemistry C* 111, 16946 (2007).
- ¹⁷³ J. V. Barth, H. Brune, G. Ertl, and R. J. Behm, *Physical Review B* 42, 9307 (1990).
- ¹⁷⁴ C. Woll, S. Chiang, R. J. Wilson, and P. H. Lippel, *Physical Review B* 39, 7988 (1989).
- ¹⁷⁵ M. Bohringer, K. Morgenstern, W. D. Schneider, R. Berndt, F. Mauri, A. De Vita, and R. Car, *Physical Review Letters* 83, 324 (1999).
- ¹⁷⁶ E. I. Altman and R. J. Colton, *Surface Science* 279, 49 (1992).
- ¹⁷⁷ C. Rogero, J. I. Pascual, J. Gomez-Herrero, and A. M. Baro, *Journal of Chemical Physics* 116, 832 (2002).
- ¹⁷⁸ L. Tang, X. Zhang, and Q. M. Guo, *Langmuir* 26, 4860 (2010).
- ¹⁷⁹ X. Zhang, F. Yin, R. E. Palmer, and Q. Guo, *Surface Science* 602, 885 (2008).
- ¹⁸⁰ H. I. Li, K. Pussi, K. J. Hanna, L. L. Wang, D. D. Johnson, H. P. Cheng, H. Shin, S. Curtarolo, W. Moritz, J. A. Smerdon, R. McGrath, and R. D. Diehl, *Physical Review Letters* 103, 056101 (2009).
- ¹⁸¹ W. W. Pai, H. T. Jeng, C. M. Cheng, C. H. Lin, X. D. Xiao, A. D. Zhao, X. Q. Zhang, G. Xu, X. Q. Shi, M. A. Van Hove, C. S. Hsue, and K. D. Tsuei, *Physical Review Letters* 104, 036103 (2010).
- ¹⁸² L. Tang, X. Zhang, and Q. M. Guo, *Surface Science* 604, 1310 (2010).
- ¹⁸³ H. Schmid, *Ferroelectrics* 162, 317 (1994).

- ¹⁸⁴ A. M. dos Santos, S. Parashar, A. R. Raju, Y. S. Zhao, A. K. Cheetham, and C. N. R. Rao, Solid State Communications 122, 49 (2002).
- ¹⁸⁵ N. A. Hill and K. M. Rabe, Physical Review B 59, 8759 (1999).
- ¹⁸⁶ A. A. Belik, S. Iikubo, T. Yokosawa, K. Kodama, N. Igawa, S. Shamoto, M. Azuma, M. Takano, K. Kimoto, Y. Matsui, and E. Takayama-Muromachi, Journal of the American Chemical Society 129, 971 (2007).
- ¹⁸⁷ P. Baettig, R. Seshadri, and N. A. Spaldin, Journal of the American Chemical Society 129, 9854 (2007).
- ¹⁸⁸ W. Eerenstein, F. D. Morrison, J. F. Scott, and N. D. Mathur, Applied Physics Letters 87, 101906 (2005).
- ¹⁸⁹ M. Gajek, M. Bibes, A. Barthelemy, K. Bouzehouane, S. Fusil, M. Varela, J. Fontcuberta, and A. Fert, Physical Review B 72, 020406 (2005).
- ¹⁹⁰ H. Jeen, G. Singh-Bhalla, P. R. Mickel, K. Voigt, C. Morien, S. Tongay, A. F. Hebard, and A. Biswas, Journal of Applied Physics 109, 074104 (2011).
- ¹⁹¹ J. Y. Son and Y. H. Shin, Applied Physics Letters 93, 062902 (2008).
- ¹⁹² A. J. Hatt and N. A. Spaldin, European Physical Journal B 71, 435 (2009).
- ¹⁹³ I. V. Solovyev and Z. V. Pchelkina, New Journal of Physics 10, 073021 (2008).
- ¹⁹⁴ I. V. Solovyev and Z. V. Pchelkina, Physical Review B 82, 094425 (2010).
- ¹⁹⁵ J. B. Goodenough, Physical Review 100, 564 (1955).
- ¹⁹⁶ A. M. dos Santos, A. K. Cheetham, T. Atou, Y. Syono, Y. Yamaguchi, K. Ohoyama, H. Chiba, and C. N. R. Rao, Physical Review B 66, 064425 (2002).
- ¹⁹⁷ C. H. Yang, T. Y. Koo, and Y. H. Jeong, Journal of Magnetism and Magnetic Materials 310, 1168 (2007).
- ¹⁹⁸ H. Yang, Z. H. Chi, J. L. Jiang, W. J. Feng, J. F. Dai, C. Q. Jin, and R. C. Yu, Journal of Materials Science 43, 3604 (2008).
- ¹⁹⁹ D. W. Boukhvalov and I. V. Solovyev, Physical Review B 82, 245101 (2010).
- ²⁰⁰ S. Picozzi, K. Yamauchi, B. Sanyal, I. A. Sergienko, and E. Dagotto, Physical Review Letters 99, 227201 (2007).
- ²⁰¹ I. A. Sergienko, C. Sen, and E. Dagotto, Physical Review Letters 97, 227204 (2006).

- 202 T. Archer, C. D. Pemmaraju, S. Sanvito, C. Franchini, J. He, A. Filippetti, P. Delugas, D. Puggioni, V. Fiorentini, R. Tiwari, and P. Majumdar, *Physical Review B* 84, 115114 (2011).
- 203 Y. N. Wu, L. Li, and H. P. Cheng, *Physical Review B* 83, 144105 (2011).
- 204 C. Chaneliere, J. L. Autran, R. A. B. Devine, and B. Balland, *Materials Science & Engineering R-Reports* 22, 269 (1998).
- 205 S. Zaima, T. Furuta, Y. Koide, Y. Yasuda, and M. Lida, *Journal of the Electrochemical Society* 137, 2876 (1990).
- 206 H. Shinriki and M. Nakata, *IEEE Transactions on Electron Devices* 38, 455 (1991).
- 207 Y. Nishioka, S. Kimura, H. Shinriki, and K. Mukai, *Journal of the Electrochemical Society* 134, 410 (1987).
- 208 Y. Nakagawa and T. Okada, *Journal of Applied Physics* 68, 556 (1990).
- 209 Y. L. Zhou, M. Niinomi, T. Akahori, H. Fukui, and H. Toda, *Materials Science and Engineering a-Structural Materials Properties Microstructure and Processing* 398, 28 (2005).
- 210 D. R. M. Crooks, P. Sneddon, G. Cagnoli, J. Hough, S. Rowan, M. M. Fejer, E. Gustafson, R. Route, N. Nakagawa, D. Coyne, G. M. Harry, and A. M. Gretarsson, *Classical and Quantum Gravity* 19, 883 (2002).
- 211 D. R. M. Crooks, P. Sneddon, G. Cagnoli, J. Hough, S. Rowan, M. M. Fejer, E. Gustafson, R. Route, N. Nakagawa, D. Coyne, G. M. Harry, and A. M. Gretarsson, *Classical and Quantum Gravity* 19, 4229 (2002).
- 212 S. D. Penn, P. H. Sneddon, H. Armandula, J. C. Betzwieser, G. Cagnoli, J. Camp, D. R. M. Crooks, M. M. Fejer, A. M. Gretarsson, G. M. Harry, J. Hough, S. E. Kittelberger, M. J. Mortonson, R. Route, S. Rowan, and C. C. Vassiliou, *Classical and Quantum Gravity* 20, 2917 (2003).
- 213 A. Reisman, F. Holtzberg, M. Berkenblit, and M. Berry, *Journal of the American Chemical Society* 78, 4514 (1956).
- 214 L. A. Aleshina and S. V. Loginova, *Crystallography Reports* 47, 415 (2002).
- 215 C. Askeljung, B. O. Marinder, and M. Sundberg, *Journal of Solid State Chemistry* 176, 250 (2003).
- 216 B. O. Marinder, *Journal of Solid State Chemistry* 160, 62 (2001).

- ²¹⁷ R. S. Roth and J. L. Waring, *Journal of Research of the National Bureau of Standards Section a-Physics and Chemistry A* 74, 485 (1970).
- ²¹⁸ R. S. Roth, J. L. Waring, and W. S. Brower, *Journal of Research of the National Bureau of Standards Section a-Physics and Chemistry A* 74, 477 (1970).
- ²¹⁹ N. C. Stephenson and R. S. Roth, *Acta Crystallographica Section B-Structural Crystallography and Crystal Chemistry B* 27, 1010 (1971).
- ²²⁰ J. L. Waring and R. S. Roth, *Journal of Research of the National Bureau of Standards Section a-Physics and Chemistry A* 72, 175 (1968).
- ²²¹ H. Kimura, J. Mizuki, S. Kamiyama, and H. Suzuki, *Applied Physics Letters* 66, 2209 (1995).
- ²²² B. R. Sahu and L. Kleinman, *Physical Review B* 69, 165202 (2004).
- ²²³ G. S. Oehrlein, F. M. Dheurle, and A. Reisman, *Journal of Applied Physics* 55, 3715 (1984).
- ²²⁴ A. Fukumoto and K. Miwa, *Physical Review B* 55, 11155 (1997).
- ²²⁵ W. Andreoni and C. A. Pignedoli, *Applied Physics Letters* 96, 062901 (2010).
- ²²⁶ S. Lagergren and A. Magneli, *Acta Chemica Scandinavica* 6, 444 (1952).
- ²²⁷ F. Laves and W. Petter, *Helvetica Physica Acta* 37, 617 (1964).
- ²²⁸ X. Q. Liu, X. D. Han, Z. Zhang, L. F. Ji, and Y. J. Jiang, *Acta Materialia* 55, 2385 (2007).
- ²²⁹ D. Makovec, H. M. Zuo, R. Twesten, and D. A. Payne, *Journal of Solid State Chemistry* 179, 1782 (2006).
- ²³⁰ L. Nordheim, *Annalen Der Physik* 9, 607 (1931).
- ²³¹ M. Methfessel and A. T. Paxton, *Physical Review B* 40, 3616 (1989).
- ²³² J. Paier, M. Marsman, K. Hummer, G. Kresse, I. C. Gerber, and J. G. Angyan, *Journal of Chemical Physics* 124, 154709 (2006).
- ²³³ J. Heyd, G. E. Scuseria, and M. Ernzerhof, *Journal of Chemical Physics* 118, 8207 (2006).
- ²³⁴ Y. Le Page and P. Saxe, *Physical Review B* 65, 104104 (2002).
- ²³⁵ H. Z. Yao, L. Z. Ouyang, and W. Y. Ching, *Journal of the American Ceramic Society* 90, 3194 (2007).

- ²³⁶ P. Ravindran, L. Fast, P. A. Korzhavyi, B. Johansson, J. Wills, and O. Eriksson, Journal of Applied Physics 84, 4891 (1998).
- ²³⁷ W. Voigt, *Lehrbuch der kristallphysik* (Teubner, Leipzig, 1928).
- ²³⁸ A. Reuss and Z. Angew, Journal of Applied Mathematics and Mechanics / Zeitschrift für Angewandte Mathematik und Mechanik 9, 49 (1929).
- ²³⁹ R. Hill, Proceedings of the Physical Society of London Section A 65, 349 (1952).
- ²⁴⁰ J. F. Nye, *Physical properties of crystals : their representation by tensors and matrices* (Oxford University Press, Oxford, 1985).
- ²⁴¹ R. Bassiri, K. B. Borisenko, D. J. H. Cockayne, J. Hough, I. MacLaren, and S. Rowan, Applied Physics Letters 98, 031904 (2011).

BIOGRAPHICAL SKETCH

Yuning Wu was born in Yihuang, Province of Jiangxi, P. R. China. He attended University of Science and Technology of China (USTC) in 2002. During his undergraduate student, he started to get interested in condensed matter physics. In 2006, he got his bachelor's degree in physics. In the same year, he became a graduate student in the Department of Physics, University of Florida. In 2007, he joined Prof. Hai-Ping Cheng's group and started to work in computational condensed matter physics. He received his Ph. D. from the University of Florida in the summer of 2012. During his Ph. D., he has been working on structure, energetics, electronic structures of various systems, including nano-clusters, molecular magnets, noble metal surfaces, and crystals.